STUDY OF THE AVERAGE SHEAR VELOCITY OF THE INNER-CORE OF THE EARTH USING ISOLATION FILTERS

by

NICOLAS FISZMAN

Submitted to the Department of
Earth, Atmospheric and Planetary Sciences
in Partial Fulfillment of the Requirements for the Degree of

MASTER OF SCIENCE
in Geophysics

at the

MASSACHUSETTS INSTITUTE OF TECHNOLOGY

September 1994

Signature of the Author_____
Department of Earth, Atmospheric and Planetary Sciences
August 5, 1994

Certified by_____
Professor Thomas H. Jordan
Department of Earth, Atmospheric and Planetary Sciences
Thesis Supervisor

Accepted by_____
Professor Thomas H. Jordan
Department Head

To my brother Jérôme and my sister Anne.

ABSTRACT

In the past, the shear velocity structure of the inner core has been constrained by a combination of low-frequency normal-modes and high-frequency inner-core reflections. Body waves with J legs, like PKJKP, have never been reliably observed as individual phases, so that very little has been learned about the details of inner-core shear velocity structure. There is, however, a significant contribution to the seismogram by intermediate-frequency arrivals that interact as propagating and evanescent shear waves in the inner core. Using the concept of isolation filters, we show how to isolate useful information about the inner core from this energy. We employ normal-mode summation to make synthetic seismograms $\tilde{s}(t)$. Isolation filters $\tilde{f}(t)$ are constructed as a normal-mode sum, where the kth mode is weighted by a coefficient α_k, chosen to enhance inner core modes. $\tilde{f}(t)$ is cross-correlated with the observed seismograms $s(t)$, the cross-correlagrams from different stations are stacked after being normalized and weighted. The time shift between the central peak of the stacked cross-correlation is measured. In this work, we show how the isolation filters can be optimized with respect to the choice of α_k, time-series length, and frequency band. We first apply the method to retrieve the shear velocity of an anelastic, spherically symmetric earth model CORE11. We then apply the method to retrieve the shear velocity for the real Earth. We use Very Long Period data provided by three global digital networks GEOSCOPE, IDA and IRIS/POSEIDON for the March 03, 1994 Fiji event and the June 09, 1994 Bolivia event. Our experiment seems to indicate that the average shear velocity of the Earth is 3.45 km/s. We also show possible evidence of the inner core anisotropy.

ACKNOWLEDGMENTS

I would like to thank here all the people who in one way or another have helped me during my thesis. I want to thank my advisor Tom Jordan for having me here and teaching me the "dark ways of science". He has put up with so much that I won't even attempt to start a list. I also wanted to thank all the friends that I made in this department. The ones who taught me English. The ones who taught me basketball, volleyball, hockey. The ones who spoke French to me (and you will never know how important it was). The ones who taught me how to brew. Nori for putting up with all the numerous phone calls I received over my three years here. The ones who were simply friends and were always there to help me. The Graduate Student Council for providing me with an invaluable opportunity to help graduate students on campus. In short, I would like to thank all of you out there for helping keep some sort of sanity while being here at M.I.T..

I also want to thank my family for being so very supportive over the years.

Merci encore à tous et à toutes,

I would like to finish with a quote from Calvin and Hobbes:

"Given the pace of technology, I propose we leave the math to the machines and go play outside"

And now let's start...

TABLE OF CONTENTS

CHAPTER 1

INTRODUCTION

In this thesis, we study the shear velocity structure of the inner core using the concept of isolation filter and cross-correlation techniques.

The study of the inner core is difficult problem. The signal coming from the core is attenuated, the structure above in the outer core, in the mantle and in the crust is complicated. It is therefore hard to extract the information from the seismogram.

Classically, there have been two ways to treat the problem. One is the isolation of individual modes that have most of their energy in the inner core. This allows us to study seismograms in the frequency band of 0.3 to 5 mHz [*Dziewonski and Gilbert*, 1972; *Masters and Gilbert*, 1981; *Ritzwoller et al.*, 1986;*Widmer et al.*, 1990]. Another possible way to study the inner core structure is to isolate high frequency phases that reflect at the inner core boundary (ICB) [*Shearer and Toy*, 1991] or phases that travel through the inner core such as PKiKP [*Shearer and Masters*, 1990], PKIKP [*Creager*, 1992; *Morelli et al.*, 1986; *Poupinet et al.*, 1983; *Shearer et al.*, 1988], PKJKP [*Julian et al.*, 1972] and all the phases with multiple legs in the inner core. The characteristic frequencies for this study range from 0.7 to 5 Hz.

The isolation and the characterization of a mode is fairly complicated due to effects such as coupling between spheroidal and toroidal modes and anomalous splitting due to heterogeneity [*Dziewonski and Gilbert*, 1971; *Dziewonski and Gilbert*, 1972; *Fukao and Suda*, 1989; *Masters and Gilbert*, 1981]. There are nevertheless about 50 modes that have been positively identified and which have lead to constraints on inner core characteristics such as the mean density of the inner core and the jump of density at the ICB (resp. 1.28 $10^3 \pm 0.15\ 10^3$ kg/m^3 and 500 – 600 kg/m^3 [*Shearer and Masters*, 1990])and the mean

shear velocity of the inner core ($3.45\ 10^3 \pm 0.01\ 10^3$ ms^{-1} [*Dziewonski and Gilbert*, 1972; *Shearer and Masters*, 1990])

On the other hand, observation of seismic phases in the seismogram is also difficult because of the combined low signal and the high noise levels. Positive observations of phases such as PKJKP have not yet been done [*Doornbos*, 1974; *Julian et al.*, 1972]. Other studies using phases such as PKiKP, PKIKP and PKP [*Cummins and Johnson*, 1988b; *Shearer and Masters*, 1990] have managed to constrain the width of the ICB to be less then 5000m and have constrained the jump of shear velocity and of density at the ICB to be respectively larger then 2.500 ms^{-1} and 1.200 kg/m^3. But as Souriau and Souriau [1989] pointed out, the very data selection that is needed in order to be able to make observations for these studies may introduce severe biases in the results.

Because of these observational problems, there remains many unknowns to be determined about the inner core. For example, what is the shear velocity at the ICB? Is it 0 ms^{-1} [*Choy and Cormier*, 1983], $2.5\ 10^3 - 3\ 10^3$ ms^{-1} [*Häge*, 1983] or $3\ 10^3 \pm 1\ 10^3$ ms^{-1} [*Cummins and Johnson*, 1988a]? Furthermore, differential travel time studies have shown major anomalies. But are these due to anisotropy throughout the inner core [*Creager*, 1992; *Shearer et al.*, 1988], anisotropy at the top of the inner core [*Woodhouse et al.*, 1986], heterogeneity in the inner core [*Morelli et al.*, 1986] or heterogeneity in the outer-core [*Ritzwoller et al.*, 1986; *Ritzwoller et al.*, 1988]? If we accept the model of anisotropy in the inner core, then how much anisotropy is there? Some travel time observations required 3% anisotropy [*Creager*, 1992], other travel time data requires 1% anisotropy [*Shearer et al.*, 1988; *Shearer and Toy*, 1991]. Modal data leads to the same type of models [*Li et al.*, 1991; *Widmer et al.*, 1992; *Woodhouse et al.*, 1986] but they tend to over-predict the travel time anomalies that are observed. Recently *Tromp* [1994] produced a model which reconciles the modal and the travel time data. His model based on splitting of normal modes presents a cylindrical anisotropy with the fast axis aligned on the spin axis of the Earth.

We propose a new method to study the shear velocity structure of the inner core. For a given reference model $\tilde{\mathbf{m}}$, we select all the modes that we consider sensitive to the shear velocity structure of the inner core. We sum up these modes to form a synthetic seismogram called isolation filter. We compare our isolation filter to data using cross-correlation techniques. We define two observables, the position of the central peak of the cross-correlation relative to zero time lag, t_c, and the amplitude of the central peak, A. If $\tilde{\mathbf{m}}$ were the real Earth, we would expect the correlation between the synthetic seismogram and the data to be very good in the sense that the cross-correlation function would be peaked at zero time lag and the amplitude of the central peak would be comparable or bigger than the amplitude of the peak of the auto-correlation of the isolation filter. We explore the model space until we find a model which meets these criteria.

In this paper, we first present an experiment using synthetic seismograms only. Synthetic seismograms contain signal generated noise but no ambient noise. We call ambient noise the signal that can be recorded during any quiescent period such as before an earthquake. We call signal generated noise, the signal that is generated by an earthquake but which is not relevant to the shear velocity structure of the inner core. We show how we can decrease the effect of the signal generated noise and therefore increase the resolution of the method by using filtering, time localization and by stacking individual cross-correlations. We show that there is a trade off in the design of the isolation filter between the amplitude and the sensitivity of the isolation filter. The more sensitive a mode is to the shear velocity structure of the inner core, the less amplitude it has at the surface. We will therefore have to choose between increasing the sensitivity of our isolation filter which will decrease the amplitude of our signal, or to increase the amplitude of the signal which will decrease our sensitivity to the shear velocity structure of the inner core. We present a short discussion of the optimal weighting scheme for the stacking of the individual cross-correlations. We use our method to retrieve the average shear velocity of an spherically symmetric, anisotropic, anelastic earth model CORE11.

We then proceed to apply our method to recover the average shear velocity of the real Earth. We study data obtained from 3 global digital networks IDA, GEOSCOPE and IRIS/POSEIDON. We study data from the March 09, 1994 Fiji event which occurred at a depth of 572 km and which had a moment magnitude $M_w = 7.6$, and for the June 09, 1994 Bolivia event which is the second largest event recorded since 1977. It occurred at a depth of 657 km and had a moment magnitude of $M_w = 8.2$. We use a total of 34 stations. For both of these events, we calculate our synthetic seismograms using source time functions provided by a spectral amplitude and phase fitting technique [*Ihmlé*, 1994]. Among all the models which we compare our data to, the one for which we obtain the best cross-correlation is the model with an average shear velocity in the inner core 3% slower than the shear velocity of the inner core of PREM. We also show evidence of difference between weighted stacked cross-correlations for polar and equatorial paths.

CHAPTER 2

EXPERIMENTAL PROCEDURE

Let $\tilde{\mathbf{m}}$ be a reference earth model. For this model, we calculate all the normal spheroidal modes $\tilde{u}_k$. Each mode has an eigenfrequency $\tilde{\omega}_k$, a quality factor $\tilde{Q}_k$, a group velocity $\tilde{g}_k$ and a phase velocity $\tilde{c}_k$.

For each mode, we define a sensitivity ξ_k,

$$\xi_k = \frac{\delta\omega_k}{(\delta\omega_k)_{\max}}, \tag{1}$$

where $\delta\omega_k$ is the frequency perturbation for the mode k due to a perturbation in the inner-core shear velocity $\delta\mathbf{m}$ and $(\delta\omega_k)_{\max}$ is the maximum perturbation for all the modes due to $\delta\mathbf{m}$. We estimate $\delta\omega_k$ using Rayleigh's principle. The first part of Rayleigh's principle states that if $\tilde{u}_k$ is a normal mode then its time averaged kinetic energy is equal to its time averaged potential energy. The second part states that if $\delta\mathbf{m}$ is an admissible variation to the model $\tilde{\mathbf{m}}$, then $\tilde{\omega}_k$ will be a stationary function of $\delta\mathbf{m}$. Applying linear perturbation to Rayleigh's principle, we calculate $\delta\omega_k$,

$$\delta\omega_k = \tilde{\omega}_k \left[\frac{1}{2} \int_0^a \mathbf{G}_k(r)\delta\mathbf{m}(r) r^2 dr \right], \tag{2}$$

where $\mathbf{G}_k(r)$ is the Frechet kernel for the mode $\tilde{u}_k$ relative to a perturbation $\delta\mathbf{m}$ and a is the radius of the Earth [*Backus and Gilbert*, 1967; *Woodhouse and Dahlen*, 1978; *Woodhouse*, 1976]. Since $\delta\omega_k$ and $(\delta\omega_k)_{\max}$ are both calculated using linear perturbation theory, they are both proportional to $\delta\mathbf{m}$. This means that the sensitivity ξ_k is independent from $\delta\mathbf{m}$ and depends only on the model $\tilde{\mathbf{m}}$.

We select modes with a sensitivity bigger then some threshold ε by applying to each mode $\tilde{u}_k$ a weight $\alpha_k = f(\xi_k, \varepsilon)$ between zero and one. We define three seismograms : the full synthetic seismogram $\tilde{s}(t)$,

$$\tilde{s}(t) = \sum \tilde{u}_k , \tag{3}$$

the isolation filter $\tilde{f}(t)$,

$$\tilde{f}(t) = \sum \alpha_k \tilde{u}_k , \tag{4}$$

and the complementary part to the isolation filter also called signal generated noise,

$$\tilde{g}(t) = \tilde{s}(t) - \tilde{f}(t). \tag{5}$$

We show an example of $s(t)$, $\tilde{s}(t)$, $\tilde{f}(t)$ and $\tilde{g}(t)$ on Figure 2.1.

We define $C_{\tilde{f}s}(t)$, the cross correlation between the isolation filter $\tilde{f}(t)$ and some $s(t)$ between two times t_1 and t_2 ,

$$C_{\tilde{f}s}(t) = \int_{t_1}^{t_2} \tilde{f}(t+\tau) s(\tau) d\tau . \tag{6}$$

For each cross-correlation, we measure t_C and A, respectively the time shift between the central peak of the cross-correlation and zero time lag and the amplitude of the central peak.

If the reference model $\tilde{\mathbf{m}}$ described the data, we would have $s(t) = \tilde{s}(t)$. This would lead to

$$C_{\tilde{f}s}(t) \approx C_{\tilde{f}\tilde{s}}(t). \tag{7}$$

Assuming that $\tilde{f}(t)$ and $\tilde{g}(t)$ are not correlated, this brings

$$C_{\tilde{f}s}(t) \approx C_{\tilde{f}\tilde{f}}(t). \tag{8}$$

For $C_{\tilde{f}\tilde{f}}(t)$, t_C is equal to zero and the amplitude A of the central peak is big compared to the amplitude of the nearby peaks. For $C_{\tilde{f}\tilde{s}}(t)$, if the cross-correlation between $\tilde{f}(t)$ and $\tilde{g}(t)$ is small, t_C should be close to zero and the central peak should have a much bigger amplitude than the nearby peaks. In general, since $\tilde{\mathbf{m}}$ will not describe the data exactly, the $C_{\tilde{f}s}(t)$ will not peak at zero time lag but at some time t_C and A will decrease as the difference

between the reference model and the model we are investigating increases. Our experiment then consists of exploring the model space by applying perturbations in the mean shear velocity of the inner core of our reference model to find the model that gives the cross-correlation $C_{\tilde{f}s}(t)$ which is the closest to $C_{\tilde{f}\tilde{s}}(t)$.

Our main concern is to make the resolution of the method as good as possible. Given a small difference between $\tilde{\mathbf{m}}$ and the model we are investigating, we want t_c and A to be as large as possible so that the central peak is well defined and we can make accurate measurements. To improve the resolution of the method, we would like to increase both the sensitivity and the amplitude of $\tilde{f}(t)$. For each mode, the amplitude at the surface of the Earth, a_k is given by

$$a_k(r) = u_k(r)\mathbf{E}_k^*(r_0):\mathbf{M}, \tag{9}$$

where $\mathbf{E}_k$ is the strain tensor for the kth mode, at the location of the source r_0, $\mathbf{M}$ is the moment tensor, * denotes the complex conjugate transpose. We calculate $\langle a_k \rangle$ the geographical average of a_k. $\langle a_k \rangle$ tells us, on average how much a mode contributes to a seismogram. Figure 2.2 shows us that there is a trade-off between the sensitivity of a mode and its amplitude. If we increase the sensitivity of the isolation filter by increasing the threshold ε, we will decrease the amplitude of the signal. On the other hand, if we increase the amplitude of the signal in the isolation filter by lowering ε, we will add more modes with low sensitivity thus decreasing the resolution of the method. Furthermore, there is the problem of the threshold itself. If the threshold is too sharp, this will introduce a sharp discontinuity in frequency in the calculation of the isolation filter. This will cause ringing in the time series and the frequency content of the synthetic seismograms will be dominated by the frequency of the cutoff. In order to avoid this problem, we introduce ε_1 and ε_2 such that

$$\begin{cases} \alpha_k(\xi_k) = 0 & \xi_k < \varepsilon_1 \\ \alpha_k(\xi_k) = \sin^2\left(\dfrac{\pi}{2}\dfrac{\xi_k - \varepsilon_1}{\varepsilon_2 - \varepsilon_1}\right) & \varepsilon_1 \le \xi_k < \varepsilon_2 . \\ \alpha_k(\xi_k) = 1 & \xi_k \ge \varepsilon_2 \end{cases} \tag{10}$$

This makes a smooth weighting functions which allows us to avoid the localization in frequency.

To improve the resolution of the method, we can also improve the data analysis by using filtering and time localization.

Time localization will help us to separate the part of the seismogram with the inner-core signal from the other arrivals. Choosing the time window also involves a trade-off between the amplitude of the signal and the sensitivity to the signal. If we choose t_1 small, we will have a bigger amplitude for both $\tilde{f}(t)$ and $s(t)$ but the cross-correlation will be dominated by the surface waves and so the resolution will be poor. If we choose t_1 large then due to attenuation, the influence of the surface waves will decrease but so will the overall signal from the inner core. We note that the amplitude of the surface waves will decrease faster than the amplitude of waves coming from the inner core because the mantle has an average quality factor of $Q_{mantle} = 156 \pm 13$ [*Jordan and Sipkin*, 1977], whereas the inner core has an average quality factor of $Q_{IC} \in [200 - 600]$ [*Doornbos*, 1983]. Furthermore, constructive interference of multiply reflected waves inside the inner core will contribute to increase the overall signal level coming from the inner core. Figure 2.1 shows us that the ratio of the maximum amplitude of $\tilde{f}(t)$ and the maximum amplitude of $\tilde{s}(t)$ goes from 1/30 after 10 min to 1/5 after 500 min.

We can improve the quality of the cross-correlation by filtering the seismograms between two frequencies ω_1 and ω_2. This will remove some of the arrivals which we are not interested in such as surface and mantle waves which constitute the signal generated noise. The frequency band of that noise is above 20 mHz. It will also remove static noise,

or station noise, which is typically very high below 5 mHz [*Agnew and Berger*, 1964; *Romanowicz and Karczewski*, 1989].

In conclusion, improving the resolution of the method involves finding the set of parameters t_1, t_2, ε_1 , ε_2 , ω_1 and ω_2 that will give the best trade-off between the amplitude and the sensitivity of $\tilde{f}(t)$. We find that the best window in time started 300 min to 500 min after the event time and was between 300 and 400 minutes long. We choose modes with a sensitivity higher than 0.008 and we apply a cosine square weight function with corners at 0.008 and 0.012. We filter our time series before cross correlation using a cosine square band pass filter between 5 mHz and 15 mHz. This frequency band allows us to subtract most of the ambient noise.

Figure Captions

Figure 2.1 : Plot of four seismograms. The top trace is the actual data, *d(t)*, for the station TSK for the June 09, 1994 Bolivia event. The three following traces are respectively the full synthetic seismogram, *s(t)*, the isolation filter, *f(t)*, calculated by summing over all the modes with a relative sensitivity bigger than 0.008 and the signal generated noise seismogram, *g(t)*, obtained by subtracting the isolation filter from the full synthetic seismogram. The last trace is a real ambient noise sample, *n(t)*, collected 1 hour before the event start time. All the traces have been band-pass filtered between 5 and 15 mHz. the synthetic traces have been calculated using the PREM model. The number on the right indicates the maximum amplitude in the seismogram in $m.s^{-2}$. We note that the energy in *s(t)* and in *d(t)* decays faster in time than the energy in *f(t)* . This is why we can use the later parts of the seismograms, still have some signal and not have to much interference because of the surface waves and all the other arrivals we are not interested in. We note however that even after 600 minutes the ratio of the amplitude of *f(t)* to the amplitude of *s(t)* is only about 1/5, which means that in order to apply our method, we need to amplify the signal to noise ratio.

Figure 2.2 : Plot of ξ_k as a function of average amplitude at the surface of the Earth for all the modes for the PREM model. It illustrates the trade-off between sensitivity and signal level that we have to resolve to build the isolation filters.

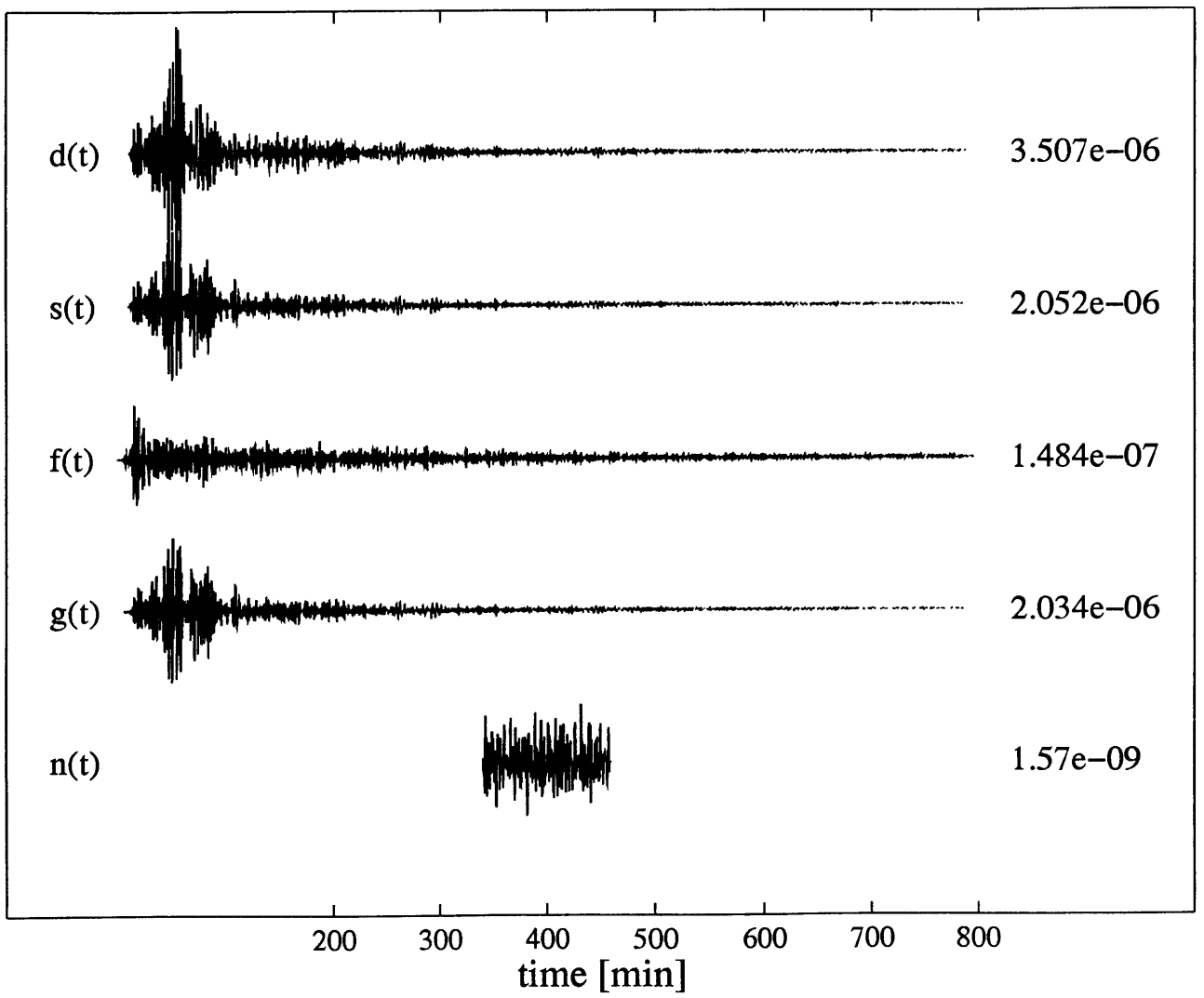
June 09, 1994 Bolivia event station TSK
d(t)
3.507e−06
s(t)
2.052e−06
f(t)
1.484e−07
g(t)
2.034e−06
n(t)
1.57e−09
200
300
400
500
600
700
800
time [min]

Figure 2.1

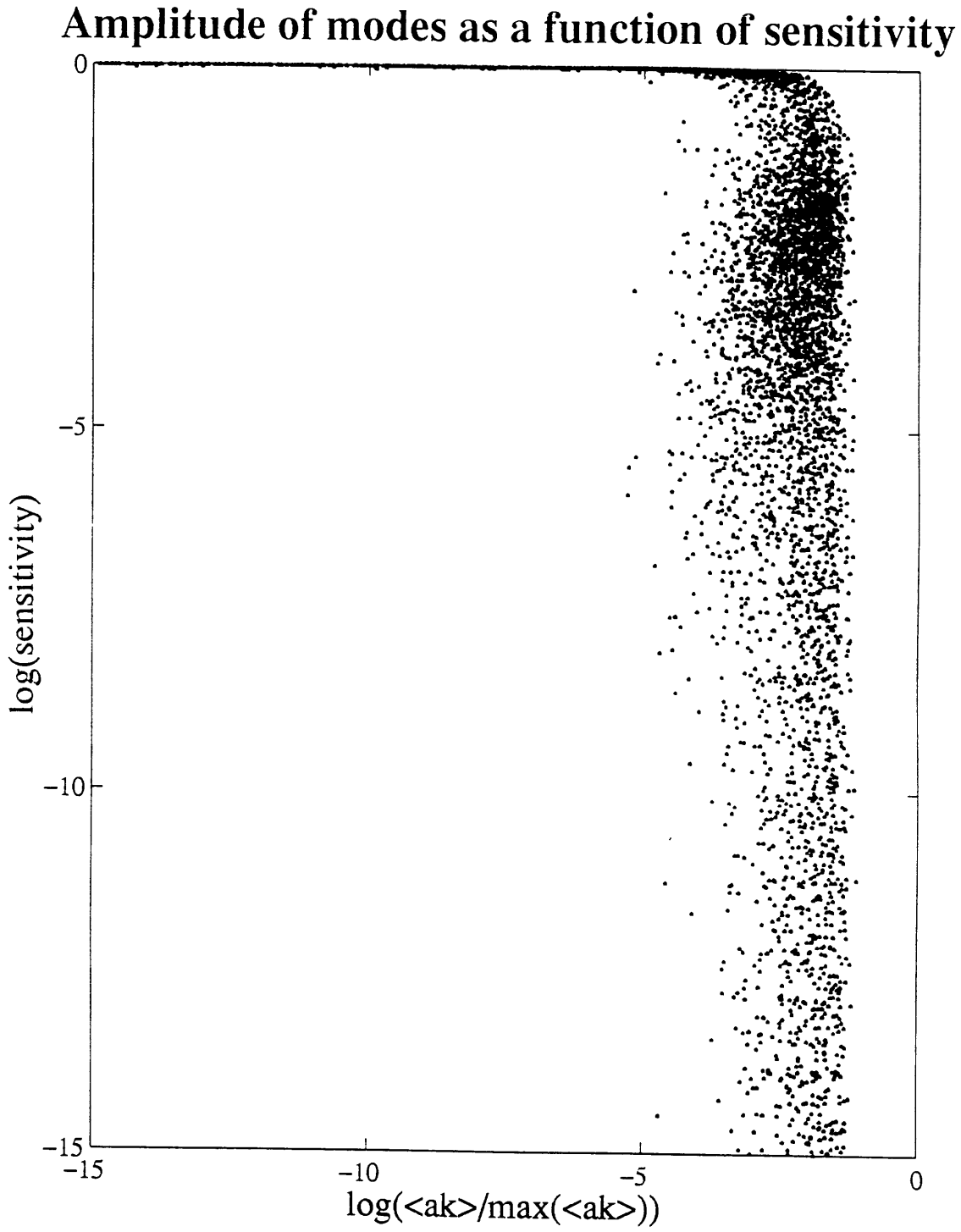
Amplitude of modes as a function of sensitivity
0
−5
−10
−15
log(sensitivity)
−15
−10
−5
0
log(<ak>/max(<ak>))

Figure 2.2

CHAPTER 3

DATA SELECTION AND PROCESSING

3.1 Data selection

For this experiment, we used the data provided by three global digital networks IDA, GEOSCOPE and IRIS/POSEIDON. We used data coming from the March 09, 1994 Fiji event and from the June 09, 1994 Bolivia event.

The Fiji event occurred at a depth of 572 km and had a moment magnitude $M_w = 7.6$. The Bolivia event occurred at a depth of 657 km and had a moment magnitude of $M_w = 8.2$. Both events were deep dip-slip events and had a long source duration. We selected these events on the assumption that because of the depth of their rupture and because of their magnitude they would particularly excite inner core modes.

The data from the IRIS/POSEIDON network is originally sampled at 1s interval. The data from the GEOSCOPE and the IDA networks was sampled at 10 s interval. All the time series were 800 min long. We used a total of 34 seismograms. Figure 3.1 and Figure 3.2 demonstrates we have a good azimuthal coverage. Figure 3.3 and Figure 3.4 shows all the data that we use after filtering between 5 and 15 mHz.

3.2 Processing

We first edited the data to remove all the non linearities. The GEOSCOPE and the IRIS/POSEIDON instruments are broad band Streckeisen instruments. They have a dynamic range greater than 140 dB and did not saturate at the start time of the event. The IDA instruments are LaCoste-Romberg instruments which have a dynamic range below 120 dB. Therefore several stations (KIP, PFO, RAR) saturated at the event start time for

the March 09, 1994 Fiji event and required to have the first 40 minutes of signal after the start of the event time removed.

We remove the tidal component of the seismograms.

Then the seismograms were resampled at 0.5 s and filtered using a band-pass cosine filter between 5 and 15 mHz.

Finally, we remove the instrument response so that all the seismograms are in acceleration units. This effectively also removes the difference of amplification and of gain which exists between different networks

3.3 Synthetic seismogram calculation

We calculate the synthetic seismograms by normal mode summation. We first calculate the Green functions for a point source in time and space. This takes into account the source and the receiver location as well as the propagation effect. We then convolve the synthetic seismograms with the moment tensor for the event. This gives us the information about the source mechanism. Because the two events have such anomalously large ruptures, the point source in time approximation breaks down and we need to convolve the synthetic seismograms with a realistic source time function. These source time functions were obtained by inverting the amplitude and phase spectra of these events in a frequency band between 1 and 250 mHz. The calculation of the seismograms fully accounts for spherical anisotropy. The full synthetic seismograms thus calculated with PREM present a very good fit with the data.

The synthetic seismograms are initially calculated at the same sampling rate as the data They are then resampled at 0.5 s and filtered using the same parameters as for the data.

Figure Captions

Figure 3.1 : Map showing the data coverage for the March 09, 1994 Fiji event in Mercator projection. We plotted the source mechanism at the event location. The station are plotted as triangles. We plotted the great circles between the epicentral location and each station. The azimuthal coverage is broad.

Figure 3.2 : Map showing the data coverage for the June 09, 1994 Bolivia event in Mercator projection. We plotted the source mechanism at the event location. The station are plotted as triangles. We plotted the great circles between the epicentral location and each station. The azimuthal coverage is more restrained to equatorial paths.

Figure 3.3 : Plot of all the data used for the March 09, 1994 Fiji event. Traces 1 to 9 are IDA data, traces 10 to 12 are IRIS/POSEIDON data, traces 13 to 22 are GEOSCOPE data. Note that most of the IDA data has the first 50 minutes edited because the instrument clipped due to a low dynamic range. All the data represented here has been resampled at 0.5 s and band-pass filtered between 5 and 15 mHz.

Figure 3.4 : Plot of all the data used for the June 09, 1994 Bolivia event. Traces 1 to 3 are IRIS/POSEIDON data, traces 4 to 13 are GEOSCOPE data. All the data represented here has been resampled at 0.5 s and band-pass filtered between 5 and 15 mHz.

March 09, 1994 Fiji event

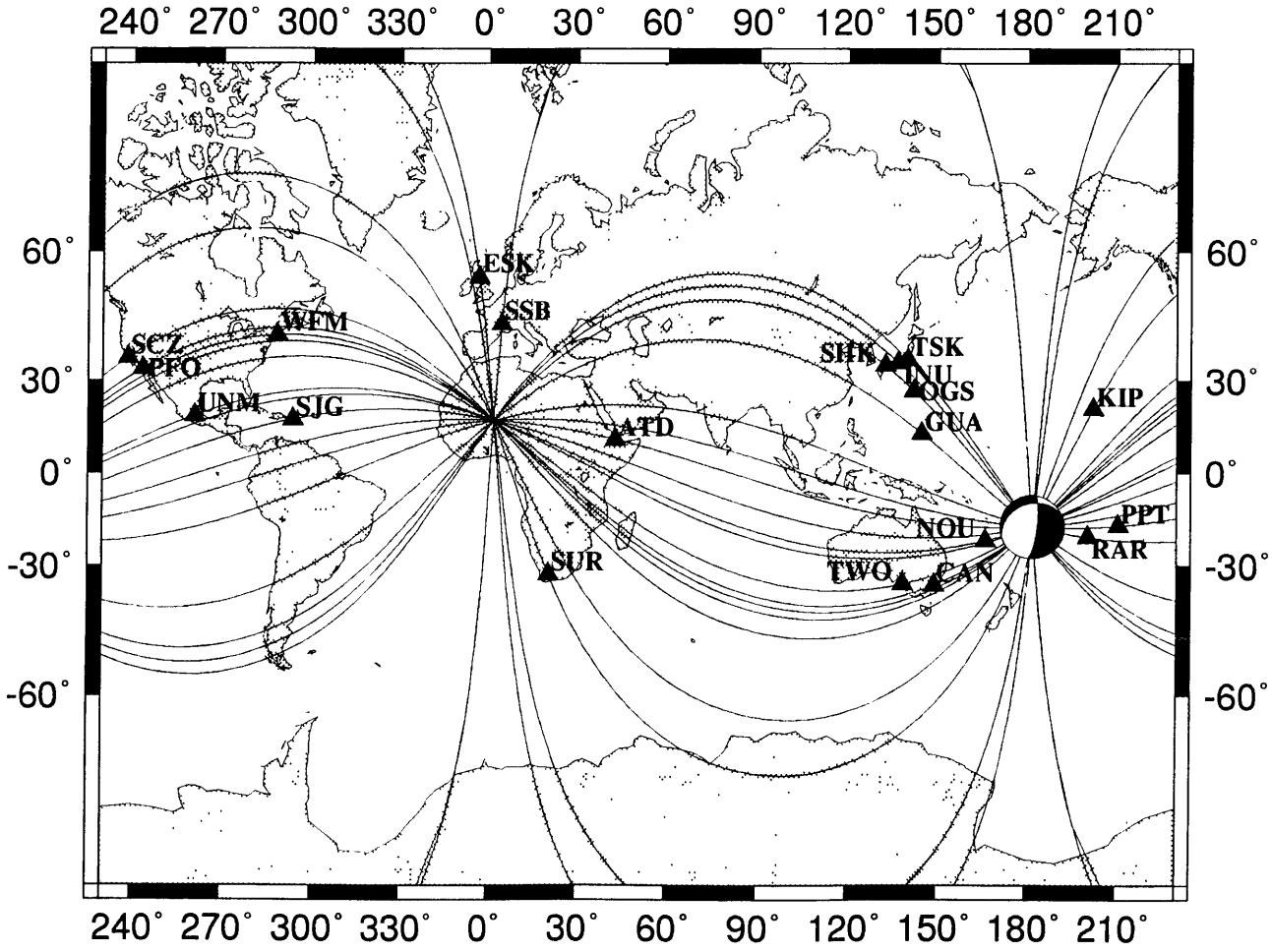

Figure 3.2

June 09, 1994 Bolivia event

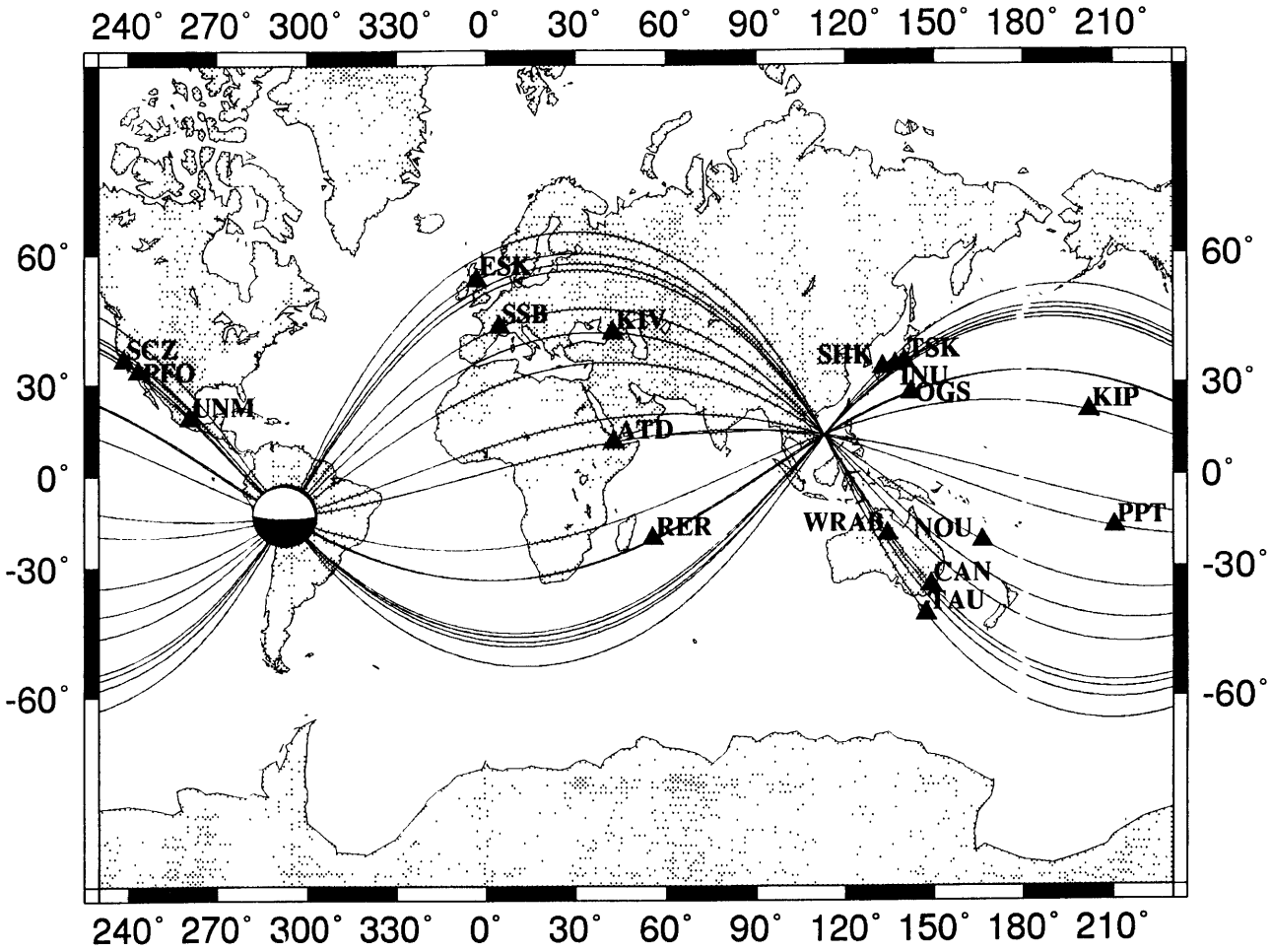

Figure 3.2

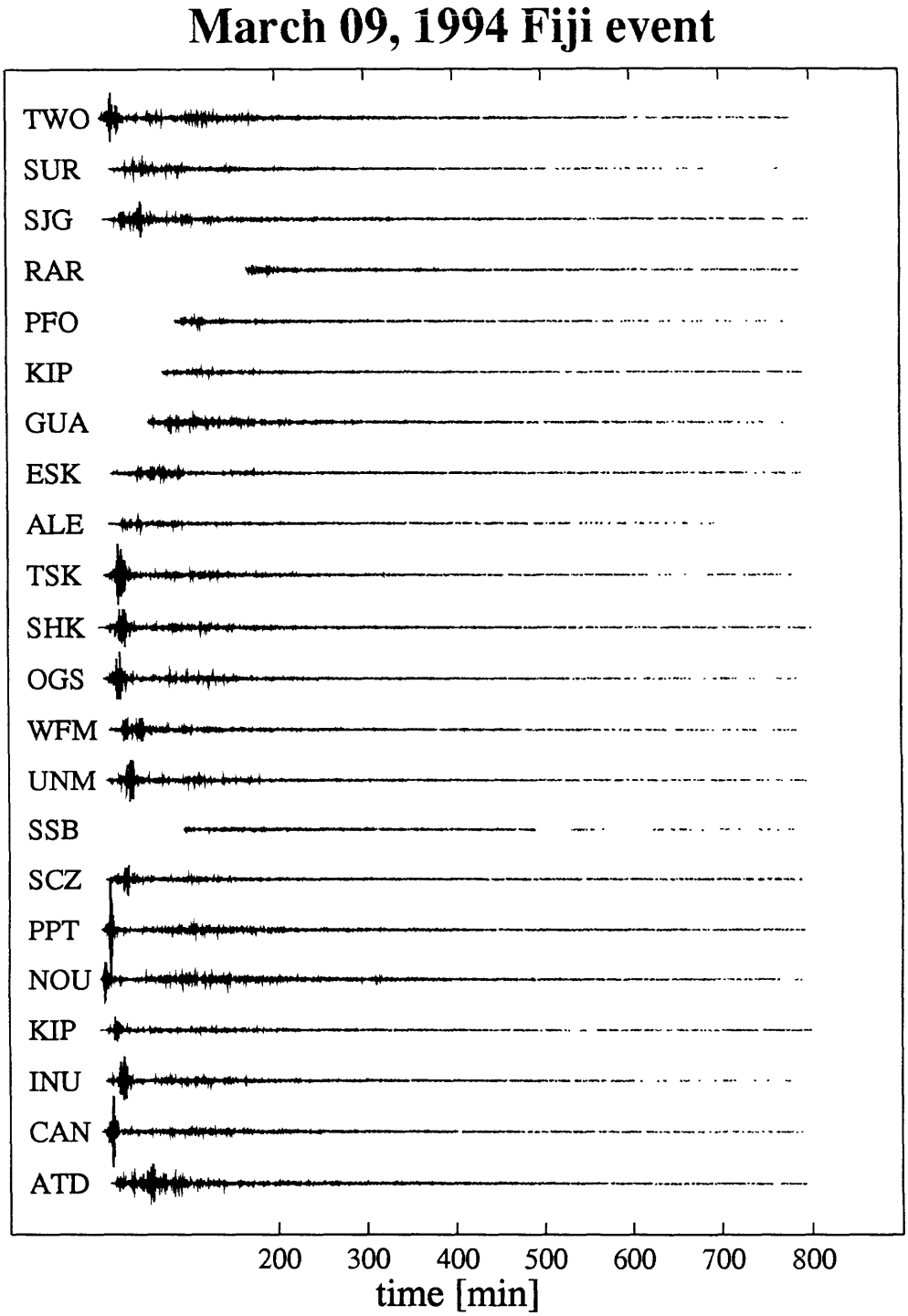
March 09, 1994 Fiji event
TWO
SUR
SJG
RAR
PFO
KIP
GUA
ESK
ALE
TSK
SHK
OGS
WFM
UNM
SSB
SCZ
PPT
NOU
KIP
INU
CAN
ATD
200
300
400
500
600
700
800
time [min]

Figure 3.3

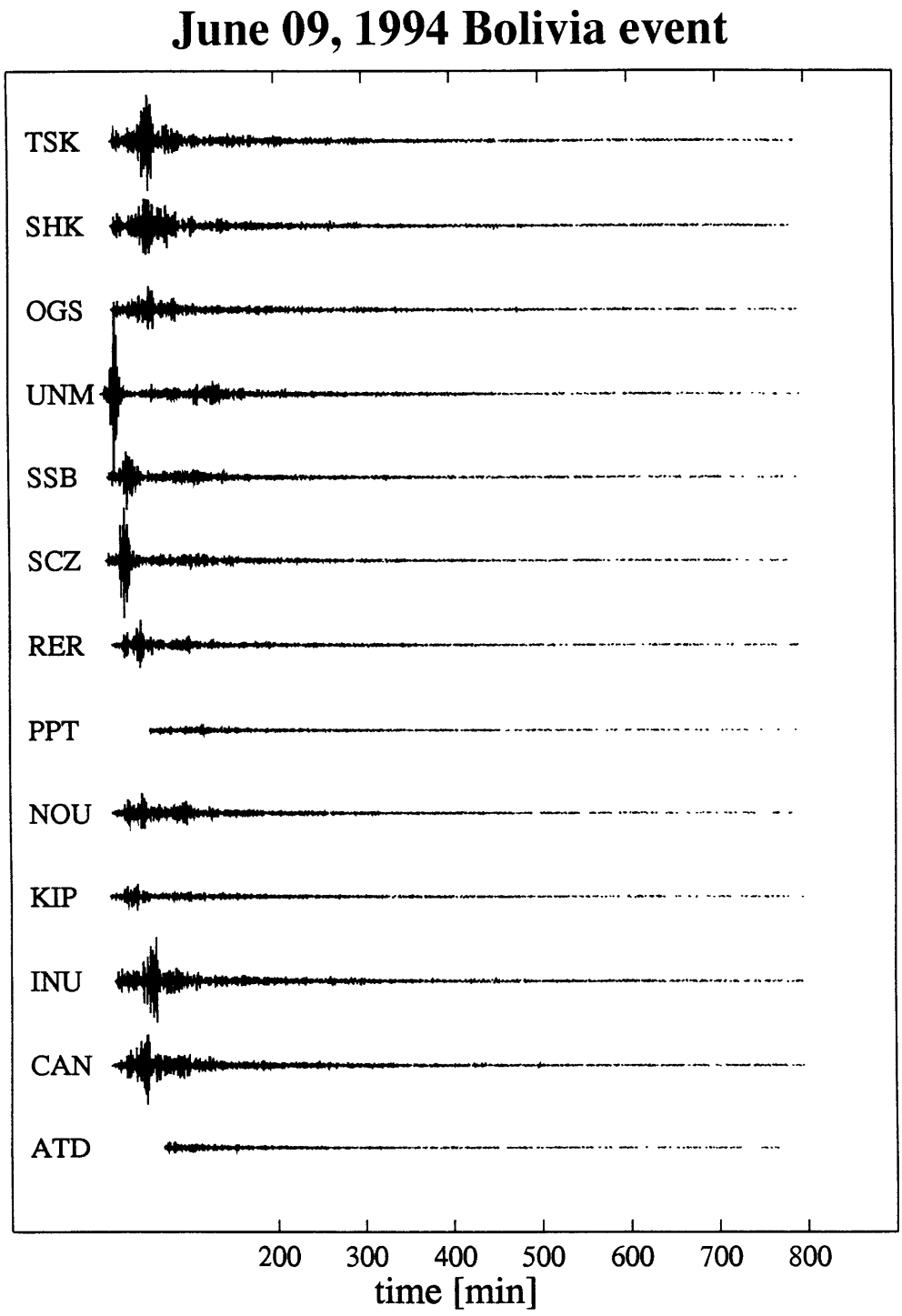
June 09, 1994 Bolivia event
TSK
SHK
OGS
UNM
SSB
SCZ
RER
PPT
NOU
KIP
INU
CAN
ATD
200
300
400
500
600
700
800
time [min]

Figure 3.4

CHAPTER 4

RESULTS

4.1 Synthetic data experiment

To test the our method, we tried to retrieve the shear velocity of the CORE11 model. CORE11 is an unpublished, transversely isotropic, anelastic model that fits the spherically averaged eigenfrequencies compiled by the UCSD group ([*Widmer et al.*, 1988, *G. Masters* personal communication, 1988). We test this model against eleven different models X_i derived from PREM with different average shear velocities in the inner core. PREM is an anelastic, spherically symmetric model [*Dziewonski and Anderson*, 1981]. The average inner-core shear velocities of the X_i models derived from PREM are respectively 10% slower, 4% slower, 3% slower, 2% slower, 0% faster, 1% faster, 1.5% faster, 2% faster, 2.5% faster, 3% faster and 4% faster than PREM.

In the experiment corresponding to the Figure 4.1, we cross correlate $\tilde{f}(t)$ and $\tilde{s}(t)$, both calculated for the PREM model (X_5) for the thirty four station-receiver pairs . We note that although $\tilde{f}(t)$ and $\tilde{s}(t)$ are calculated for the same model, and although $C_{\tilde{f}\tilde{s}}(t)$ should be close to an auto correlation, the $C_{\tilde{f}\tilde{s}}(t)$ are very different from the $C_{\tilde{f}\tilde{f}}(t)$. This is because the inner-core signal is not well localized in time, because there is interference between $\tilde{f}(t)$ and $\tilde{g}(t)$, because of path effects and because the amplitude of $\tilde{f}(t)$ is too small compared to the amplitude of $\tilde{s}(t)$. The central peak is not symmetric with respect to its central location, the amplitude of the central peak is not big with respect to peaks nearby and t_c shows a large scatter around zero time lag. This means that we cannot use the individual cross-correlations because of too much variability between stations.

In order to remedy to this, we stack the cross-correlations. We introduce $S_{\tilde{f}s}(t)$

$$S_{\tilde{f}s}(t) = \sum w_i C^{(i)}_{\tilde{f}s}(t), \tag{11}$$

where the sum extends over all the station-receiver pairs. We weight each $C_{\tilde{f}s}(t)$ with w_i defined as

$$w_i = 1/M_w^{\,2}, \tag{12}$$

where M_w is the moment magnitude for each earthquake. This normalizes the different seismograms and allows us to compare cross-correlations for earthquakes of different sizes.

For one event, equivalent signals come in at different time for different stations because of epicentral distance. Therefore, in stacking seismograms, one needs to shift them in order to make equivalent phases match, so that they stack up well. In our case, we do not have to do this. We cross-correlate seismograms after 300 min. After that length of time, rays have traveled so long in the Earth that the difference in distance between the stations is negligible compared to the total distance traveled. So there should not be any consistent variation of t_c for individual $C_{\tilde{f}s}(t)$ as a function of epicentral distance. Figure 4.1 shows us that this is the case. It also shows that the $S_{\tilde{f}s}(t)$ do stack at zero time lag and that the central peak is symmetrical and well defined. This result also holds for cross-correlations between slightly different models. Figure 4.2 shows thirty four cross-correlations for $\tilde{f}(t)$ calculated for X5 and $s(t)$ calculated for X10. Again, we see that the individual $C_{\tilde{f}s}(t)$ do not present a well defined peak and the t_c show a large scatter, but $S_{\tilde{f}s}(t)$ has a symmetrical well defined central peak. We also note that since the two models do not have the same average shear velocity in the inner core, the central peak of $S_{\tilde{f}s}(t)$ is not at zero time lag. It peaks to the left of the zero time lag which indicates that the model for which we calculate the isolation filters is slow compared to the model we are investigating . In Figure 4.3, we show the stacked cross-correlations for isolation filters calculated for the eleven models and for full synthetic seismograms calculated for X10. We

observe a central peak for each stack. The position of this peak shifts as we change the perturbation in the shear velocity of the inner core. t_C is positive if the model we investigate is slower than the model we use to calculate our isolation filters and negative otherwise. We observe that the peak gets bigger as we get closer 3% perturbation in the shear velocity of the inner core with respect to PREM. The peak stacks is located at zero time lag when we reach the right model. This experiment shows that we can recover the shear velocity of the inner core for synthetic models in the case where we only vary the average of the shear velocity of the inner core.

We shall now show that this remains true if we also change the inner core structure. CORE11 is anisotropic in the inner core whereas PREM is isotropic. CORE11 has an S_V velocity 1.4% faster than the S velocity for PREM and an S_H velocity which is 3.4% faster then the S velocity for PREM. The P velocities in the inner core and the densities are almost identical to PREM (+0.1% for the average P_V, +0.3% for the average P_H velocity and -0.5% for the density ρ). Similarly CORE11 and PREM are not very different in the outer core and in the mantle. In Figure 4.4, we show the $S_{\tilde{f}s}(t)$ for $\tilde{f}(t)$ calculated for the eleven X_i models and $s(t)$ calculated for CORE11. On the right hand side is the value of t_C in seconds. We see that the two models which give the best $S_{\tilde{f}s}(t)$ are the X_9 and X_{10} models. This indicates that the CORE11 model has an average velocity in the inner core which between 2.5% and 3% faster then the shear velocity for PREM. We can even say that it is closer to 3% because the cross-correlation is stronger with model X_{10} than with model X_9. This is also shown on Figure 4.5. There, we plotted the value of t_C and the value of A as a function of the amount of perturbation we apply to PREM. We see that t_C goes to zero between 2.5% and 3%. Figure 4.4 shows that the best model probably is 2.6% faster then PREM in shear velocity in the inner core. This means that the average velocity for a ray traveling in a vertical anisotropic medium is the just the average of the two S_V and S_H velocities. This also shows that we can retrieve the shear velocity in the inner core even if the inner core structure is different.

4.2 Determination of the average shear velocity of the inner core of the Earth

Having ascertained that our method is capable of retrieving the average shear velocity of the inner core of the Earth for a synthetic experiment, we now analyze real seismograms. We test the data against he same eleven models and CORE11.

The experiment is slightly more complicated than for just synthetic seismograms because real data contains both signal generated noise and ambient noise. We model this in the following fashion

$$s_j = f_j + g_j + n_j = f_j + h_j, \tag{13}$$

where s_j stands for the jth data seismogram, f_j is the jth isolation filter, g_j is the jth signal generated noise seismogram, n_j is the jth ambient noise seismogram and the index j runs over all the pair of station-event.

The stack is defined as

$$S_{\tilde{j}s}(t) = \sum w_i C^{(i)}_{\tilde{j}s}(t), \tag{14}$$

where w_j is the weight we apply to the cross-correlation after normalizing for the moment magnitude. The signal from the inner core is small compared to the combined signal from the signal generated noise and the ambient noise. In order to be able to extract the inner-core information, a proper weighting scheme before the stacking is essential. Figure 4.6 shows all the individual cross-correlations without any weighting. The top 20 cross-correlations are for the Fiji event while the bottom 13 are for the Bolivia event. We observe a big discrepancy between individual cross-correlations. Certain stations have a very high amplitude level (i.e. TWO, SJG, NOU, SHK for the June 9, 1994 event). Certain cross-correlations present a well defined central peak (i.e. SHK for the Bolivia event, PPT for

the Bolivia event), whereas other stations do not seem to show any specific peak (i.e. TWO or SJG).

In Figure 4.8 to 4.12, we plot the mean square amplitude levels for the individual $C_{\bar{f}\bar{f}}$, $C_{\tilde{f}s}$, $C_{\tilde{f}\bar{s}}$ and $C_{\tilde{f}\tilde{s}}$ for all the stations and for different time windows. We vary their start time and their length. In each case, we normalize the mean square amplitudes by the maximum value the mean square amplitude of $C_{\tilde{f}s}$. We observe that for a given time window, the ratio between the mean square amplitude level of two stations is the same for $C_{\bar{f}\bar{f}}$, $C_{\tilde{f}s}$, $C_{\tilde{f}\bar{s}}$ or $C_{\tilde{f}\tilde{s}}$. This shows us that the difference in mean square amplitude level between stations is not due to ambient noise since it observed for synthetic and real data. As we start the time window later in the seismograms, we observe that the mean square amplitude level of $C_{\bar{f}\bar{f}}$ increases relatively to that of $C_{\tilde{f}s}$ and $C_{\tilde{f}\bar{s}}$. This, again, illustrates that the energy in the isolation filter decreases slower in time than the energy in the full synthetic seismogram or in the real data. We also observe that the ratio between the mean square amplitude for two different stations stays almost the same as we change the window. This rules out any effect of interference of surface waves since the values should change as we change the window. On Figure 4.13 and Figure 4.14, we plot the mean square amplitude values of $C_{\tilde{f}s}$ at the location of their respective stations. The size of the mean square amplitude is indicated by the size of the symbol at the station. Figure 4.14 shows that for the Bolivia event, all the stations with large mean square amplitude values are located near the antipode of the epicenter. This could suggest that the difference in amplitude may be linked to focusing effects. But this observation does not hold for the Fiji event where the stations with big amplitudes are scattered. Another observation is that most of the stations with a large value of mean square amplitude are on great circles for which the colatitude of the pole of the great circle, l_C, is smaller than 45 degrees (see Figure 4.19). Stations for which l_C is greater than 45 degrees have a smaller mean square amplitude level (see Figure 4.20). Observations have shown that the inner core of the Earth is anisotropic with a fast axis along the pole. One of the best models to date, given

by Tromp [*Tromp*, 1994], uses PREM as an equatorial model and introduces cylindrical anisotropy from there. The difference that we observe between different stations may just reflect the fact that our Earth model (PREM) models the equatorial paths well but fails to account for the inner core structure for polar paths.

We now investigate briefly the importance of ambient noise with respect to the signal generated with the following synthetic experiment. We consider a typical noise power spectrum as given by *Agnew and Berger* [1964] or *Romanowicz and Karczewski* [1989]. The spectrum is displayed Figure 4.15. We calculate noise time series by combining this amplitude information with a random phase. Our noise model is therefore such that

$$\begin{cases} E(n(t)) = 0 \\ Var(n(\omega)) = N^2(\omega) \end{cases} \quad (15)$$

We create a synthetic noise time serie which we filter between 5 and 15 mHz. We then add noise to the full synthetic seismograms. We scale the noise level so that the *rms* of the noise reaches a certain percentage of the *rms* of $C_{\tilde{fs}}$. We show on Figure 4.16 that we can add up noise with an *ms* is 55% the *rms* of the combined signal generated noise and isolation filter, and still observe a clear cross-correlation. Visual inspection of real filtered noise sample (see Figure 2.1), shows that the noise amplitude is about 1/1000 of the amplitude of the real seismogram at the event start time and 1/10 at 700 minutes after the event start time. This shows us that we are in a regime where we can neglect the importance of ambient noise relatively to the signal generated noise.

To remove any possible bias in our stacked cross-correlations by the stations with a big mean square amplitude level, we weight the individual cross-correlations inversely to the root mean square of $C_{\tilde{fs}}$. This sets all the cross-correlations to the same maximum amplitude. Figure 4.7 shows the individual cross-correlations with this weighting. Again, the top 20 cross-correlations are for the Fiji event whereas the bottom 13 are for the Bolivia event. We continue to observe a big difference in character for the different stations. Some

stations such as ESK show a cross-correlation with a very limited frequency band, whereas TSK for both events shows a wider frequency content. In Figure 4.17 and 4.18, we show the weighted stacked cross-correlations obtained for the eleven models and CORE11 and the data with the two types of weighting (resp. $w = 1$ and $w = 1/rms\left(C_{\tilde{fs}}\right)$). We observe that although the values of t_C vary for a same model of isolation filter from Figure 4.17 to Figure 4.18, the stack obtained for the X_i model show very similar characteristics. All the cross-correlations obtained for models X_5 to X_{11} show either no peak or a very badly defined peak. All the cross-correlations for models X_1 to X_4 show a very well defined peak. We observe that for the stacks calculated with CORE11 the characteristic of the stack changes with the weighting. In the case where $w = 1$, the stack for CORE11 is much richer in higher frequencies than the other stacks. In the case of $w = 1/rms\left(C_{\tilde{fs}}\right)$, the stack for CORE11 is very similar to the other stacks obtained with X_i models which have about the same average shear velocity in the inner core (i.e. X_9, X_{10} and X_{11}). Because the shift in t_C between the two types of weighting may reflect a possible bias introduced by the anomalously large individual cross-correlations, from now on, we will adopt the $w = 1/rms\left(C_{\tilde{fs}}\right)$ weighting. We observe the best cross-correlation for the model X_3. Since t_C is positive for all our stacks, our results seem to indicate that all our synthetic models are significantly faster than the real Earth. It is interesting to note that the best cross-correlation which we observe, occurs for a model which has an average shear velocity of 3.45 km/s. This value has been reported by Shearer and Masters in a study using 50 normal modes and PKiKP/PcP amplitude ratio [*Shearer and Masters*, 1990]. We note however that none of the models we tried produces a peak centered at zero time lag. This means that none of the models we have tried is correct in predicting the average shear velocity of the Earth. There are two possible explanations for this. One is that the inner core model we are using is so far removed from the real Earth that we cannot correct the phase delay and produce a peak at zero time lag. Another explanation is that we are not modeling the rest of the Earth correctly and that the 32 seconds shift which we

observe result from that mismatch. The first hypothesis seems unlikely because we do observe a well defined peak. If the model was very different form the real Earth we would not observe such a cross-correlation. To test the second hypothesis, we plot $S_{\tilde{g}s}$ for the different X_i models and for CORE11 for the entire dataset (see Figure 4.23), for the equatorial paths (see Figure 4.24) and for the polar paths (see Figure 4.25). If the complementary part of our models was similar to the real Earth, we would observe stacks peaking at zero time lag. Furthermore the stacks for the equatorial paths, the polar paths and for the entire dataset would be identical. We observe that all the stacked cross-correlations have nearly identical characteristics We also observe t_C values of 19 seconds for the entire dataset, 5 seconds for the polar paths and 38 seconds for the equatorial paths. The fact that the $S_{\tilde{g}s}$ all have the same characteristic tells us that, as expected, the signature from the crust, the mantle and the outer core is similar for all our models. The t_C value for the stacks for the entire dataset are the average of the t_C values obtained for the equatorial and the polar paths. This shows us that the time shift which we observe is probably due to ellipticity. The real Earth is 0.11% wider at the equator than PREM. A PKIKP crossing the Earth diagonally would travel 1.36 seconds faster in our model than it would in the real Earth just due to the difference in radius. For a time window between 400 minutes and 700 minutes, this wave would have accumulated an advance ranging from 26.9 seconds to 47.0 seconds relatively to the Earth. We are dealing with a complex superposition of different waves. This means that the average phase delay observed will probably lie within the bounds that we have calculated and that this may help us to explain this 32 seconds phase delay that we observe for $C_{\tilde{f}s}$. To completely prove our point, we would need to calculate synthetic seismograms which correct for ellipticity. We can nevertheless conclude that our method allowed us to retrieve the average shear velocity of the inner-core of the Earth and that the reason why the stacked cross-correlations do not peak at zero time lag is probably an effect of the Earth ellipticity. According to our experiments the value of the average shear velocity in the inner core is about 3.45 km/s.

4.3 Evidence of azimuthal variations in the shear velocity structure of the inner core of the Earth

Evidence for anisotropy was first reported by *Poupinet et al.* [1983] in a study of P residuals in PKIKP travel times. They proposed a model based on anisotropy in the inner core with a fast axis along the spin axis of the Earth or alternatively a model in which the ICB would elongated of 200 km at the poles. An evidence for anomalous splitting was then observed by *Masters and Gilbert* [1981] for modes ${}_{10}S_2$ and ${}_{6}S_2$. It was only explained as anisotropy by *Dziewonski and Gilbert* [1972]. Since then, normal spheroidal mode observations have shown that other modes, also believed to be core modes, present an anomalously large splitting. Differential travel times studies using PKIKP, PKP-BC, PKP-DF and PKP-Cdiff have confirmed that there is a travel time difference between rays traveling along the spin axis of the Earth and rays presenting a bigger angle to the spin axis of the Earth. Several models have been presented to explain these anomalies. They either involve anisotropy at the top of the inner core ([*Morelli et al.*, 1986;*Woodhouse et al.*, 1986]), or anisotropy throughout the inner core [*Creager*, 1992; *Shearer et al.*, 1988] or heterogeneity in the outer core ([*Ritzwoller et al.*, 1986; *Ritzwoller et al.*, 1988]). *Masters et al.* [1992] suggested that most of the anomalously split modes sample the outer core but not the inner core, thus suggesting that the anisotropy be located in the outer core and not in the inner core. None of these models agree one with another. *Shearer* [1988; 1991] proposes a uniform anisotropy of 1% throughout the inner core, while *Creager* [1992] requires 3.5% anisotropy near the inner core boundary. So far only two models fit both the mode data and the travel time data. *Li et al.* [1991] presented a model with a higher order anisotropy which. *Tromp* [1994] presented a model based on PREM which introduces cylindrical anisotropy with the fast axis parallel to the spin axis of the Earth. It is based on the inversion of anomalous splitting for 18 modes.

We set up an experiment to try to assess whether we can see an azimuthal variation in our stacked cross-correlations. We divide our data set in two groups according to l_C, the colatitude of the pole of the great circle which goes between each pair station-event. The first group has all the great circles with l_C ranging from 0 to 45 degrees. This represents 16 stations. The second group has l_C ranging from 45 degrees to 90 degrees and represents the 18 other stations. We note that all the stations which presented a bigger amplitude in Figure 4.6 (TWO, SJG, GUA, PPT and NOU for the Fiji event) fall in the first group. The more "quiet" stations seem to belong to the second group. We stack the cross correlations in each group in the same way as described earlier after applying the $w = 1/rms\left(C_{\tilde{j}s}\right)$ weighting scheme. We show the individual cross-correlations as well as the stacks on Figure 4.19 and 4.20 for the equatorial paths and the polar paths respectively. We also show how the stack varies with each of the eleven models and the CORE11 model in Figure 4.21 and 4.22 for the two groups.

We observe the following result. The stack for the equatorial paths displays a very well defined peak at 32 seconds. This was the value observed for the stack over the entire dataset for the same time window. The stack for the polar paths does display a well defined peak. The values of t_C for the second group are smaller than the values of t_C for the first one. This indicates that the propagation in the Earth is faster for polar paths than it is for equatorial paths. This is consistent with all the observations about the anisotropy of the inner core which state that the fast axis is parallel to the spin axis of the Earth. This experiment shows that neither of our models can predict the right average shear velocity for the real Earth. We do however observe an azimuthal variation in the quality of the cross-correlations of $C_{\tilde{j}s}$ and we do observe a faster propagation along the polar directions than along the equatorial directions. The fact that we observe well defined stacked cross-correlation for the equatorial paths indicates that the inner-core shear velocity structure in our models is close to the inner-core shear velocity structure of the Earth. As we showed

earlier, the reason why the stacks do not peak at zero time-lag but around 32 seconds is probably due to the ellipiticity of the Earth. The fact the stacked cross-correlations are less well defined for the polar paths shows us that the inner-core shear velocity structure for PREM is probably far removed from the inner-core shear velocity structure of the Earth in the polar direction. This is consistent with the anisotropy model of *Tromp* [1994]. We also observe in Figure 4.21 and Figure 4.22 that the stacked cross-correlations are not different for an anisotropic model such as CORE11 or for an isotropic model such as PREM with a similar average shear velocity in the inner core as CORE11. This shows us that although there is evidence for anisotropy in the inner core of the Earth, the anisotropy is different from the type used in CORE11. This again is consistent with the model derived by *Tromp* [1994] where the anisotropy is cylindrical and not transversely isotropic such as in CORE11.

Figure Captions

Figure 4.1 : Plot of the $C_{\tilde{fs}}(t)$ for 34 different stations (bottom) and $S_{\tilde{fs}}(t)$ (top) for isolation filters and synthetic seismograms calculated with PREM. The seismograms were all band pass filtered using a cosine square filter with corner frequencies at 5 mHz and 15 mHz. The isolation filter was calculated using ε_1=0.8% and ε_2=1.2%. The cross correlations were calculated between 400 min and 700 min. The number on the left is the epicentral distance in degrees. The number on the right is t_c in seconds. We note that the individual $C_{\tilde{fs}}(t)$ do not display, in general, a cross correlation with a well defined peak at zero time lag, whereas $S_{\tilde{fs}}(t)$ does. The scatter in the position of the central peak for the $C_{\tilde{fs}}(t)$ does not seem to be correlated with distance.

Figure 4.2 : Plot of the $C_{\tilde{fs}}(t)$ for 34 different stations (bottom) and $S_{\tilde{fs}}(t)$ (top) for isolation filters calculated with PREM whereas the full synthetic seismograms were calculated with a model 3% faster in the inner core. The seismograms were all band pass filtered using a cosine square filter with corner frequencies at 5 mHz and 15 mHz. The isolation filter was calculated using ε_1=0.8% and ε_2=1.2%. The cross correlations were calculated between 300 min and 400 min. The number on the left is the epicentral distance in degrees. The number on the right is t_c in seconds. We note that the individual $C_{\tilde{fs}}(t)$ do not display, in general, a cross correlation with a well defined peak, whereas $S_{\tilde{fs}}(t)$ does. We also note that the central peak is not as symmetrical in this case as it is for the auto correlation of PREM. Nor is the amplitude of the peak as big with respect to nearby peaks. The scatter in the position of the central peak for the $C_{\tilde{fs}}(t)$ does not seem to be correlated with distance.

Figure 4.3 : Plot of the $S_{\tilde{fs}}(t)$ where the isolation filter correspond to the eleven X_i models derived from PREM with average shear velocities in the inner core which are

respectively 10% slower, 4% slower, 3% slower, 2% slower, 0% faster, 1% faster, 1.5% faster, 2% faster, 2.5% faster, 3% faster and 4% faster than PREM. The data is a complete synthetic seismogram for the model X_{10}. The cross-correlations are calculated between 500 and 800 minutes after the event start time. The isolation filters are composed of modes with a sensitivity greater than 8%. All the seismograms were band-pass filtered between 5 and 15 mHz. For the correct isolation filter, we observe a cross-correlation which peaks at zero time lag.

Figure 4.4 : Plot of the $S_{\tilde{f}s}(t)$ where the isolation filter correspond to the eleven X_i models derived from PREM with average shear velocities in the inner core which are respectively 10% slower, 4% slower, 3% slower, 2% slower, 0% faster, 1% faster, 1.5% faster, 2% faster, 2.5% faster, 3% faster and 4% faster than PREM. The data is a complete synthetic seismogram for the model CORE11. The cross-correlations are calculated between 500 and 800 minutes after the event start time. The isolation filters are composed of modes with a sensitivity greater than 8%. All the seismograms were band-pass filtered between 5 and 15 mHz. We note that the best models are the models X_9 and X_{10} which indicates the average shear velocity for CORE11 is equal to an average shear velocity about 2.6 faster than PREM.

Figure 4.5 : Plot of t_c and A calculated for the $S_{\tilde{f}s}(t)$ for the eleven X_i models. The time window used is [500;800] min and the frequency band is [5;15] mHz. We note that the best fitting model is in between the model 2.5% and the model 3% faster then PREM. It is the model for which $S_{\tilde{f}s}(t)$ has the biggest amplitude and at_c value of zero.

Figure 4.6 : Plot of all individual $C^j_{\tilde{f}s}(t)$s calculated between isolation filters obtained using a model derived from PREM which is 3% slower than PREM and real data. The cross-correlations are calculated between 400 and 700 minutes after the event start time.

The weights we assign to all the cross-correlations are all equal to 1. The cross-correlations with high amplitude are symptomatic of equatorial great circles.

Figure 4.7 : Plot of all individual $C^j_{\tilde{fs}}(t)$s calculated between isolation filters obtained using a model derived from PREM which is 3% slower than PREM and real data. The cross-correlations are calculated between 400 and 700 minutes after the event start time. The weights we assign to all the cross-correlations are all equal to $w = 1/rms\left(C_{\tilde{fs}}\right)$.

Figure 4.8 : Plot of the mean square amplitude of the $C^j_{\tilde{ff}}(t)$s, $C^j_{\tilde{fs}}(t)$s, $C^j_{\tilde{fs}}(t)$s and $C^j_{\tilde{fg}}(t)$s calculated at all the stations between 300 and 600 minutes. We note that the ratio of the mean square amplitude level between two stations is constant for all four quantities. The ratio involve synthetic seismograms and real data. This indicates that these values are characteristic of the radiation pattern and not of local factors such as ambient noise.

Figure 4.9 : Plot of the mean square amplitude of the $C^j_{\tilde{ff}}(t)$s, $C^j_{\tilde{fs}}(t)$s, $C^j_{\tilde{fs}}(t)$s and $C^j_{\tilde{fg}}(t)$s calculated at all the stations between 400 and 700 minutes. We note that the ratio of the mean square amplitude level between two stations is constant for all four quantities. The ratio involve synthetic seismograms and real data. This indicates that these values are characteristic of the radiation pattern and not of local factors such as ambient noise.

Figure 4.10 : Plot of the mean square amplitude of the $C^j_{\tilde{ff}}(t)$s, $C^j_{\tilde{fs}}(t)$s, $C^j_{\tilde{fs}}(t)$s and $C^j_{\tilde{fg}}(t)$s calculated at all the stations between 500 and 800 minutes. We note that the ratio of the mean square amplitude level between two stations is constant for all four quantities. The ratio involve synthetic seismograms and real data. This indicates that these values are characteristic of the radiation pattern and not of local factors such as ambient noise.

Figure 4.11 : Plot of the mean square amplitude of the $C^{J}_{\tilde{f}\tilde{f}}(t)$s, $C^{J}_{\tilde{f}s}(t)$s, $C^{J}_{\tilde{f}\bar{s}}(t)$s and $C^{j}_{\tilde{f}\bar{g}}(t)$s calculated at all the stations between 300 and 400 minutes. We note that the ratio of the mean square amplitude level between two stations is constant for all four quantities. The ratio involve synthetic seismograms and real data. This indicates that these values are characteristic of the radiation pattern and not of local factors such as ambient noise.

Figure 4.12 : Plot of the mean square amplitude of the $C^{J}_{\tilde{f}\tilde{f}}(t)$s, $C^{J}_{\tilde{f}s}(t)$s, $C^{J}_{\tilde{f}\bar{s}}(t)$s and $C^{j}_{\tilde{f}\bar{g}}(t)$s calculated at all the stations between 500 and 600 minutes. We note that the ratio of the mean square amplitude level between two stations is constant for all four quantities. The ratio involve synthetic seismograms and real data. This indicates that these values are characteristic of the radiation pattern and not of local factors such as ambient noise.

Figure 4.13 : Map of the mean square amplitudes of the $C^{J}_{\tilde{f}\tilde{f}}(t)$s, $C^{J}_{\tilde{f}s}(t)$s, $C^{j}_{\tilde{f}\bar{s}}(t)$s and $C^{j}_{\tilde{f}\bar{g}}(t)$s calculated at all the stations between 400 and 700 minutes at their respective location for the March 09, 1994 Fiji event. The size of the triangle is proportional to the size of $C^{J}_{\tilde{f}s}(t)$. We also display the focal mechanism at the epicenter. This shows us that their does not seem to be a correlation between the mean square amplitude of $C^{j}_{\tilde{f}s}(t)$ and either the epicentral distance of the station or a specific location of the station with respect to the epicenter.

Figure 4.14 : Map of the mean square amplitudes of the $C^{J}_{\tilde{f}\tilde{f}}(t)$s, $C^{J}_{\tilde{f}s}(t)$s, $C^{J}_{\tilde{f}\bar{s}}(t)$s and $C^{j}_{\tilde{f}\bar{g}}(t)$s calculated at all the stations between 400 and 700 minutes at their respective location for the June 09, 1994 Bolivia event. The size of the triangle is proportional to the size of $C^{j}_{\tilde{f}s}(t)$. We also display the focal mechanism at the epicenter. In this case there seems to be a correlation between the mean square amplitude of $C^{j}_{\tilde{f}s}(t)$ and the location of the station with respect to the epicenter. We note that all the stations with high mean square amplitude level are located near to the antipodal location. We also note that since this

includes data from the IRIS/POSEIDON network and from the GEOSCOPE network, this is not an artifact of the network (such as a bad scaling, ...).

Figure 4.15 : Plot of the theoretical amplitude noise spectrum used in the synthetic noise experiment. It is derived from Romanowicz and Karczewski ([1989]). We use this spectrum between 5 and 15 mHz only since we band-pass filter all our seismograms.

Figure 4.16 : Plot of all the stacked cross-correlations obtained between isolation filters calculated with PREM and full synthetic seismograms to which we add a frequency band-limited noise time series. The number on the left is equal to the ratio in percent of the root mean square of the isolation filter to the root mean square of the full synthetic seismogram without any noise. This is almost equivalent to saying that the maximum amplitude of the noise is equal to the square root of that number time the maximum amplitude of the full synthetic seismogram. The cross-correlations are calculated between 400 and 700 minutes. We see that we can add up to 55% of noise without affecting the cross-correlation. We note that the peak is always centered around 0 since we add a random phase noise so it shouldn't bias our measurement.

Figure 4.17 : Plot of the $S_{\tilde{f}s}(t)$ where the isolation filter correspond to the eleven X_i models derived from PREM with average shear velocities in the inner core which are respectively 10% slower, 4% slower, 3% slower, 2% slower, 0% faster, 1% faster, 1.5% faster, 2% faster, 2.5% faster, 3% faster and 4% faster than PREM and with CORE11. *s(t)* corresponds to the real data. The cross-correlations are calculated between 400 and 700 minutes after the event start time. The isolation filters are composed of modes with a sensitivity greater than 8%. All the seismograms were band-pass filtered between 5 and 15 mHz. We weighted the individual $C^j_{\tilde{f}s}(t)$ with $w_j = 1$. We note that the stack obtained for CORE11 has different characteristics than the stacks obtained for X9,

X_{10} and X_{11}. We note that the best model is X_3 although it fails to produce a peak centered at zero time lag.

Figure 4.18 : Plot of the $S_{\tilde{fs}}(t)$ where the isolation filter correspond to the eleven X_i models derived from PREM with average shear velocities in the inner core which are respectively 10% slower, 4% slower, 3% slower, 2% slower, 0% faster, 1% faster, 1.5% faster, 2% faster, 2.5% faster, 3% faster and 4% faster than PREM and with CORE11. *s(t)* corresponds to the real data. The cross-correlations are calculated between 400 and 700 minutes after the event start time. The isolation filters are composed of modes with a sensitivity greater than 8%. All the seismograms were band-pass filtered between 5 and 15 mHz. We weighted the individual $C^J_{\tilde{fs}}(t)$ with $w_J = 1/rms\left(C_{\tilde{fs}}\right)$. We note that now all the stacks obtained for CORE11, X_9, X_{10} and X_{11} share the same characteristics. We note that the best model is X_3 although it fails to produce a peak centered at zero time lag.

Figure 4.19 : Individual and stacked cross-correlation obtained for isolation filters calculated with a model 3% slower than PREM and real data. We have selected all the great circles for which l_C, the colatitude of the pole, is between 0 and 45 degrees. This amounts to choosing the equatorial paths versus the polar paths. We weighted the individual $C^J_{\tilde{fs}}(t)$ inversely to the root mean square of the cross-correlations. The cross-correlations are well defined. We note that these paths include most of the stations which had a large value of the mean square of $C^J_{\tilde{fs}}(t)$.

Figure 4.20 : Individual and stacked cross-correlation obtained for isolation filters calculated with a model 3% slower than PREM and real data. We have selected all the great circles for which l_C, the colatitude of the pole, is between 45 and 90 degrees. This amounts to choosing the polar paths versus the equatorial paths. We weighted the

individual $C^j_{\tilde{fs}}(t)$ inversely to the root mean square of the cross-correlations. We note that the cross-correlations are not so well defined as in Figure 4.19. We also note that these paths include most o the stations which had a small value of the mean square of $C^j_{\tilde{fs}}(t)$.

Figure 4.21 : Plot of the $S_{\tilde{fs}}(t)$ where the isolation filter correspond to the eleven X_i models derived from PREM with average shear velocities in the inner core which are respectively 10% slower, 4% slower, 3% slower, 2% slower, 0% faster, 1% faster, 1.5% faster, 2% faster, 2.5% faster, 3% faster and 4% faster than PREM and CORE11. *s(t)* corresponds to the real data. The cross-correlations are calculated between 400 and 700 minutes after the event start time. The isolation filters are composed of modes with a sensitivity greater than 8%. All the seismograms were band-pass filtered between 5 and 15 mHz. We have selected all the great circles for which l_C, the colatitude of the pole, is between 0 and 45 degrees. We weighted the individual $C^j_{\tilde{fs}}(t)$ inversely to the root mean square of the cross-correlations to remove any possible bias introduced by the surface waves. We note that the best model is X_3 which indicates the average shear velocity for the real Earth for equatorial paths is equal to an average shear velocity about 3% slower than PREM. Note how t_C never reaches 0. This indicates that our model is too far away from the real Earth to correct for the phase delay.

Figure 4.22 : Plot of the $S_{\tilde{fs}}(t)$ where the isolation filter correspond to the eleven X_i models derived from PREM with average shear velocities in the inner core which are respectively 10% slower, 4% slower, 3% slower, 2% slower, 0% faster, 1% faster, 1.5% faster, 2% faster, 2.5% faster, 3% faster and 4% faster than PREM and CORE11. *s(t)* corresponds to the real data. The cross-correlations are calculated between 400 and 700 minutes after the event start time. The isolation filters are composed of modes with a sensitivity greater than 8%. All the seismograms were band-pass filtered between 5 and 15 mHz. We have selected all the great circles for which l_C, the colatitude of the pole, is

between 45 and 90 degrees. We weighted the individual $C^{j}_{\tilde{f}s}(t)$ inversely to the root mean square of the cross-correlations. None of the models produces a satisfactory cross-correlation, which indicates how far away our model is from the real Earth.

Figure 4.23 : Plot of the $S_{\tilde{g}s}(t)$ where the isolation filter correspond to the eleven X_i models derived from PREM with average shear velocities in the inner core which are respectively 10% slower, 4% slower, 3% slower, 2% slower, 0% faster, 1% faster, 1.5% faster, 2% faster, 2.5% faster, 3% faster and 4% faster than PREM and CORE11. *s(t)* corresponds to the real data. The cross-correlations are calculated between 400 and 700 minutes after the event start time. The isolation filters are composed of modes with a sensitivity greater than 8%. All the seismograms were band-pass filtered between 5 and 15 mHz. We weighted the individual $C^{j}_{\tilde{f}s}(t)$ inversely to the root mean square of the cross-correlations. We observe that the signature from the complementary part of our models is constant with respect to changes in the inner core. We also observe that the complementary part of our models are systematically fast with respect to the real Earth. Ellipticity of the real Earth may be a possible explanation for this observation.

Figure 4.24 : Plot of the $S_{\tilde{g}s}(t)$ where the isolation filter correspond to the eleven X_i models derived from PREM with average shear velocities in the inner core which are respectively 10% slower, 4% slower, 3% slower, 2% slower, 0% faster, 1% faster, 1.5% faster, 2% faster, 2.5% faster, 3% faster and 4% faster than PREM and CORE11. *s(t)* corresponds to the real data. The cross-correlations are calculated between 400 and 700 minutes after the event start time. The isolation filters are composed of modes with a sensitivity greater than 8%. All the seismograms were band-pass filtered between 5 and 15 mHz. We have selected all the great circles for which l_C, the colatitude of the pole, is between 0 and 45 degrees. We weighted the individual $C^{j}_{\tilde{f}s}(t)$ inversely to the root mean square of the cross-correlations. We observe that the signature from the complementary

part of our models is constant with respect to changes in the inner core. We also observe that the complementary part of our models are systematically fast with respect to the real Earth. Ellipticity of the real Earth may be a possible explanation for this observation.

Figure 4.23 : Plot of the $S_{\tilde{g}s}(t)$ where the isolation filter correspond to the eleven X_i models derived from PREM with average shear velocities in the inner core which are respectively 10% slower, 4% slower, 3% slower, 2% slower, 0% faster, 1% faster, 1.5% faster, 2% faster, 2.5% faster, 3% faster and 4% faster than PREM and CORE11. *s(t)* corresponds to the real data. The cross-correlations are calculated between 400 and 700 minutes after the event start time. The isolation filters are composed of modes with a sensitivity greater than 8%. All the seismograms were band-pass filtered between 5 and 15 mHz. We have selected all the great circles for which l_C, the colatitude of the pole, is between 45 and 90 degrees. We weighted the individual $C^j_{\tilde{f}s}(t)$ inversely to the root mean square of the cross-correlations. We observe that the signature from the complementary part of our models is constant with respect to changes in the inner core. We also observe that the complementary part of our models are systematically fast with respect to the real Earth. Ellipticity of the real Earth may be a possible explanation for this observation.

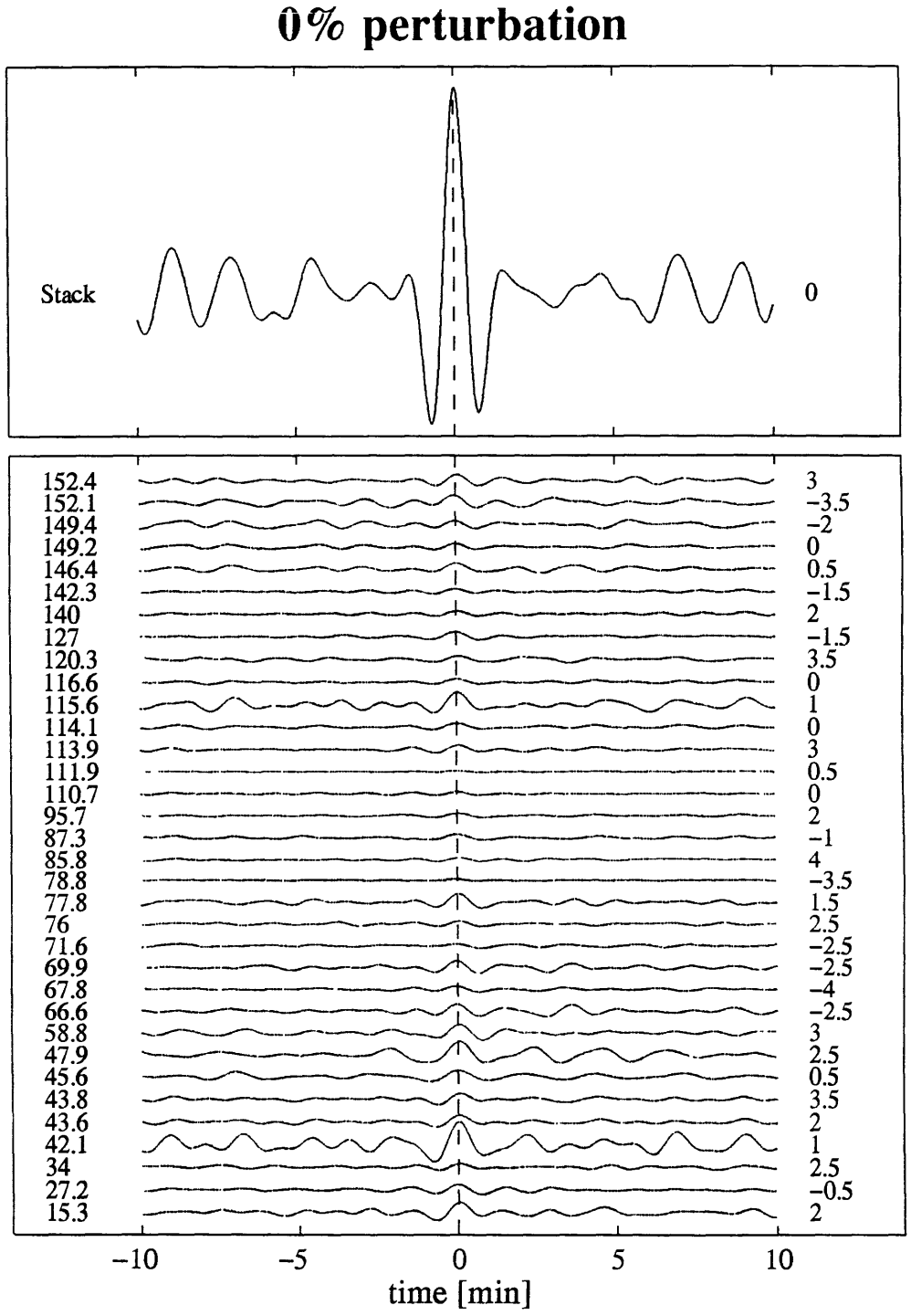
0% perturbation
Stack
0
152.4 3
152.1 −3.5
149.4 −2
149.2 0
146.4 0.5
142.3 −1.5
140 2
127 −1.5
120.3 3.5
116.6 0
115.6 1
114.1 0
113.9 3
111.9 0.5
110.7 0
95.7 2
87.3 −1
85.8 4
78.8 −3.5
77.8 1.5
76 2.5
71.6 −2.5
69.9 −2.5
67.8 −4
66.6 −2.5
58.8 3
47.9 2.5
45.6 0.5
43.8 3.5
43.6 2
42.1 1
34 2.5
27.2 −0.5
15.3 2
−10
−5
0
5
10
time [min]

Figure 4.1

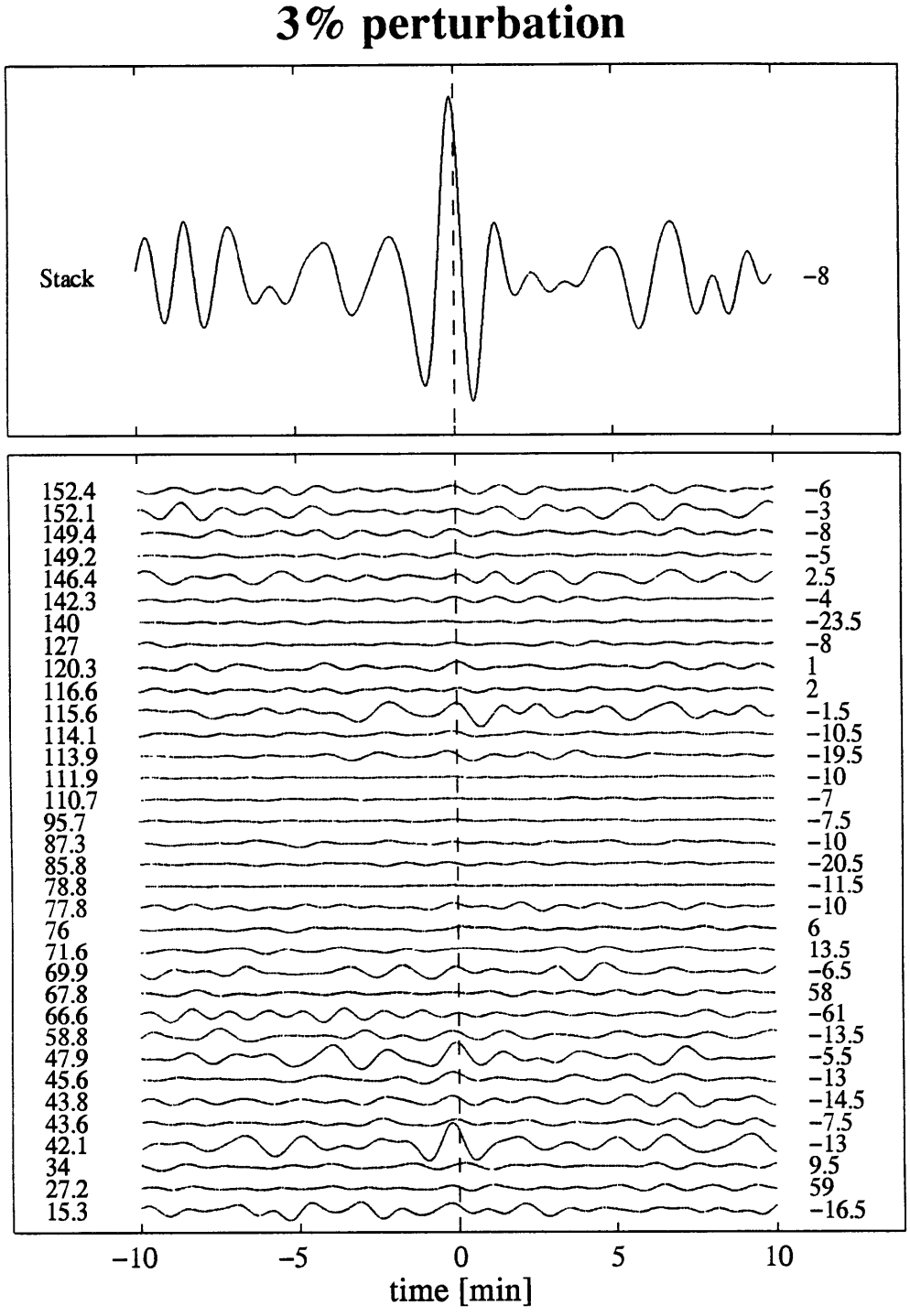
3% perturbation
Stack
-8
152.4 -6
152.1 -3
149.4 -8
149.2 -5
146.4 2.5
142.3 -4
140 -23.5
127 -8
120.3 1
116.6 2
115.6 -1.5
114.1 -10.5
113.9 -19.5
111.9 -10
110.7 -7
95.7 -7.5
87.3 -10
85.8 -20.5
78.8 -11.5
77.8 -10
76 6
71.6 13.5
69.9 -6.5
67.8 58
66.6 -61
58.8 -13.5
47.9 -5.5
45.6 -13
43.8 -14.5
43.6 -7.5
42.1 -13
34 9.5
27.2 59
15.3 -16.5
-10
-5
0
5
10
time [min]

Figure 4.2

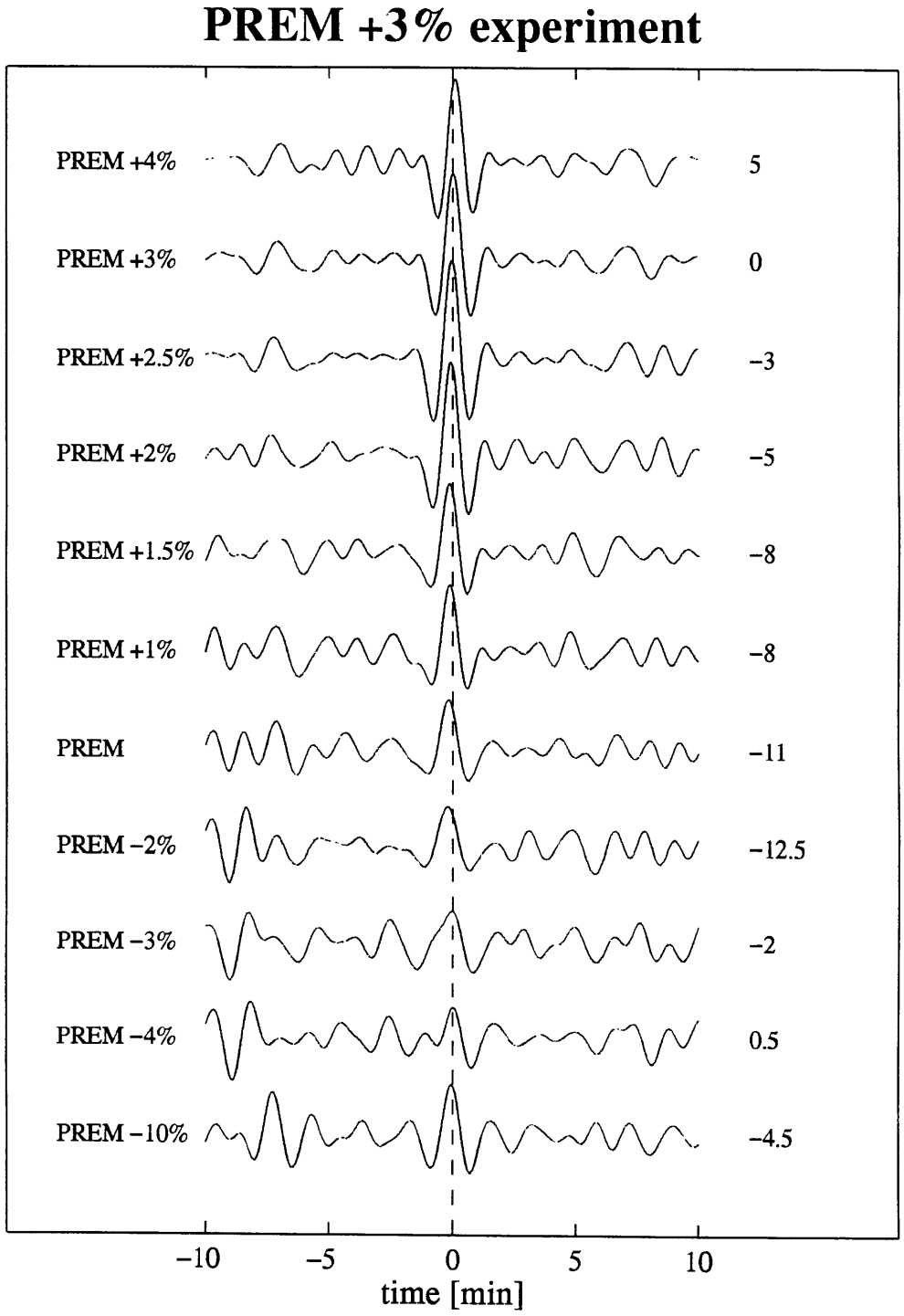
PREM +3% experiment
PREM +4%
PREM +3%
PREM +2.5%
PREM +2%
PREM +1.5%
PREM +1%
PREM
PREM −2%
PREM −3%
PREM −4%
PREM −10%
5
0
−3
−5
−8
−8
−11
−12.5
−2
0.5
−4.5
−10
−5
0
5
10
time [min]

Figure 4.3

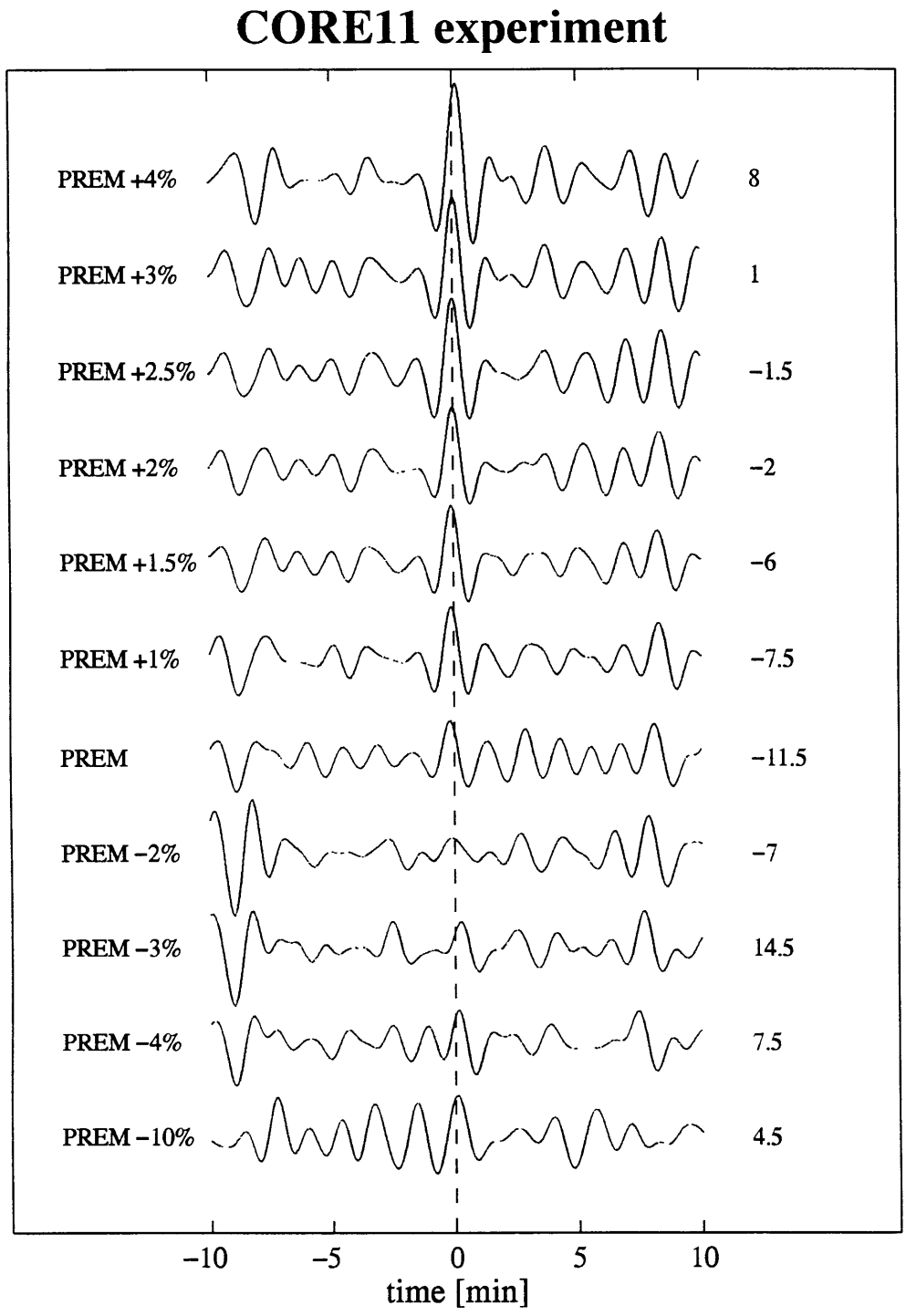
CORE11 experiment
PREM +4%
PREM +3%
PREM +2.5%
PREM +2%
PREM +1.5%
PREM +1%
PREM
PREM −2%
PREM −3%
PREM −4%
PREM −10%
8
1
−1.5
−2
−6
−7.5
−11.5
−7
14.5
7.5
4.5
−10
−5
0
5
10
time [min]

Figure 4.4

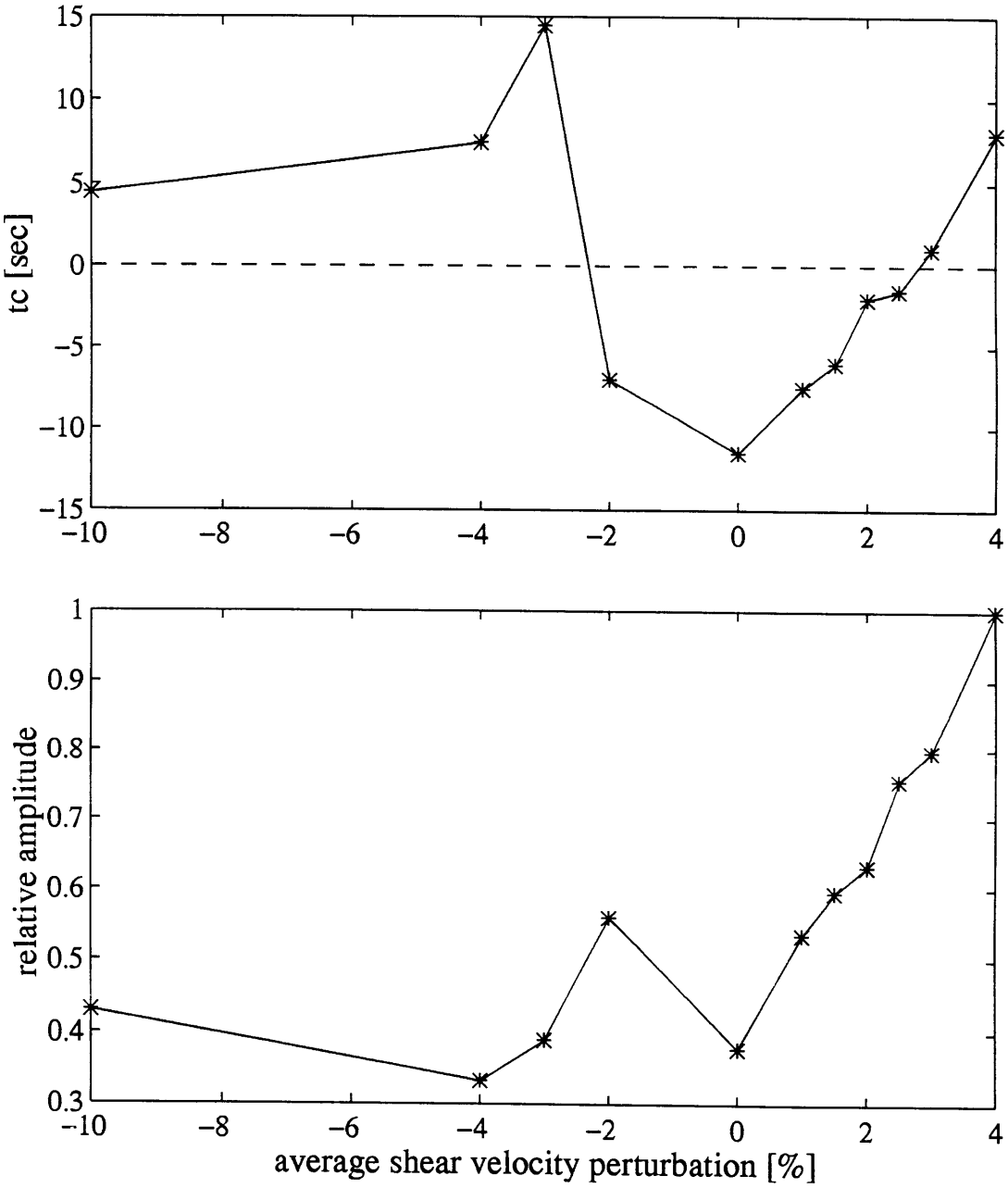
CORE11 experiment
tc [sec]
15
10
5
0
−5
−10
−15
−10
−8
−6
−4
−2
0
2
4
relative amplitude
1
0.9
0.8
0.7
0.6
0.5
0.4
0.3
−10
−8
−6
−4
−2
0
2
4
average shear velocity perturbation [%]

Figure 4.5

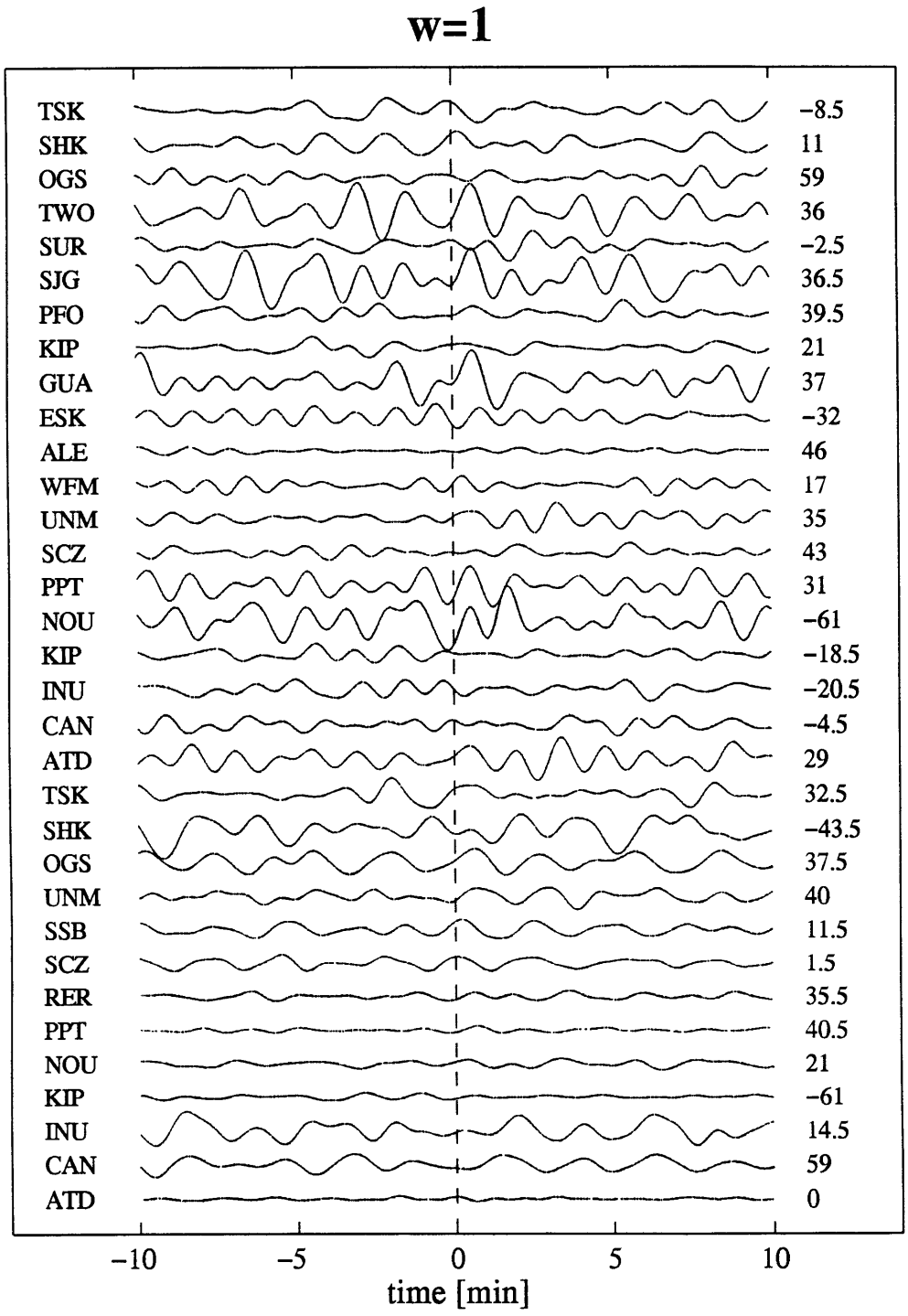
w=1
TSK
SHK
OGS
TWO
SUR
SJG
PFO
KIP
GUA
ESK
ALE
WFM
UNM
SCZ
PPT
NOU
KIP
INU
CAN
ATD
TSK
SHK
OGS
UNM
SSB
SCZ
RER
PPT
NOU
KIP
INU
CAN
ATD
-8.5
11
59
36
-2.5
36.5
39.5
21
37
-32
46
17
35
43
31
-61
-18.5
-20.5
-4.5
29
32.5
-43.5
37.5
40
11.5
1.5
35.5
40.5
21
-61
14.5
59
0
-10
-5
0
5
10
time [min]

Figure 4.6

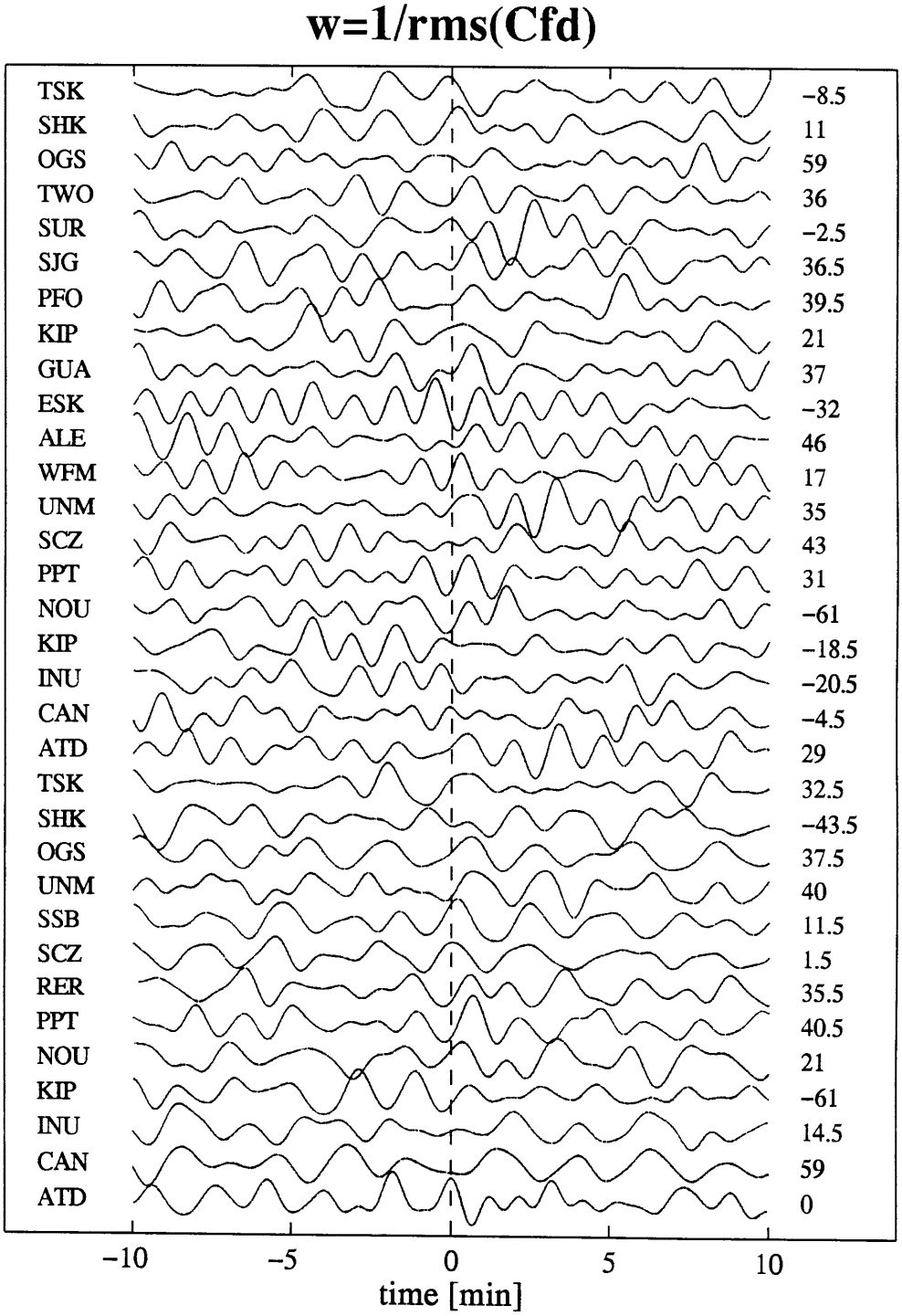
w=1/rms(Cfd)
TSK
SHK
OGS
TWO
SUR
SJG
PFO
KIP
GUA
ESK
ALE
WFM
UNM
SCZ
PPT
NOU
KIP
INU
CAN
ATD
TSK
SHK
OGS
UNM
SSB
SCZ
RER
PPT
NOU
KIP
INU
CAN
ATD
-8.5
11
59
36
-2.5
36.5
39.5
21
37
-32
46
17
35
43
31
-61
-18.5
-20.5
-4.5
29
32.5
-43.5
37.5
40
11.5
1.5
35.5
40.5
21
-61
14.5
59
0
-10
-5
0
5
10
time [min]

Figure 4.7

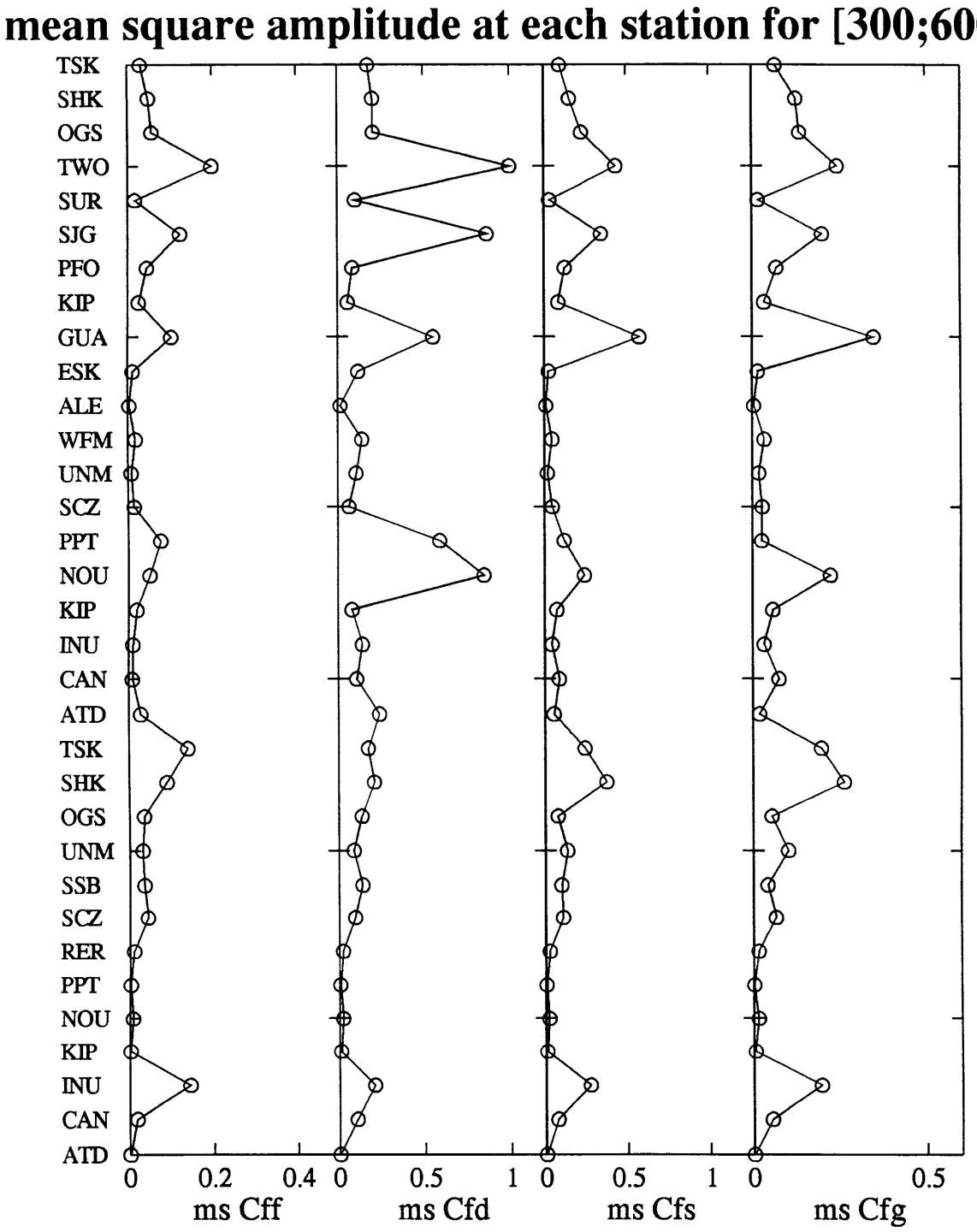
mean square amplitude at each station for [300;600]
TSK
SHK
OGS
TWO
SUR
SJG
PFO
KIP
GUA
ESK
ALE
WFM
UNM
SCZ
PPT
NOU
KIP
INU
CAN
ATD
TSK
SHK
OGS
UNM
SSB
SCZ
RER
PPT
NOU
KIP
INU
CAN
ATD
0 0.2 0.4
ms Cff
0 0.5 1
ms Cfd
0 0.5 1
ms Cfs
0 0.5
ms Cfg

Figure 4.8

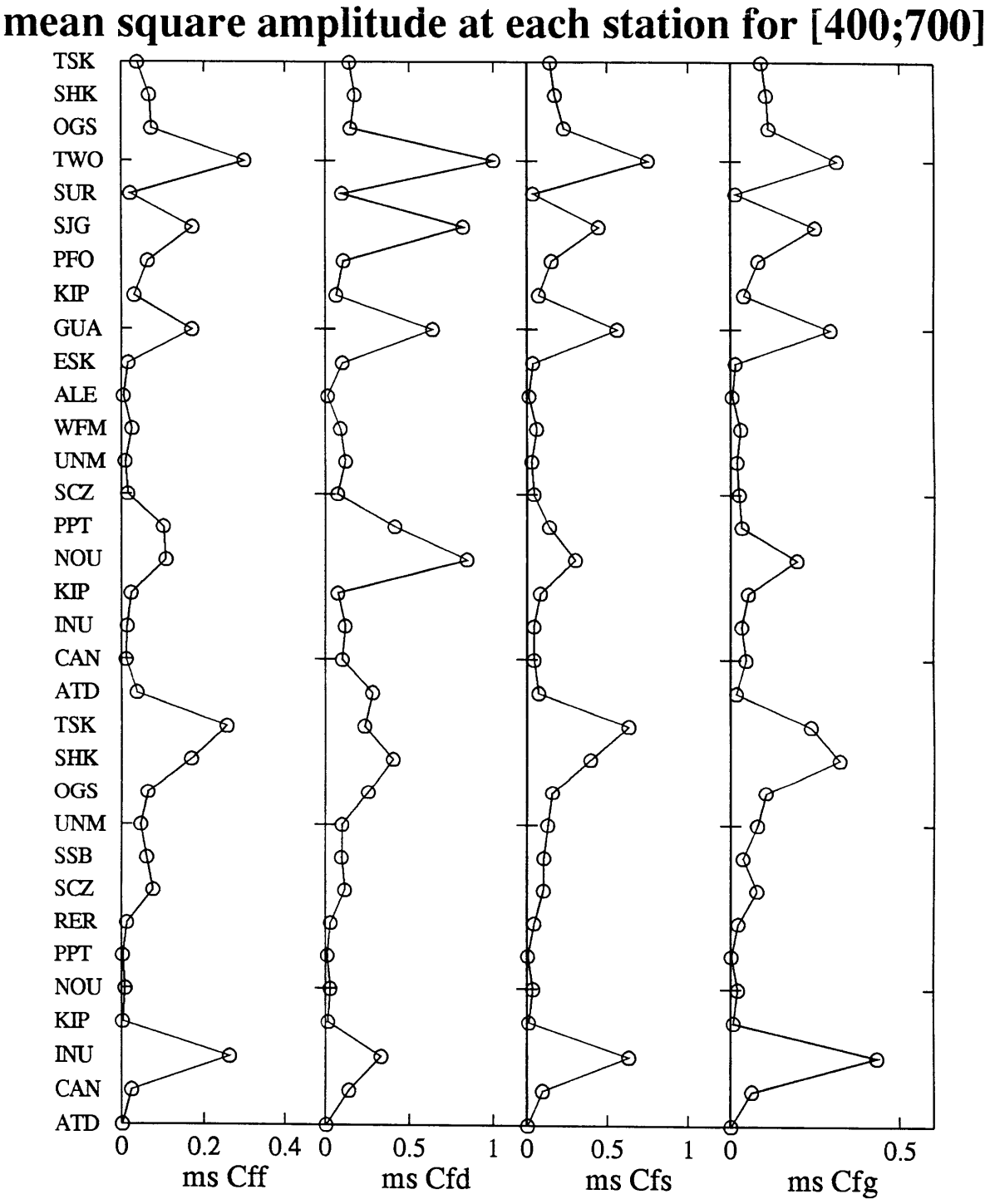
mean square amplitude at each station for [400;700]
TSK
SHK
OGS
TWO
SUR
SJG
PFO
KIP
GUA
ESK
ALE
WFM
UNM
SCZ
PPT
NOU
KIP
INU
CAN
ATD
TSK
SHK
OGS
UNM
SSB
SCZ
RER
PPT
NOU
KIP
INU
CAN
ATD
0
0.2
0.4
ms Cff
0
0.5
1
ms Cfd
0
0.5
1
ms Cfs
0
0.5
ms Cfg

Figure 4.9

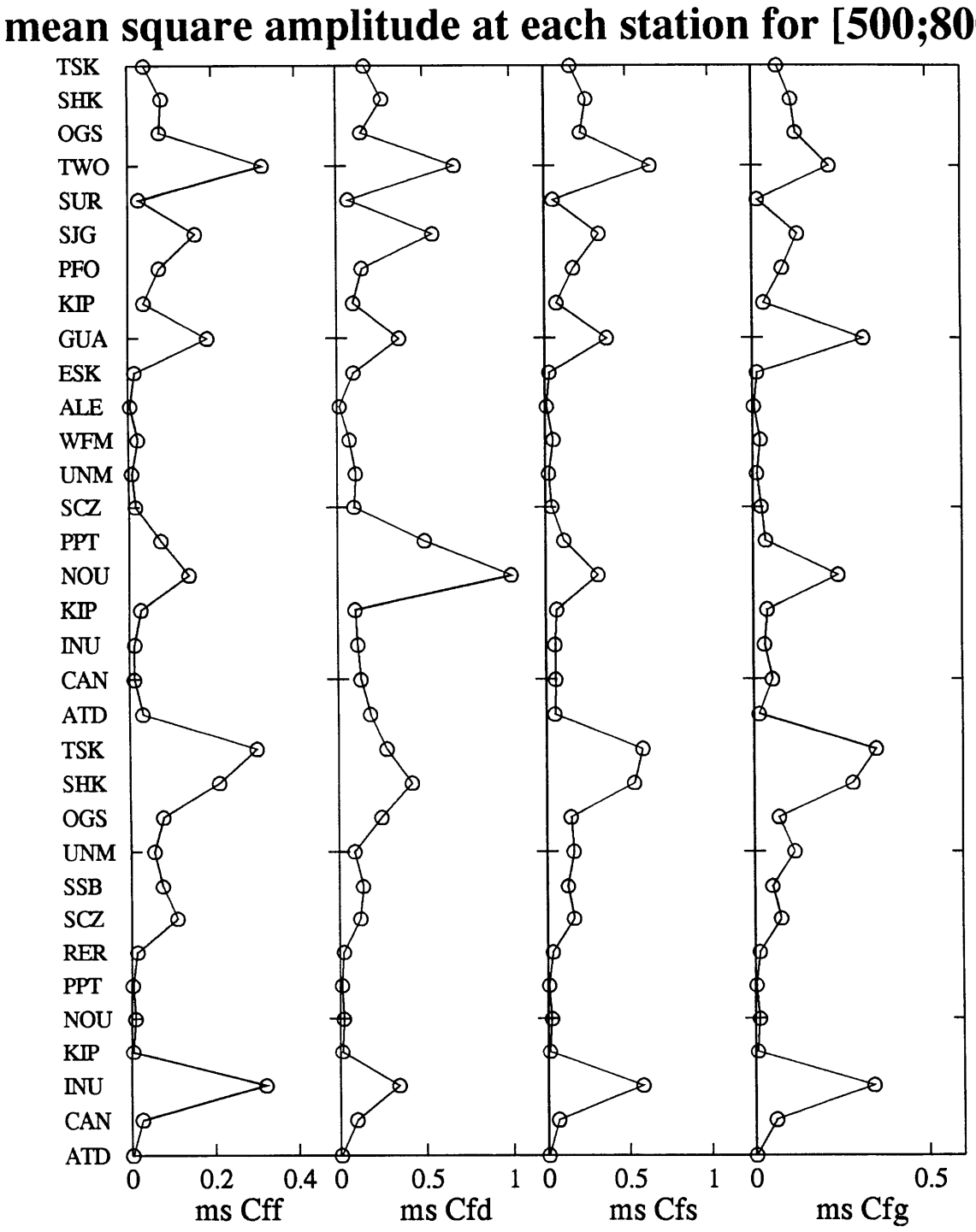
mean square amplitude at each station for [500;800]
TSK
SHK
OGS
TWO
SUR
SJG
PFO
KIP
GUA
ESK
ALE
WFM
UNM
SCZ
PPT
NOU
KIP
INU
CAN
ATD
TSK
SHK
OGS
UNM
SSB
SCZ
RER
PPT
NOU
KIP
INU
CAN
ATD
0 0.2 0.4
ms Cff
0 0.5 1
ms Cfd
0 0.5 1
ms Cfs
0 0.5
ms Cfg

Figure 4.10

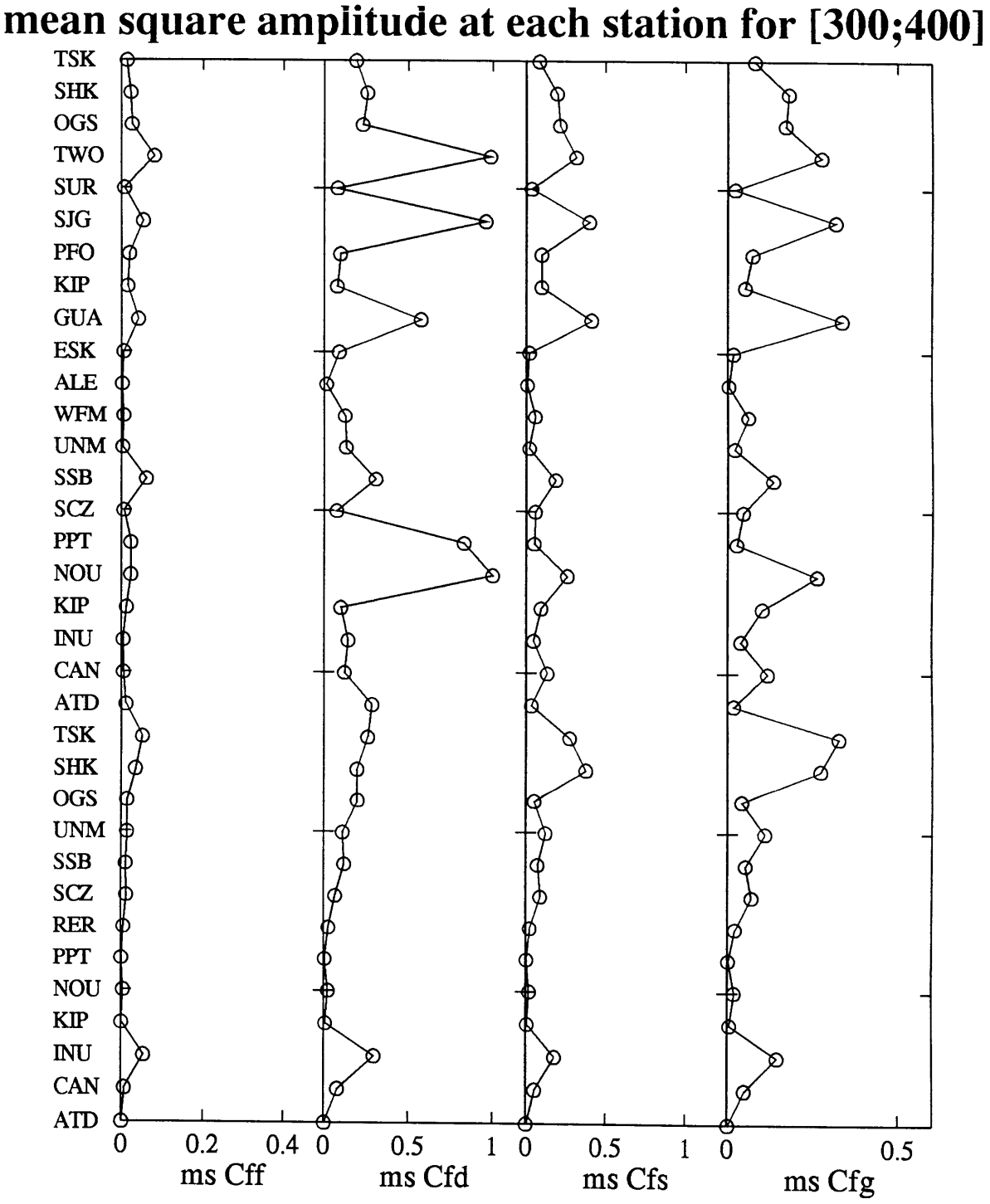
mean square amplitude at each station for [300;400]
TSK
SHK
OGS
TWO
SUR
SJG
PFO
KIP
GUA
ESK
ALE
WFM
UNM
SSB
SCZ
PPT
NOU
KIP
INU
CAN
ATD
TSK
SHK
OGS
UNM
SSB
SCZ
RER
PPT
NOU
KIP
INU
CAN
ATD
0
0.2
0.4
ms Cff
0
0.5
1
ms Cfd
0
0.5
1
ms Cfs
0
0.5
ms Cfg

Figure 4.11

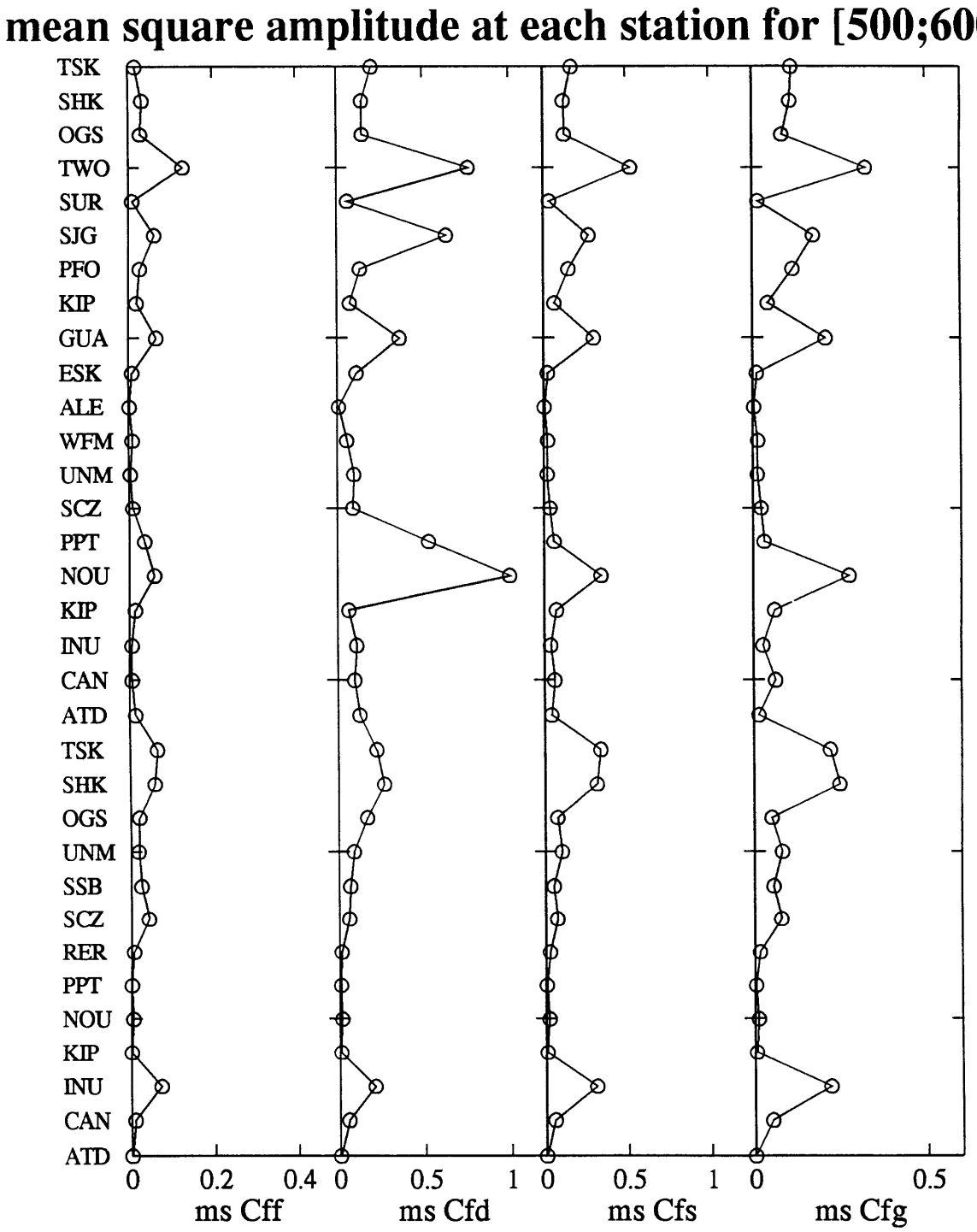
mean square amplitude at each station for [500;600]
TSK
SHK
OGS
TWO
SUR
SJG
PFO
KIP
GUA
ESK
ALE
WFM
UNM
SCZ
PPT
NOU
KIP
INU
CAN
ATD
TSK
SHK
OGS
UNM
SSB
SCZ
RER
PPT
NOU
KIP
INU
CAN
ATD
0 0.2 0.4
ms Cff
0 0.5 1
ms Cfd
0 0.5 1
ms Cfs
0 0.5
ms Cfg

Figure 4.12

March 09, 1994 Fiji event

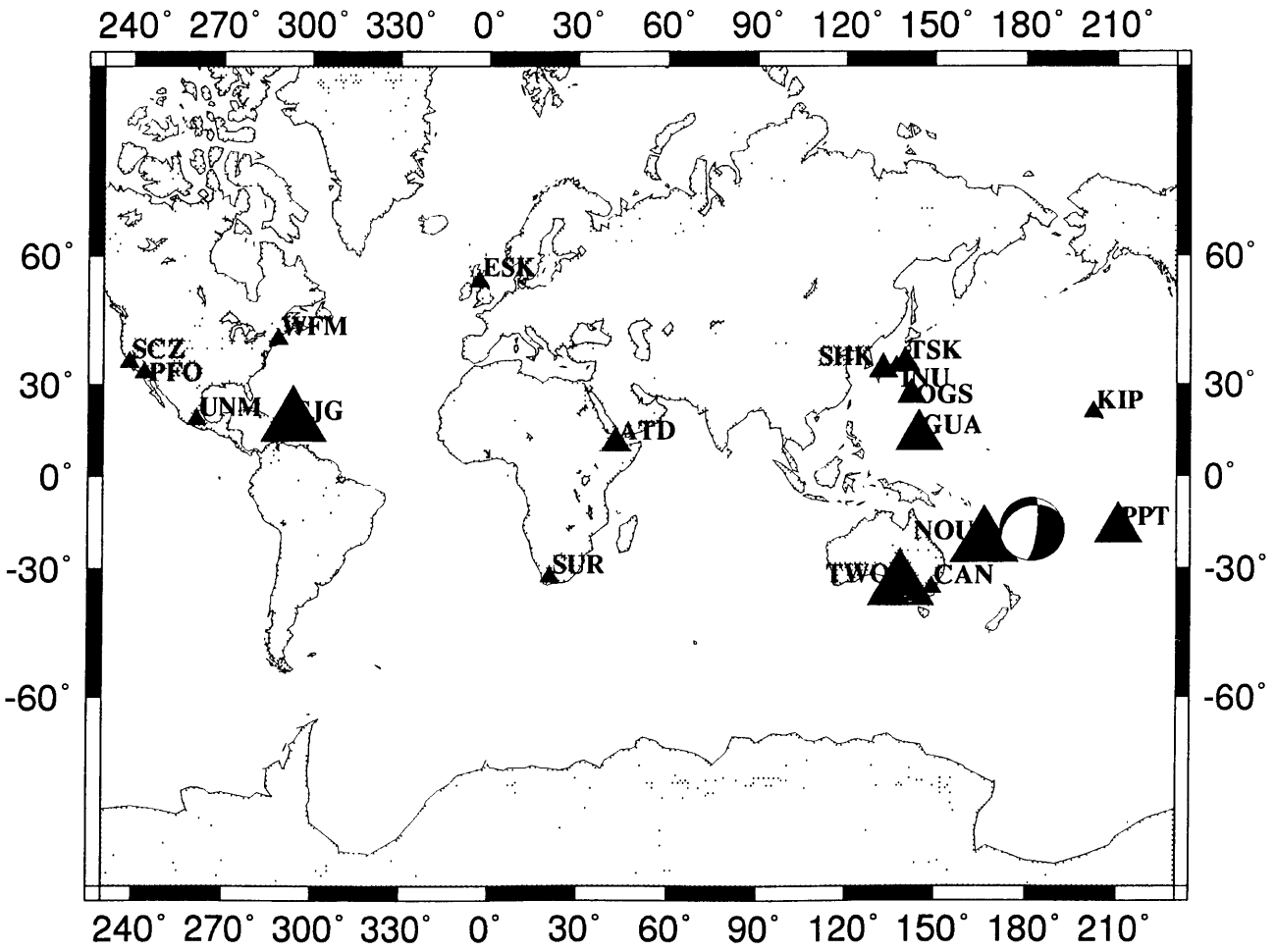

Figure 4.13

June 09, 1994 Bolivia event

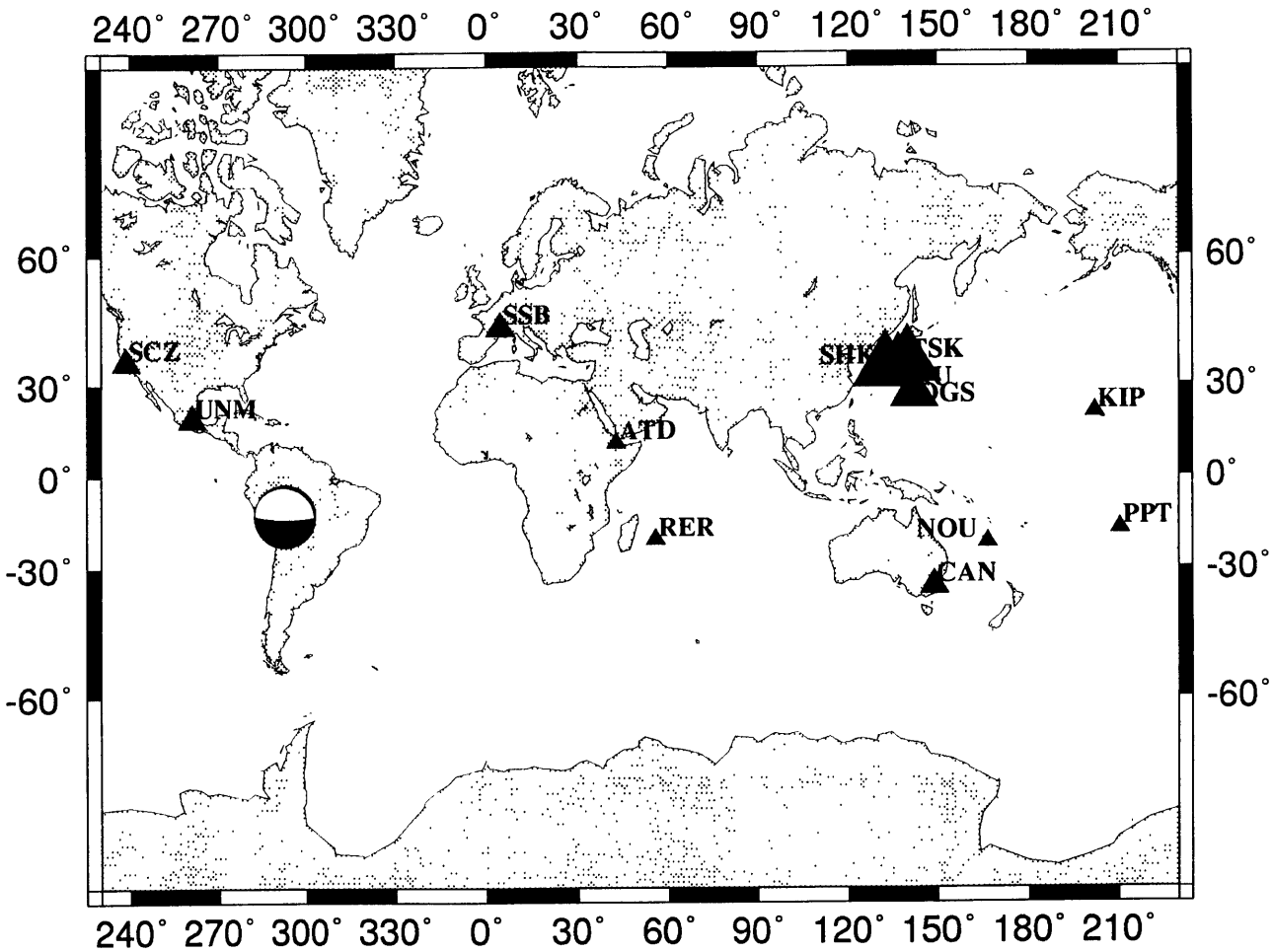

Figure 4.14

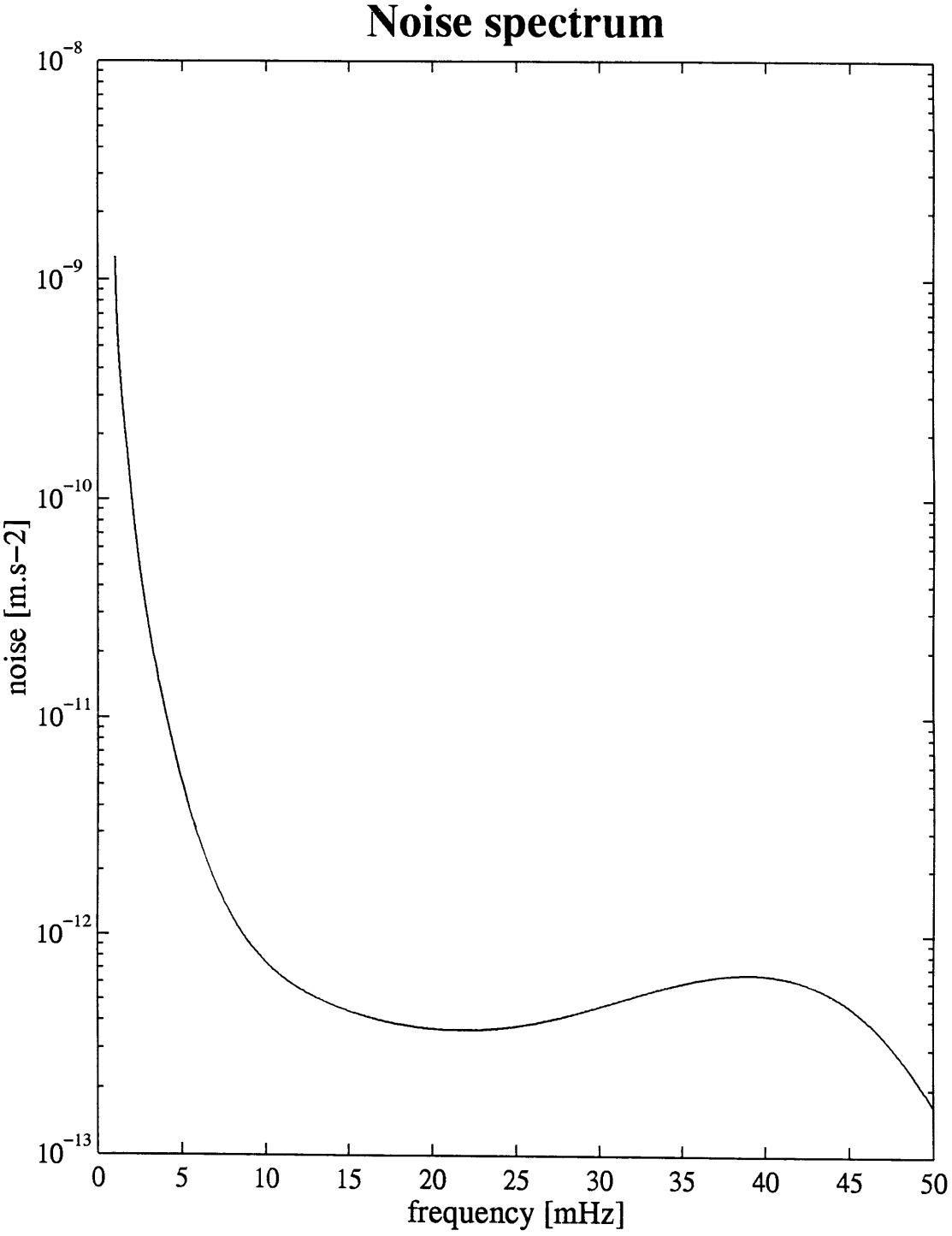
Noise spectrum
noise [m.s-2]
frequency [mHz]
10^-8
10^-9
10^-10
10^-11
10^-12
10^-13
0
5
10
15
20
25
30
35
40
45
50

Figure 4.15

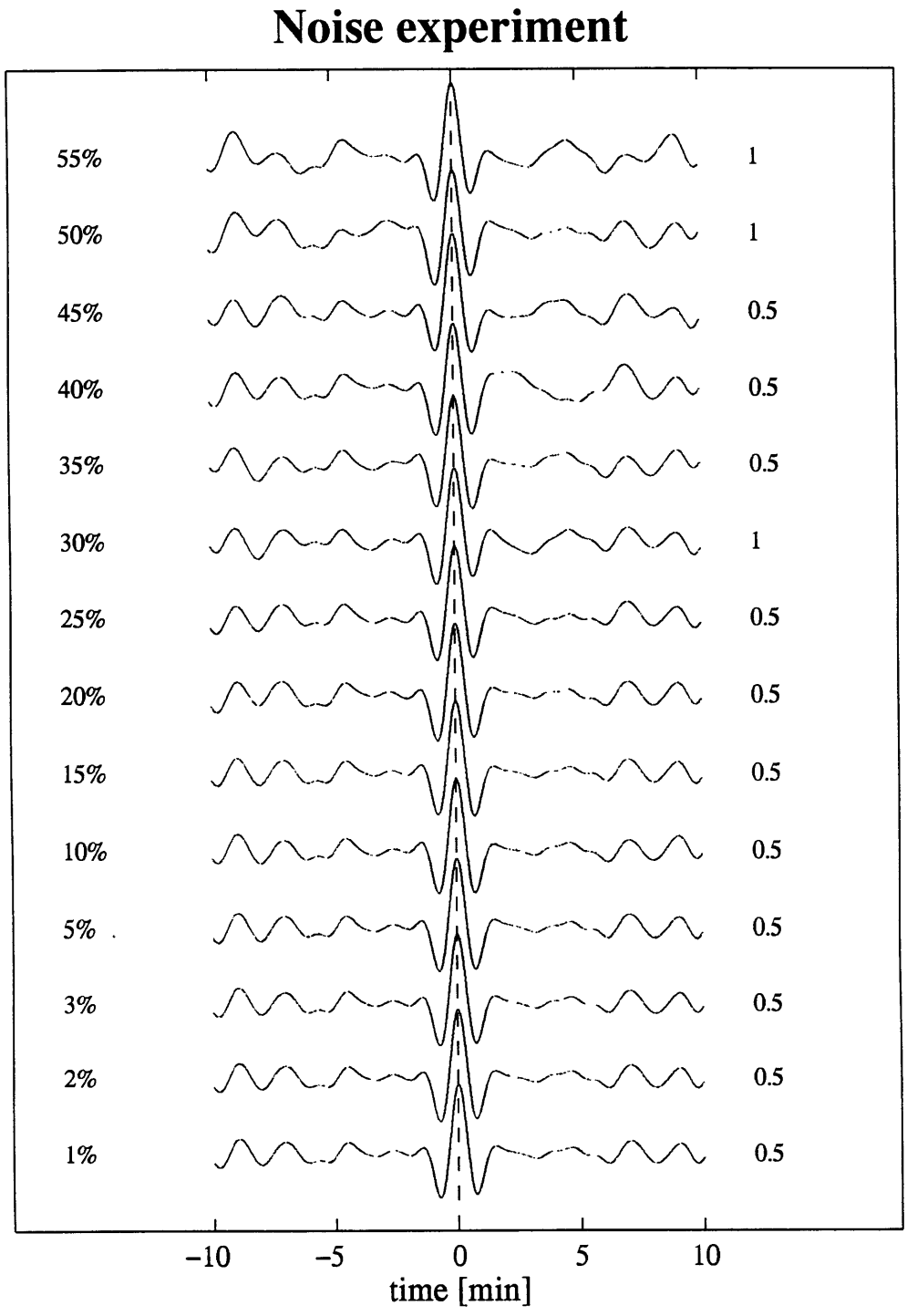
Noise experiment
55%
50%
45%
40%
35%
30%
25%
20%
15%
10%
5%
3%
2%
1%
1
1
0.5
0.5
0.5
1
0.5
0.5
0.5
0.5
0.5
0.5
0.5
−10
−5
0
5
10
time [min]

Figure 4.16

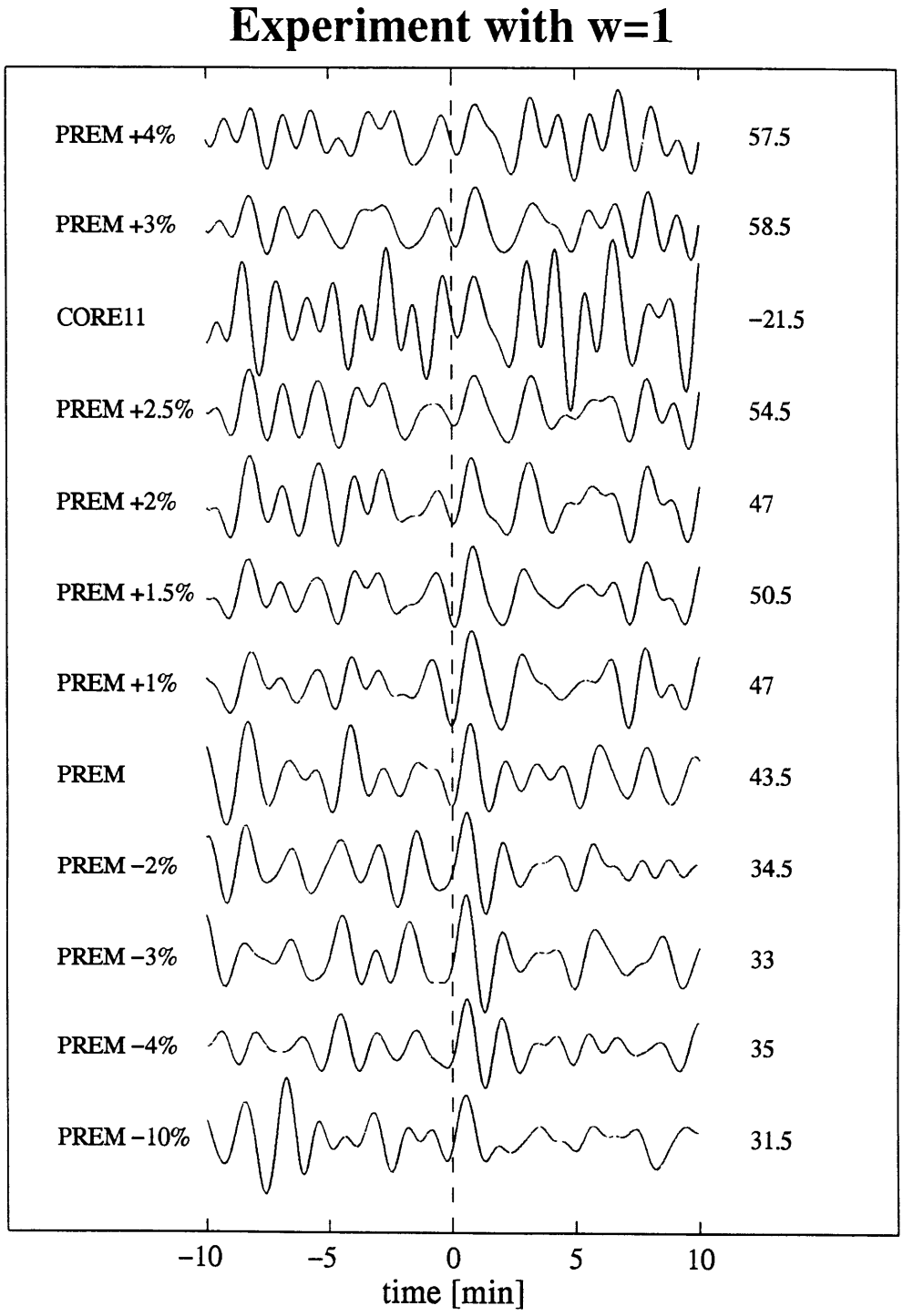
Experiment with w=1
PREM +4%
57.5
PREM +3%
58.5
CORE11
-21.5
PREM +2.5%
54.5
PREM +2%
47
PREM +1.5%
50.5
PREM +1%
47
PREM
43.5
PREM -2%
34.5
PREM -3%
33
PREM -4%
35
PREM -10%
31.5
-10
-5
0
5
10
time [min]

Figure 4.17

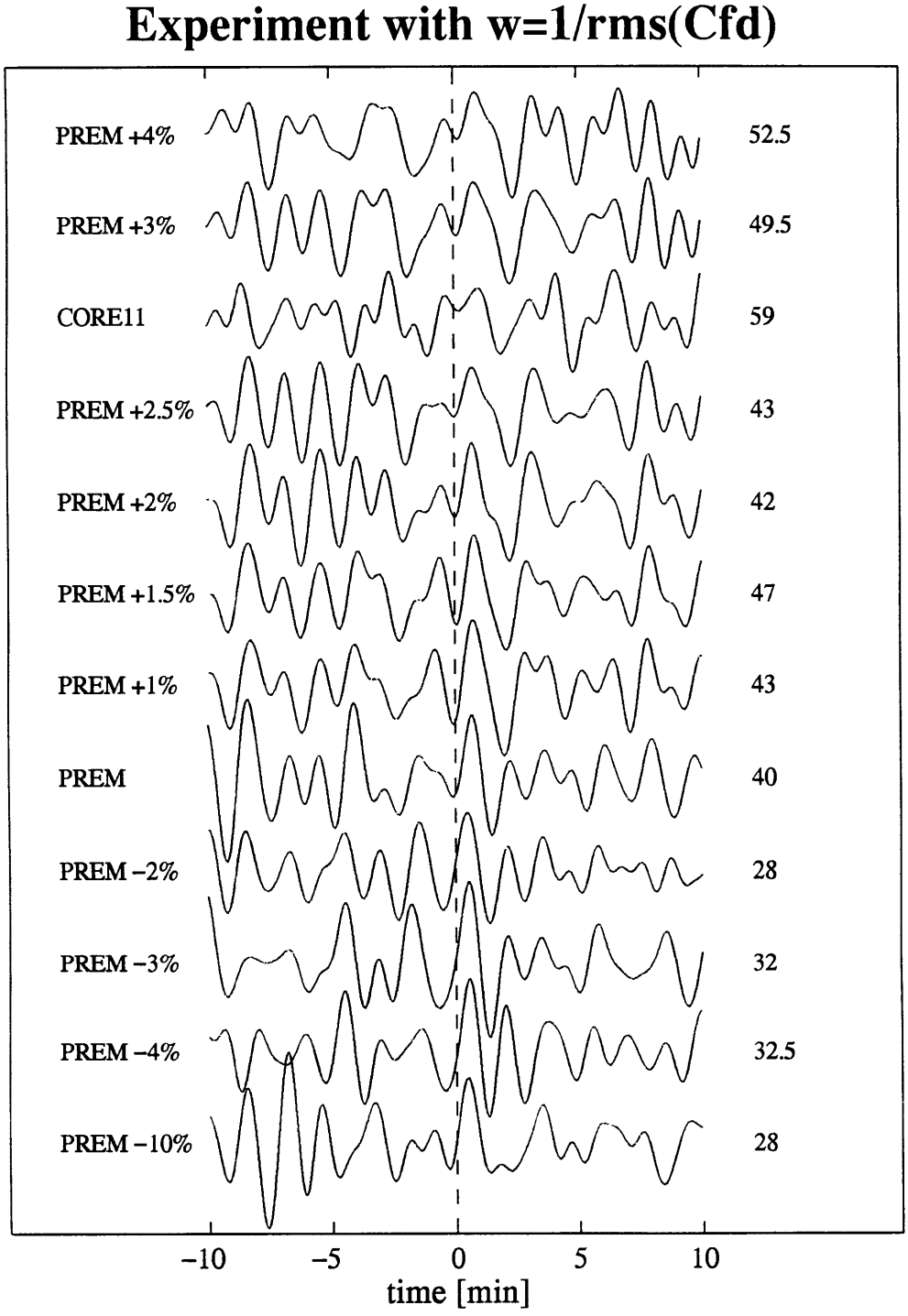
Experiment with w=1/rms(Cfd)
PREM +4%
PREM +3%
CORE11
PREM +2.5%
PREM +2%
PREM +1.5%
PREM +1%
PREM
PREM −2%
PREM −3%
PREM −4%
PREM −10%
52.5
49.5
59
43
42
47
43
40
28
32
32.5
28
−10
−5
0
5
10
time [min]

Figure 4.18

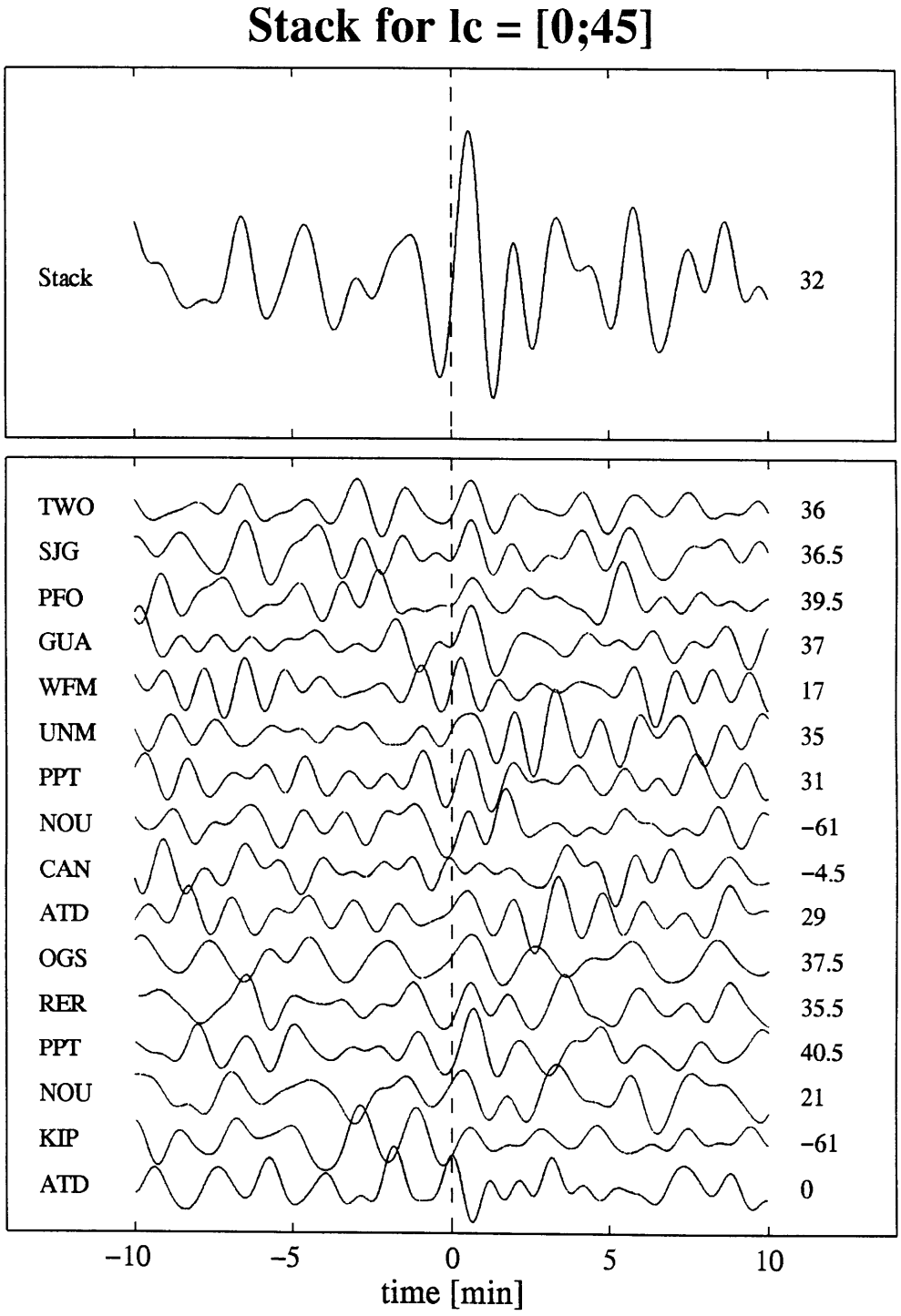
Stack for lc = [0;45]
Stack
32
TWO
SJG
PFO
GUA
WFM
UNM
PPT
NOU
CAN
ATD
OGS
RER
PPT
NOU
KIP
ATD
36
36.5
39.5
37
17
35
31
-61
-4.5
29
37.5
35.5
40.5
21
-61
0
-10
-5
0
5
10
time [min]

Figure 4.19

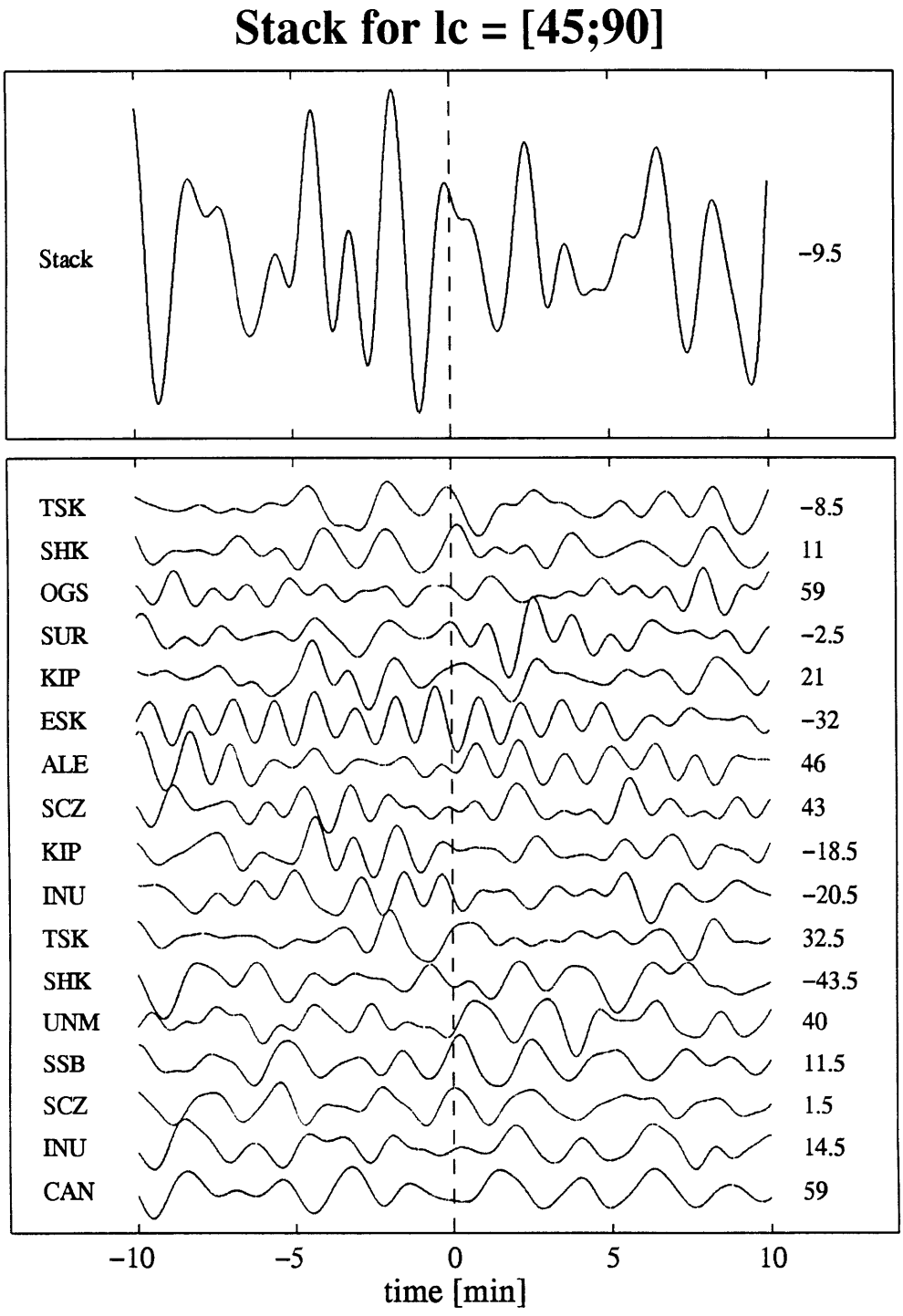
Stack for lc = [45;90]
Stack
-9.5
TSK
SHK
OGS
SUR
KIP
ESK
ALE
SCZ
KIP
INU
TSK
SHK
UNM
SSB
SCZ
INU
CAN
-8.5
11
59
-2.5
21
-32
46
43
-18.5
-20.5
32.5
-43.5
40
11.5
1.5
14.5
59
-10
-5
0
5
10
time [min]

Figure 4.20

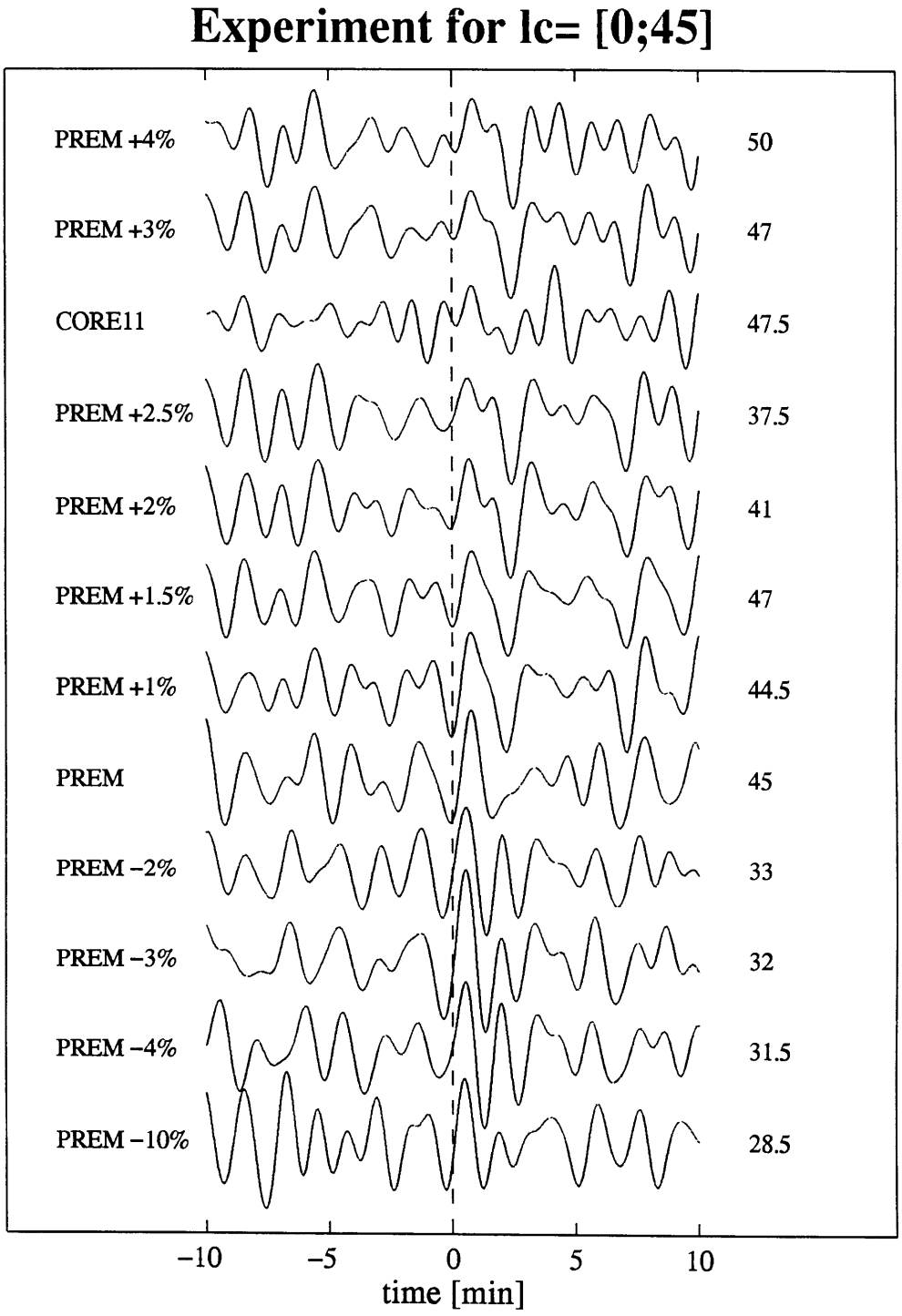
Experiment for lc= [0;45]
PREM +4%
PREM +3%
CORE11
PREM +2.5%
PREM +2%
PREM +1.5%
PREM +1%
PREM
PREM −2%
PREM −3%
PREM −4%
PREM −10%
50
47
47.5
37.5
41
47
44.5
45
33
32
31.5
28.5
−10
−5
0
5
10
time [min]

Figure 4.21

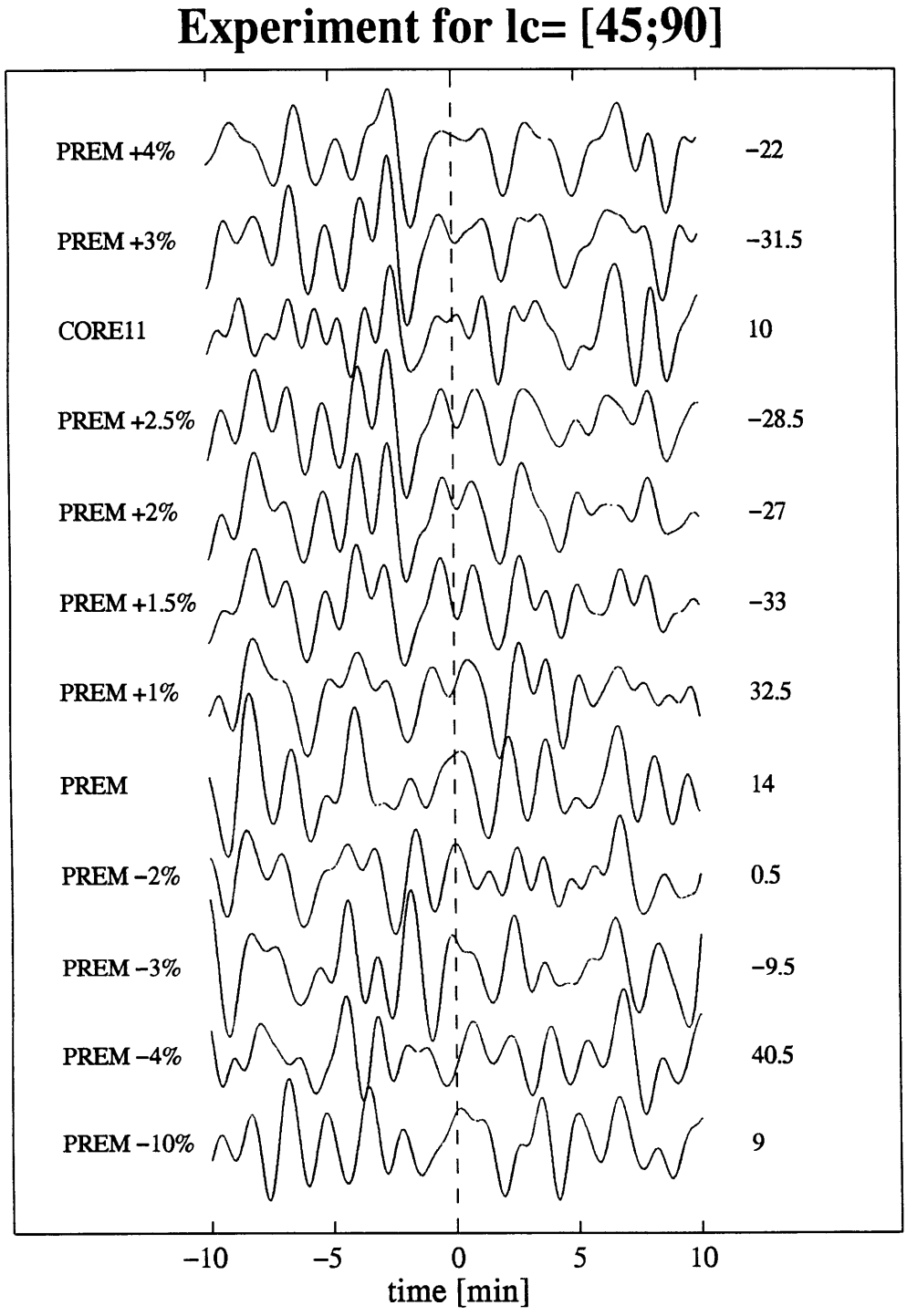
Experiment for lc= [45;90]
PREM +4%
PREM +3%
CORE11
PREM +2.5%
PREM +2%
PREM +1.5%
PREM +1%
PREM
PREM -2%
PREM -3%
PREM -4%
PREM -10%
-22
-31.5
10
-28.5
-27
-33
32.5
14
0.5
-9.5
40.5
9
-10
-5
0
5
10
time [min]

Figure 4.22

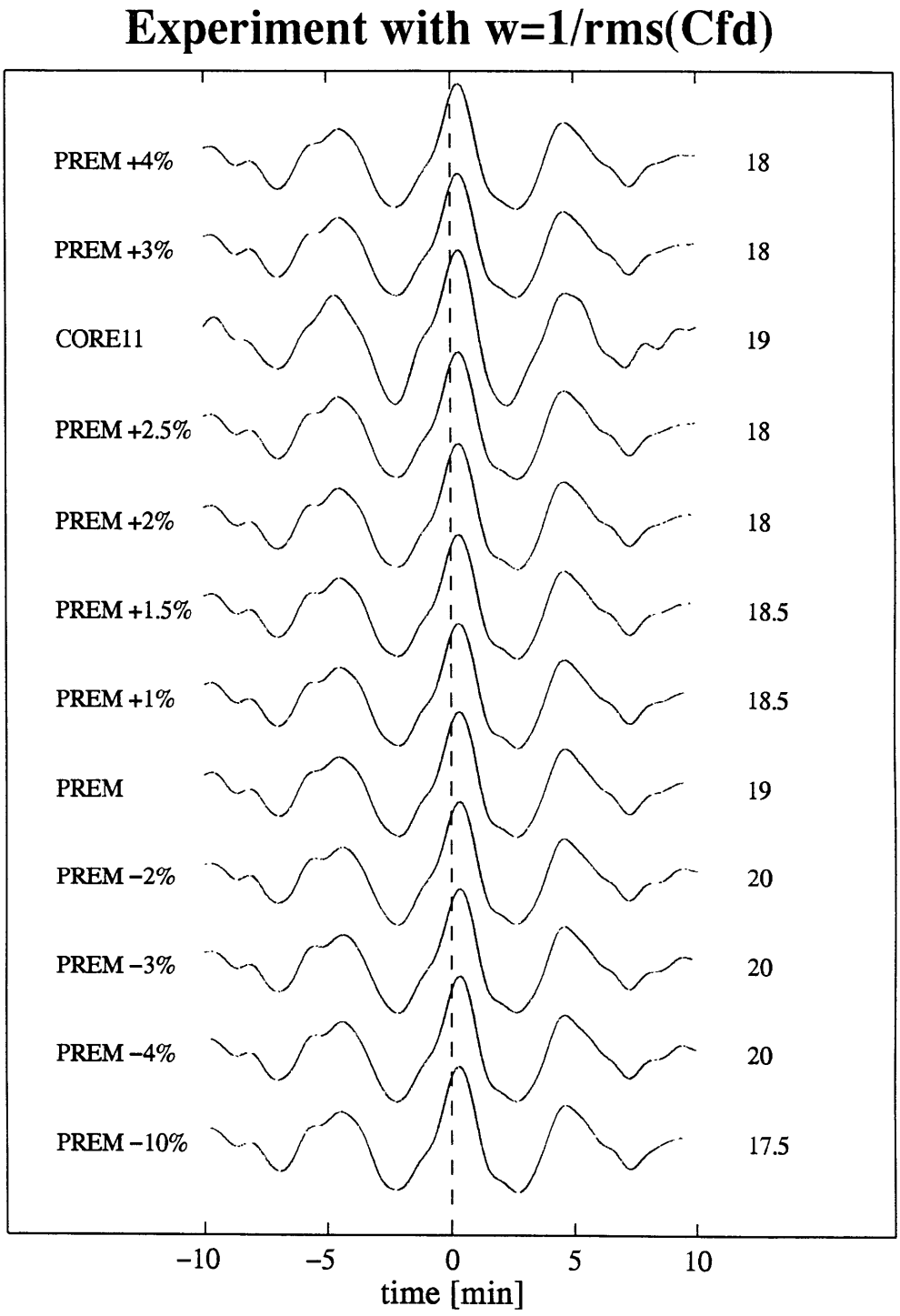
Experiment with w=1/rms(Cfd)
PREM +4%
PREM +3%
CORE11
PREM +2.5%
PREM +2%
PREM +1.5%
PREM +1%
PREM
PREM −2%
PREM −3%
PREM −4%
PREM −10%
18
18
19
18
18
18.5
18.5
19
20
20
20
17.5
−10
−5
0
5
10
time [min]

Figure 4.23

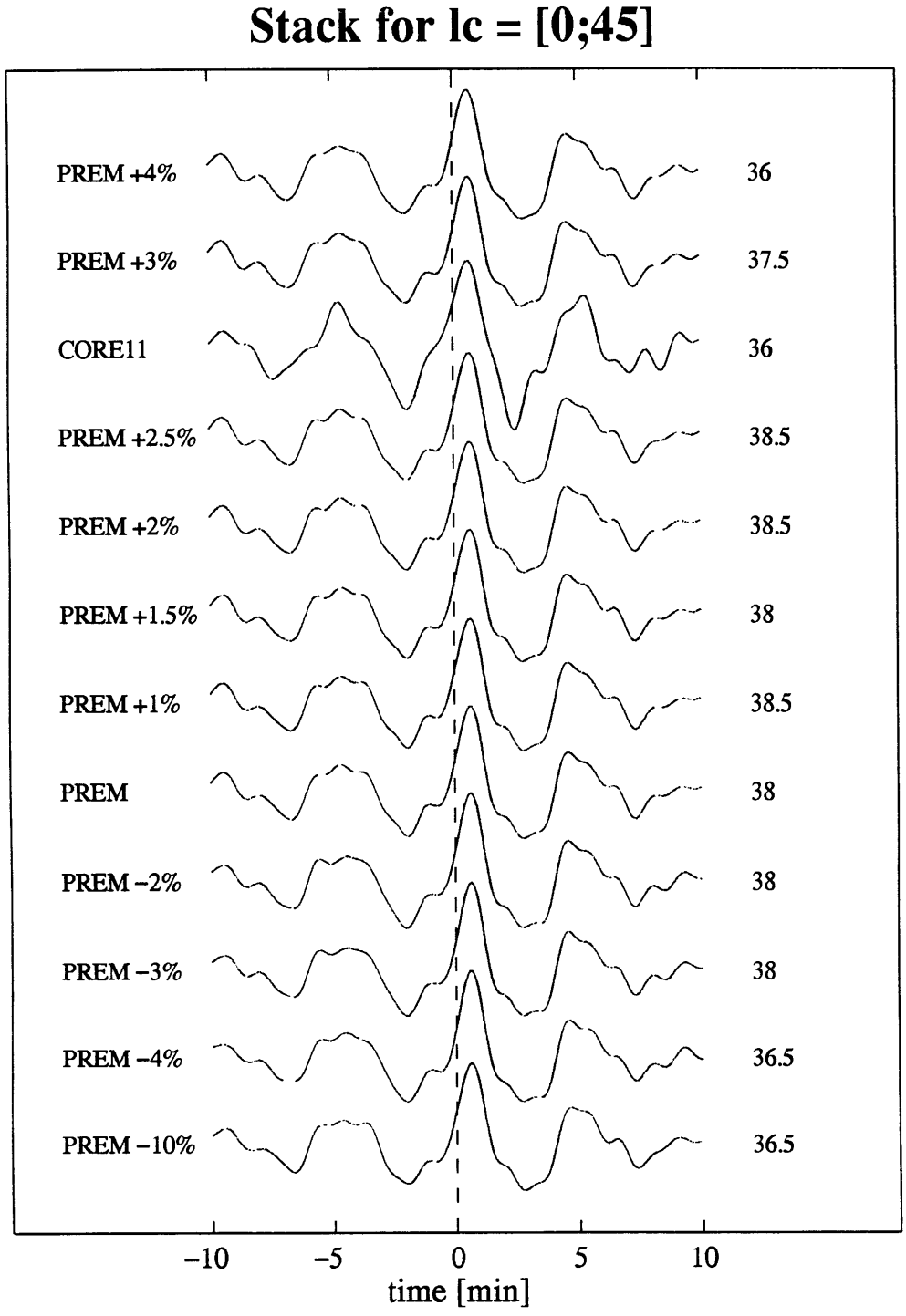
Stack for lc = [0;45]
PREM +4%
PREM +3%
CORE11
PREM +2.5%
PREM +2%
PREM +1.5%
PREM +1%
PREM
PREM −2%
PREM −3%
PREM −4%
PREM −10%
36
37.5
36
38.5
38.5
38
38.5
38
38
38
36.5
36.5
−10
−5
0
5
10
time [min]

Figure 4.24

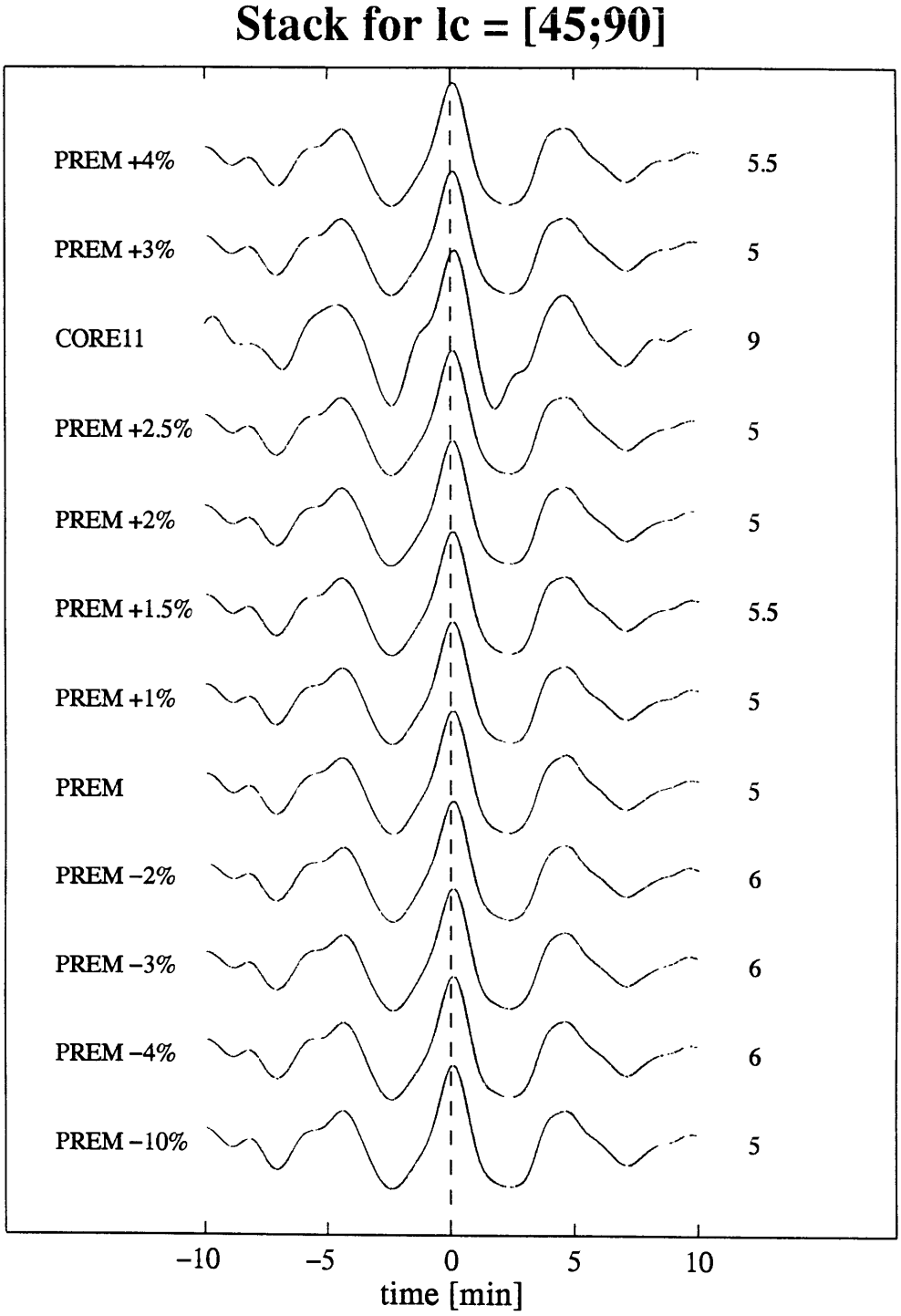
Stack for lc = [45;90]
PREM +4%
PREM +3%
CORE11
PREM +2.5%
PREM +2%
PREM +1.5%
PREM +1%
PREM
PREM −2%
PREM −3%
PREM −4%
PREM −10%
5.5
5
9
5
5
5.5
5
5
6
6
6
5
−10
−5
0
5
10
time [min]

Figure 4.25

CHAPTER 5

CONCLUSION

In this thesis, we presented a new approach to the study of the shear velocity structure of the inner core. We show that we can retrieve information about the average shear velocity in the inner core through simple cross-correlations. We show that by stacking cross-correlations calculated at different stations for different events, we can remove local variations and this way increase our signal to noise ratio. We also show that the stacking operation does not require to align the cross-correlations. We show that with this method, we can compare models with the same structure but with different average shear velocities in the inner core. We show that this method still works for models with different structure in the inner core (isotropic versus anisotropic). In the case of real data, the experiment does not work as well. When we stack all the cross-correlations, we observe a peak a well defined peak. As we vary the perturbation in our inspection models, we observe a shift of the central peak. The direction of the shift of t_C is compatible with the amount of perturbation applied. This means that we observe a signal and that this signal contains information about the inner core. For none of our models, do we observe a peak at zero time lag. We have shown that this can be explained by the ellipticity of the Earth. We note that an anisotropic model such as CORE11 does not compare better to the real Earth than an isotropic model such as PREM with a perturbation in the average shear velocity in the inner core. Furthermore, we observe difference in the quality of the stacked cross-correlations between stacks obtained for equatorial paths and stacks obtained for polar paths. This indicates some sort of anisotropy of the inner-core of the Earth. These are the results of this thesis. Where do we go from here?

We could investigate more complicated features and more complicated model space. As it is designed, the experiment is limited to the determination of the average shear

velocity of the inner core. First, we only explore the model space by perturbing the average shear velocity of the inner core. We stack all the $C_{js}(t)$ over a wide range of ray path azimuth and of epicentral distance to the receiver. Finally, we make our measurements for time windows such that the wave groups which sampled the inner core have done so over a long period of time and thus have averaged out the information on any structure they sampled. We would like to study more interesting features of the Earth. We could vary the average velocity as well as the gradient of velocity at the ICB. There are many problem associated with this. First of all direct exploration of the model space for more than one unknown is very time and memory consuming and therefore hard to implement. If we were able to linearize the problem, then by expanding the theory already written by Gee and Jordan [1992], we would be able to investigate more complicated model spaces in a more thorough way. But modes vary in a non linear way with velocity perturbation. This means that t_c will be a non linear function of the perturbations. It will make the inverse problem much more difficult to study. We can study alternative ways to select our modes and calculate our isolation filters. We need to understand the organization of normal spheroidal modes better. There has been two major studies to try to classify normal modes. One has been done by Okal [1978] . He classified normal modes based on $\tilde{Q}_k$, $\tilde{g}_k$ and $\tilde{c}_k$. in order to create classes of modes with homogenous properties. Another attempt of classification has been done by Zhao and Dahlen [1993] who recalculated the normal modes eigenfrequencies using the ray parameters and positive interference conditions. This allowed them to derive asymptotic formulae for eigenfrequencies and illustrate the ray-mode duality better. But a lot of work still needs to be done. Modes that we use to calculate our isolation filters belong to very different ray parameter regimes. What is the physics of these modes and to what wave types do they belong? A better understanding of these modes would allow us to design more optimal isolation filters. Finally, we can use more complicated models to calculate modes and seismograms. First, we should incorporate ellipticity in the calculation of our modes and seismograms. Then we can take

the model proposed by *Tromp* [1994], calculate a spherically symmetric anisotropic model for each great circle which would take into account the cylindrical anisotropy and calculate seismograms for each of these models. Tromp's model has cylindrical symmetry and it is based on PREM. This means that in the special case of equatorial paths, Tromp's model is the PREM model. Now we have shown that we do observe well formed cross-correlations for equatorial paths. We haven't been able to find a model which gives us a cross-correlation peaked at zero time lag. Nevertheless this is promising and tells us that we may be able to calculate better cross-correlations for polar paths as well. Another alternative is to take fully three dimensional models and to calculate three dimensional seismograms. The problem with this approach is to define the coupling which occurs between the modes due to aspherical structures.

APPENDIX

ILLUSTRATION OF PHYSICAL CHARACTERISTICS OF MODES FOR DIFFERENT VALUES OF ξ_k

Figure A.1 shows a complete mode table for the PREM model. There is a total of 16,614 modes for that model. The modes represented as o have a sensitivity between 0.008 and 0.012 and modes represented as + have a sensitivity between 0.012 and 1. We see that the modes which we have selected as sensitive to the inner core structure organize themselves in branches. This means that modes we selected all have the same type of physical properties. To find out what the physics of these branches are, we selected modes within a given sensitivity window and we plotted them in the ω-l diagram. We then scanned over the entire range of sensitivity between 0.008 and 1.

The modes that we selected to design the isolation filter fall in two groups.

The first group is constituted of modes with ξ_k between 0.8 and 1. This corresponds to the class of modes identified by Okal [1978] as the inner core modes (K modes). They lie along steep branches with a frequency spacing between two branches of 1.4 mHz (see Figure A.2). There are two subgroups of modes. The modes with the highest sensitivity form the lowest branch. An example is the mode ${}_{40}S_{111}$. The displacement of this mode is completely concentrated at the ICB. The Frechet kernels for these modes present two decaying tails on each side of the ICB. They correspond to Stoneley waves which travel around the ICB. They have the highest sensitivity but they do not contribute to the seismogram at all since their energy is completely localized at the ICB. The second subgroup contains all the other modes. They modes have mostly horizontal displacements, concentrated in the inner core. Over 90% of their shear energy density is in the inner core. The Frechet kernels for these modes show a large sensitivity to shear velocity in the inner core and a high sensitivity to compressional velocity in the mantle.

They correspond to PKIKP/PKJKP waves as has been shown by Zhao and Dahlen [1993]. These will be the modes with the modes with the highest sensitivity that we will still be able to measure.

The second group is constituted of modes with sensitivities ranging from 8.10^{-3} to 8.10^{-1}. They fall in the category labeled by Okal as vertical modes (V modes). They form very steep branches. We find a frequency spacing between two branches of 0.8 mHz which is compatible with the value of 0.82 mHz derived theoretically by Okal [1978]. They present mostly vertical displacement in the outer core. The horizontal displacement starts being predominant in the inner core. Their energy is primarily compressional and they only have 10% of their shear energy density in the inner core. The Frechet kernels for these modes show an equal sensitivity to compressional and shear velocity throughout the Earth. They sample the upper part of the inner core and present an evanescent tail as the radius goes to zero, as shown by the Frechet kernels. This group of modes correspond to PKP and PKIKP/PKJKP waves. These are the most important modes since they will constitute all the energy and therefore most of the sensitivity of the isolation filter.

For the modes which have a ξ_k smaller than 8.10^{-3}, we recognize again sensitivity windows in which we observe a uniform behavior. We isolate this way 3 groups. One is composed of modes with values of ξ_k ranging from 10^{-3} to 8.10^{-3}. Those are the same V modes as the one we chose to calculate our isolation filter except that their sensitivity is lower (Figure A.3). The second group has a sensitivity ranging from 10^{-7} to 10^{-3}. These have been described by Okal as colatitudinal modes (C modes). These are modes with mostly horizontal displacement in the mantle and very little vertical displacement in the outer core. Their energy pattern is dominated by shear energy in the mantle and they correspond to ScS/SKS waves (see Figure A.4). The last group has a sensitivity ranging from 0 to 10^{-7}. This group is made of highly hybridized modes. We can recognize three trends, a C and V mode trend for modes with a relatively high ξ_k and a radial mode (R

mode) trend for relatively lower sensitivities. An interesting feature is that in this group, windows in sensitivity tend to align themselves parallel one to another and that the sensitivity decreases for increasing angular order (see Figure A.5).

We have shown here that we can recognize different groups of modes, in which modes all have the same properties. Although there is some overlap between the groups, they seem fairly distinct from each other and they can be assigned some boundary in sensitivity This should allow us to understand better the physics of the modes which form the isolation filters. This is an interesting observation which could help us in designing more optimal isolation filters.

Figure Captions

Figure A.1 : Complete ω-l diagram for the PREM model. Frequency ranges from 0 to 50 mHz and angular order goes from l=0 to l=130. Modes with ξ_k less than 0.008 are represented by ".". The modes represented by "o" have a ξ_k between 0.008 and 0.012. Modes represented by "+" have a ξ_k bigger than 0.012.

Figure A.2 : The top plot shows the ω-l diagram for modes with ξ_k comprised between 0.8 and 1. The modes with a ξ_k between 0.8 and 0.88 are represented by ".". The modes with a ξ_k between 0.88 and 0.96 are represented by "o". The modes with a ξ_k between 0.96 and 1 are plotted as "+". The lowest branches corresponds to the Stoneley branch identified by Okal. We note that sensitivity decreases in that branch as the angular order increases. The bottom plots show two examples of modes belonging to this group. ${}_{61}S_6$ is a regular K mode and ${}_{40}S_{111}$ is a Stoneley mode. The plots show the displacement functions (horizontal displacement dotted and vertical displacement solid) and the Frechet kernels for S (dotted) and P (solid). We note the evanescent tails for ${}_{40}S_{111}$.

Figure A.3 : The top plot shows the ω-l diagram for modes with ξ_k comprised between 0.001 and 0.8. The modes with a ξ_k between 0.001 and 0.1 are plotted as "+". The modes with a ξ_k between 0.1 and 0.8 are plotted as ".". The modes correspond to V modes. The frequency spacing of the branches is 0.8 mHz. The bottom plots show one example of mode belonging to this group, ${}_{54}S_9$. The plots show the displacement functions (horizontal displacement dotted and vertical displacement solid) and the Frechet kernels for S (dotted) and P (solid).

Figure A.4 : The top plot shows the ω-l diagram for modes with ξ_k between 10^{-7} and 10^{-3}. The modes correspond to C modes. The frequency spacing of the branches is 1.06

mHz. The bottom plots show one example of mode belonging to this group, ${}_{101}S_2$. The plots show the displacement functions (horizontal displacement dotted and vertical displacement solid) and the Frechet kernels for S (dotted) and P (solid).

Figure A.5 : The plot shows the ω-l diagram for modes with ξ_k between 10^{-60} and 10^{-7}. The modes with a ξ_k between 10^{-60} and 10^{-30} are represented as "+". The modes with a ξ_k between 10^{-30} and 10^{-15} are represented as "o". The modes with a ξ_k between 10^{-15} and 10^{-7} are represented as ".". The branches are highly hybridized. We observe numerous tessellations in the branches which indicates this hybridization. The modes correspond to a mixing of V, C and R modes. Windows in sensitivity align themselves parallel one to another.

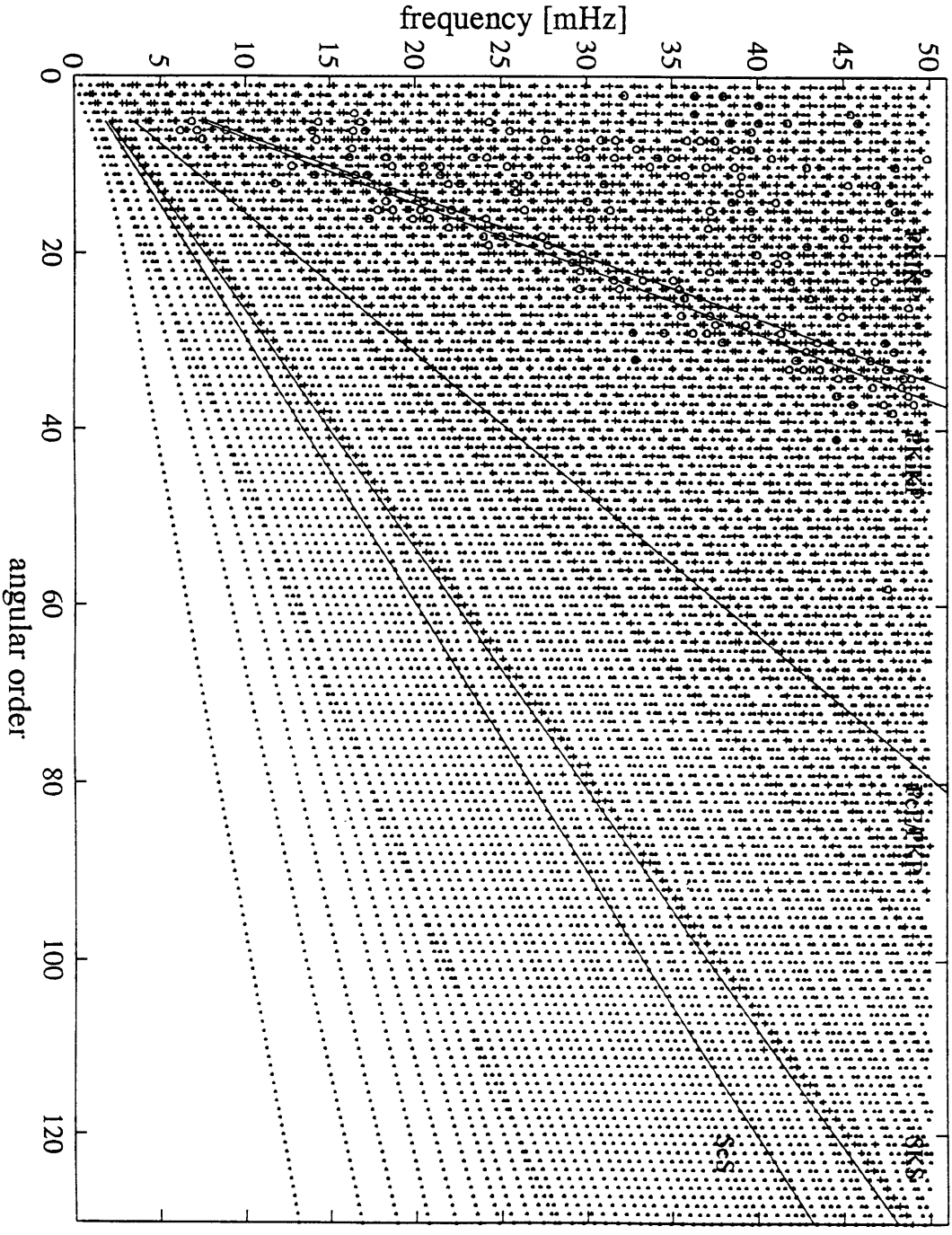
Mode table for PREM
frequency [mHz]
angular order
0
5
10
15
20
25
30
35
40
45
50
0
20
40
60
80
100
120
PKiKP
PcP, pPKP
ScS
SKS

Figure A.1

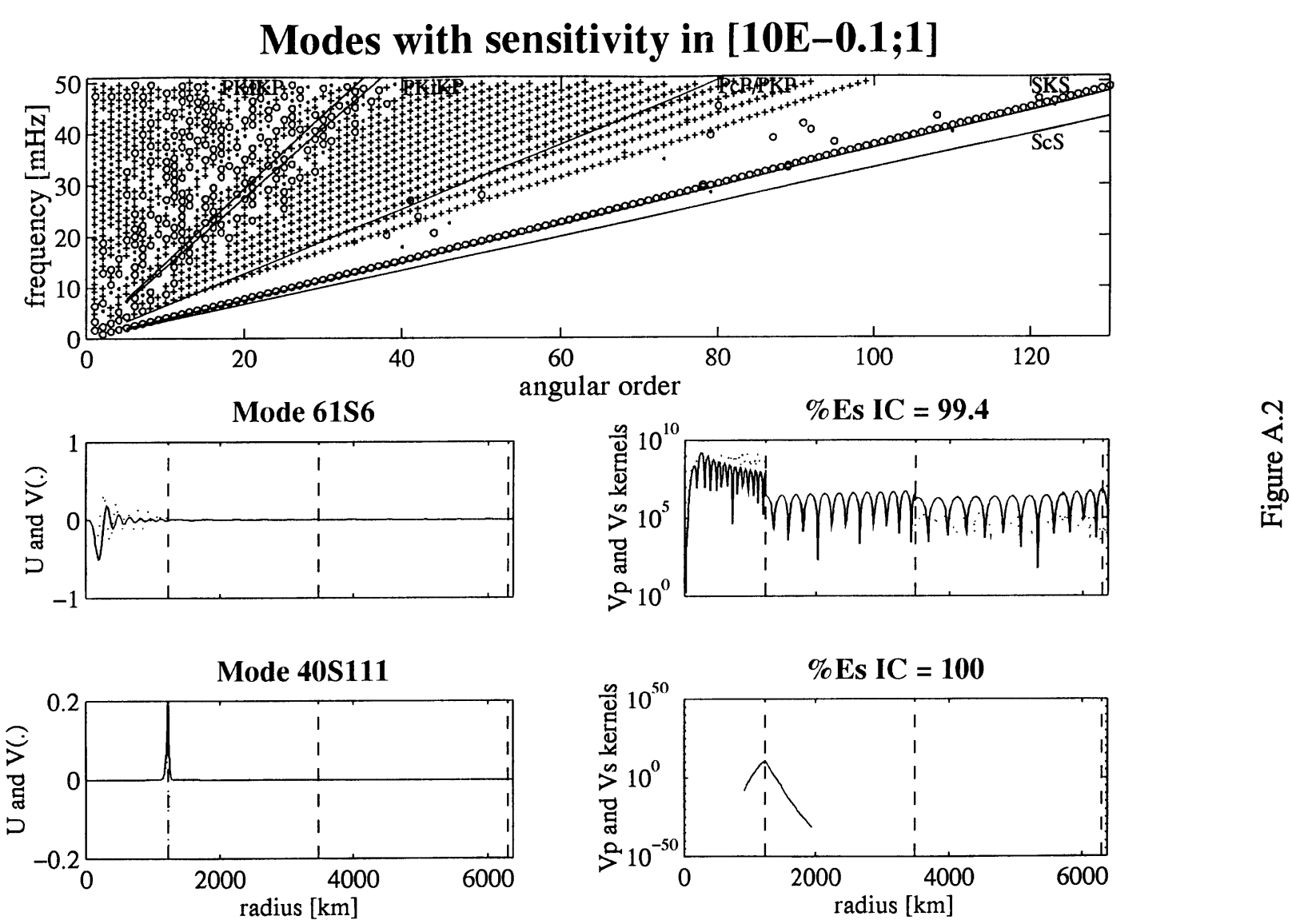
Modes with sensitivity in [10E-0.1;1]
PKiKP
PKIKP
PcP/PKP
SKS
ScS
frequency [mHz]
angular order
Mode 61S6
%Es IC = 99.4
U and V(.)
Vp and Vs kernels
Mode 40S111
%Es IC = 100
radius [km]

Figure A.2

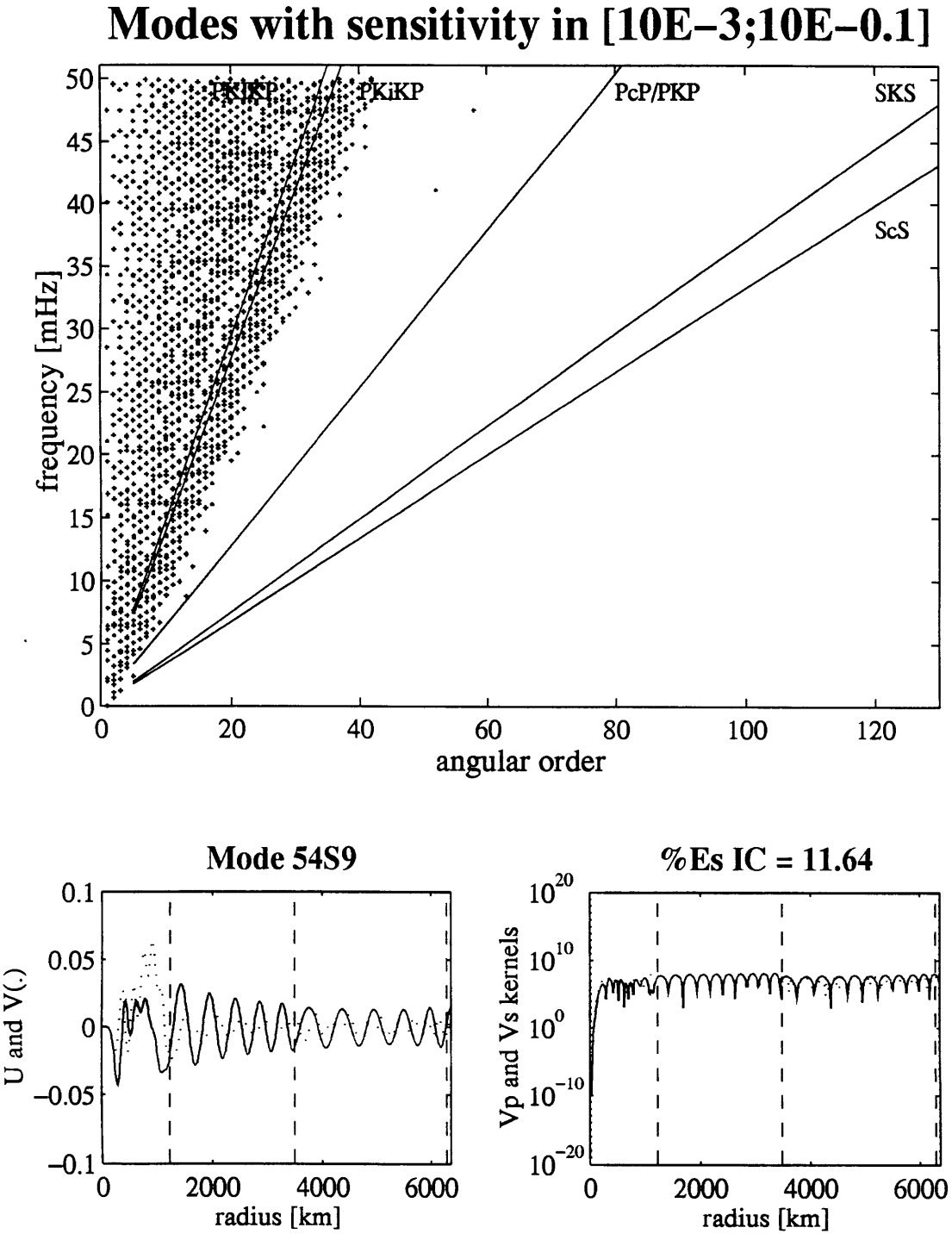
Modes with sensitivity in [10E−3;10E−0.1]
PKiKP
PKiKP
PcP/PKP
SKS
ScS
frequency [mHz]
angular order
Mode 54S9
%Es IC = 11.64
U and V(.)
Vp and Vs kernels
radius [km]
radius [km]

Figure A.3

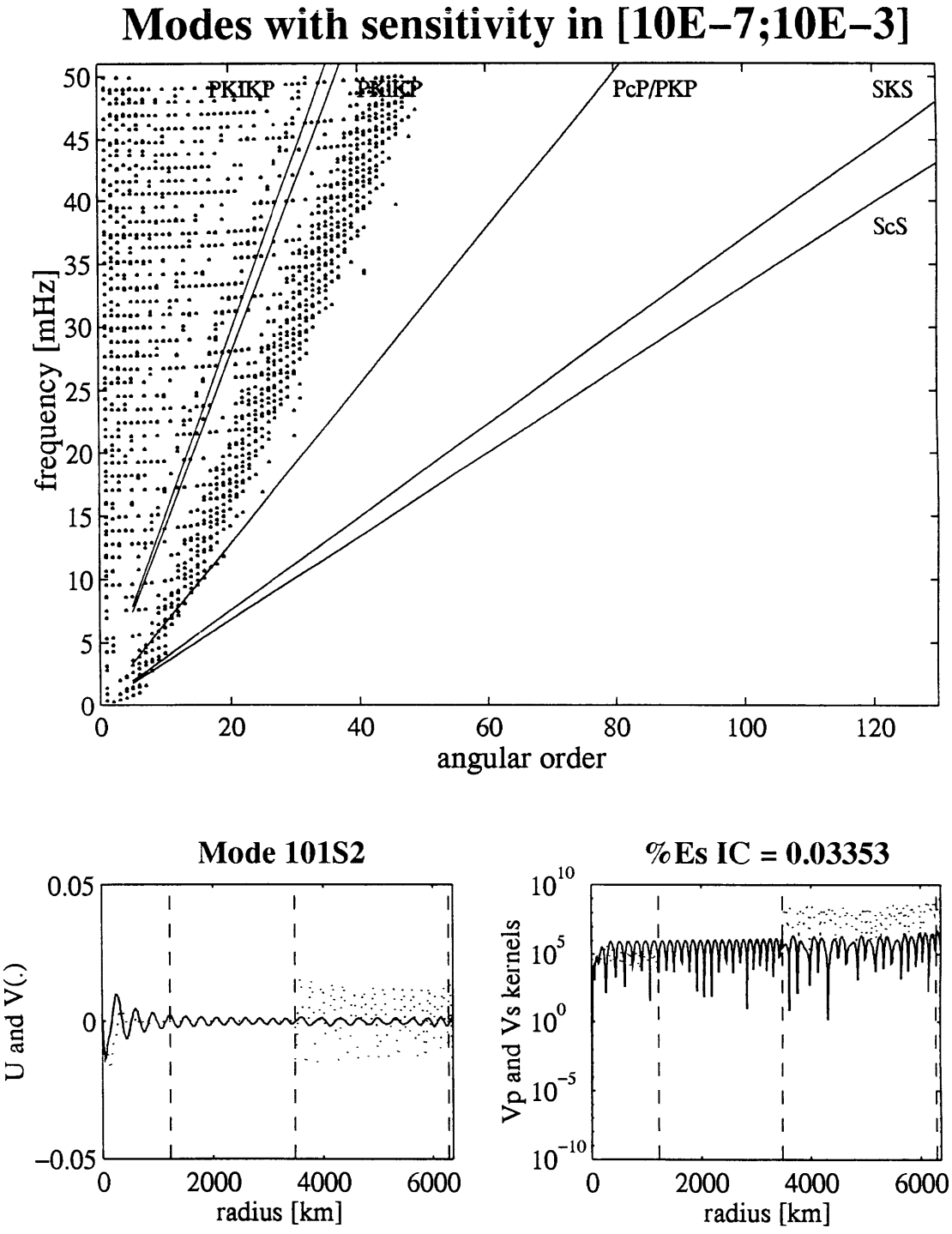
Modes with sensitivity in [10E−7;10E−3]
PKIKP
PKiKP
PcP/PKP
SKS
ScS
frequency [mHz]
angular order
Mode 101S2
%Es IC = 0.03353
U and V(.)
Vp and Vs kernels
radius [km]
radius [km]

Figure A.4

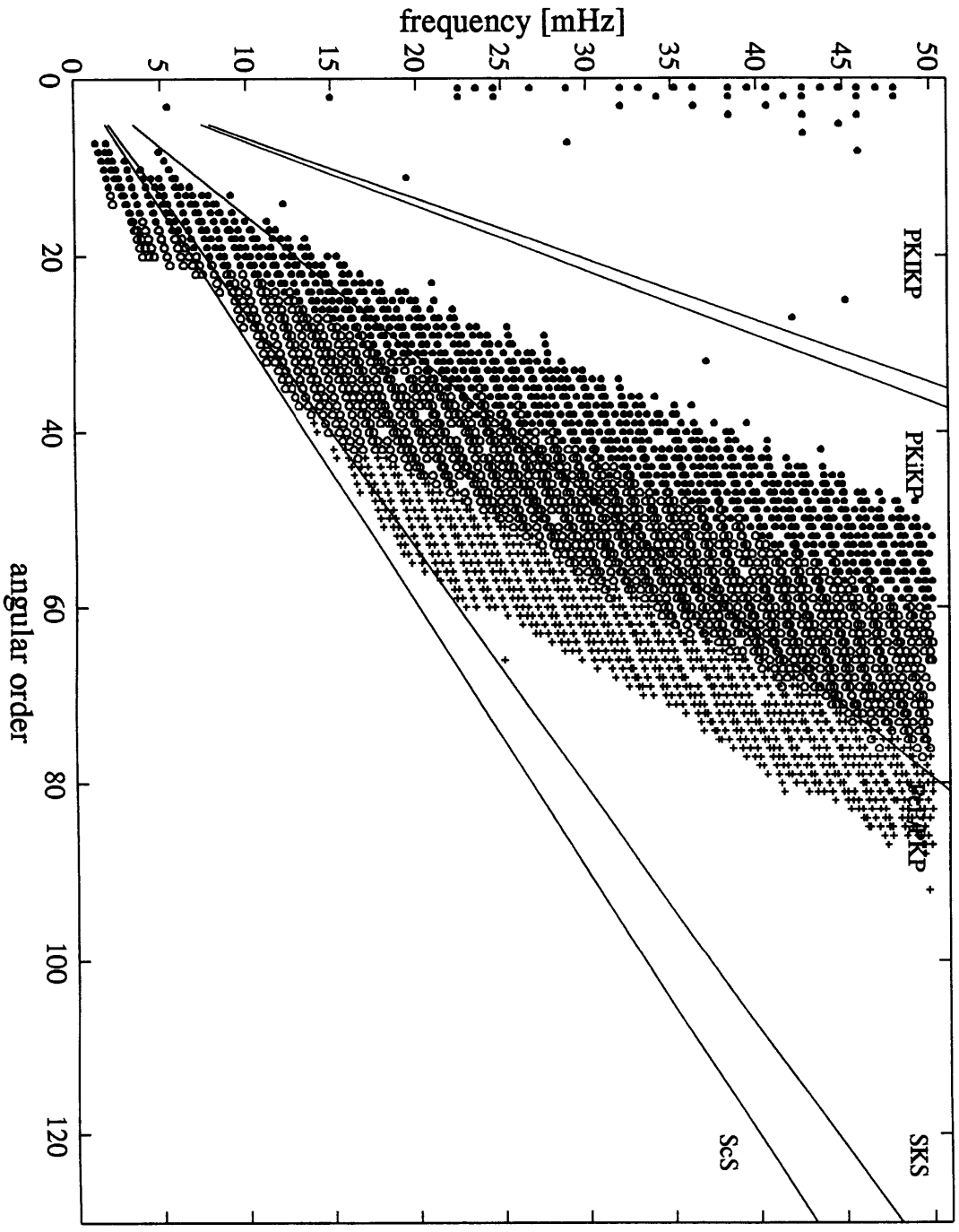
Modes with sensitivity in [10E−60;10E−7]
frequency [mHz]
angular order
PKIKP
PKiKP
SKS
ScS
0
5
10
15
20
25
30
35
40
45
50
0
20
40
60
80
100
120

Figure A.5

BIBLIOGRAPHY

Agnew, D., and J. Berger, Vertical seismic noise at very low frequencies, *J. Geophys. Res.*, *83*, 5420-5424, 1964.

Backus, G. E., and F. Gilbert, Numerical applications of a formalism for geophysical inverse problems, *13*, 247-276, 1967.

Choy, G. L., and V. F. Cormier, The structure of the inner core inferred from short-period and broadband GDSN data, *72*, 1-21, 1983.

Creager, K. C., Anisotropy of the inner core from differential travel times of the phases PKP and PKIKP, *356*, 309-314, 1992.

Cummins, P., and L. R. Johnson, Short-period body wave constraints of properties of the Earth's inner core boundary, *93*, 9058-9074, 1988a.

Cummins, P., and L. R. Johnson, Synthetic seismograms for an inner core transition of finite thickness, *94*, 21-34, 1988b.

Doornbos, D. J., The anelasticity of the inner core, *38*, 397-415, 1974.

Doornbos, D. J., Observable effects of seismic absorption band in the Earth, *75*, 693-711, 1983.

Dziewonski, A. M., and D. L. Anderson, Preliminary reference Earth model, *25*, 297-356, 1981.

Dziewonski, A. M., and J. F. Gilbert, Solidity of the inner core inferred from normal mode observations, *234*, 465-466, 1971.

Dziewonski, A. M., and J. F. Gilbert, Observations of normal modes from 84 recordings of the Alaskan earthquake of 28 March 1964, *27*, 393-446, 1972.

Fukao, Y., and N. Suda, Core modes of the Earth's free oscillations and structure of the inner core, *16*, 401-404, 1989.

Gee, L. S., and T. H. Jordan, Generalized seismological data functionals, *111*, 363-390, 1992.

Häge, H., Velocity constraints for the inner core inferred from long-period PKP amplitudes, *31*, 171-185. 1983.

Ihmlé, P. F., Teleseismic Study of Rupture Processes with Long Duration, thesis, M.I.T., 1994.

Jordan, T. H., and S. A. Sipkin, Estimation of the attenuation operator for multiple ScS waves, *Geophys. Res. Lett.*, *4*, 167-170, 1977.

Julian, B. R., D. Davies, and R. M. Sheppard, PKJKP, *235*, 317-318, 1972.

Li, X.-D., D. Giardini, and J. H. Woodhouse, Large-scale three-dimensional even-degree structure of the Earth from splitting of long-period normal modes, *96*, 551-577, 1991.

Masters, D., and F. Gilbert, Structure of the inner core inferred from observations of its spheroidal shear modes, *8*, 569-571, 1981.

Masters, G., Anomalous splitting: an unexplained phenomenon, *4th annual IRIS workshop,* 1992.

Morelli, A., A. M. Dziewonski, and J. H. Woodhouse, Anisotropy of the inner core inferred from PKIKP travel times, *13*, 1545-1548, 1986.

Okal, E. A., A physical classification of the Earth's spheroidal modes, *26*, 75-103, 1978.

Poupinet, G., R. Pillet, and A. Souriau, Possible heterogeneity of the Earth's core deduced from PKIKP travel times, *Nature*, *305*, 204-206, 1983.

Ritzwoller, M., G. Masters, and F. Gilbert, Observations of anomalous splitting and their interpretation in terms of aspherical structure, *91*, 10,203-10,228, 1986.

Ritzwoller, M., G. Masters, and F. Gilbert, Constraining aspherical structure with low degree interaction coefficients: application to uncoupled multiplet, *93*, 6369-6396, 1988.

Romanowicz, B., and J. F. Karczewski, GEOSCOPE program: progess report, *Institut de Physique du Globe de Paris, IPG/INSU 01-1989*, 1989.

Shearer, M. M., K. M. Toy, and J. A. Orcutt, Axi-symmetric earth models and inner core anisotropy, *333*, 228-232, 1988.

Shearer, P. M., and G. Masters, The density and shear velocity contrast at the inner core boundary, *102*. 491-498, 1990.

Shearer, P. M., and K. M. Toy, PKP(BC) versus PKP(DF) differential travel times and aspherical structure in the Earth's inner core, *96*, 2233-2247, 1991.

Souriau, A., and M. Souriau, Ellipticity and density at the inner core boundary from sub-critical PKiKP and PcP data, *98*, 39-54, 1989.

Tromp, J., Support for anisotropy of the Earth's inner core from free oscillations, *Nature*, in press, 1994.

Widmer, R., G. Masters, and F. Gilbert, The spherically symmetric Earth: observational aspects and constraints on new models, *69*, 1310, 1988

Widmer, R., G. Masters, and F. Gilbert, Spherically symmetric attenuation within the Earth from normal mode data, *Geophys. J. Int.*, *111*, 559-576, 1992.

Woodhouse, J. E., and F. A. Dahlen, The effect of a general aspherical perturbation on the free oscillations of the Earth, *53*, 335-354, 1978.

Woodhouse, J. H., On Rayleigh's principle, *46*, 11-22, 1978.

Woodhouse, J. H., D. Giardini, and X.-D. Li, Evidence for inner core anisotropy from free oscillation oscillations, *13*, 1549-1552, 1986.

Zhao, L., and F. A. Dahlen, Asymptotic eigenfrequencies of the Earth's normal modes, 1993.

2809-13